

Distribution Agreement

In presenting this thesis or dissertation as a partial fulfillment of the requirements for an advanced degree from Emory University, I hereby grant to Emory University and its agents the non-exclusive license to archive, make accessible, and display my thesis or dissertation in whole or in part in all forms of media, now or hereafter known, including display on the world wide web. I understand that I may select some access restrictions as part of the online submission of this thesis or dissertation. I retain all ownership rights to the copyright of the thesis or dissertation. I also retain the right to use in future works (such as articles or books) all or part of this thesis or dissertation.

Signature:

Joel R. Schmitz

Date

Spectroscopic Characterization of the Low-Lying States of $\text{MX}^{0/+}$

(M = Ca, Nd, Sm, Th; X = N,O) Molecules

By

Joel R. Schmitz

Doctor of Philosophy

Chemistry

Michael C. Heaven, Ph.D.
Advisor

Katherine Davis, Ph.D.
Committee Member

Francesco Evangelista, Ph.D.
Committee Member

Accepted:

Kimberly Jacob Arriola, Ph.D., MPH
Dean of the James T. Laney School of Graduate Studies

Date

Spectroscopic Characterization of the Low-Lying States of $\text{MX}^{0/+}$

(M = Ca, Nd, Sm, Th; X = N,O) Molecules

By

Joel R. Schmitz

M.S., Wright State University, 2017

B.S., Wright State University, 2014

Advisor: Michael C. Heaven, Ph.D.

An abstract of
A dissertation submitted to the Faculty of the
James T. Laney School of Graduate Studies of Emory University
in partial fulfillment of the requirements for the degree of
Doctor of Philosophy
in Chemistry
2022

Abstract

Spectroscopic Characterization of the Low-Lying States of $\text{MX}^{0/+}$

(M = Ca, Nd, Sm, Th; X = N,O) Molecules

By: Joel R. Schmitz

Electronic structure characterization of small metal-containing molecules can determine chemical bonding properties with applications ranging to real world problems, such as safe nuclear waste treatment, to those of chemical fundamental interest, such as detangling rotational perturbations. In this work, the electronic structure of ThO, ThN, CaO, NdO^{0/+}, and SmO^{0/+} was characterized through low- and high-resolution laser induced fluorescence (LIF) and dispersed fluorescence (DLIF) techniques.

The electronic structure of actinide complexes is of interest both in relation to actinide extraction in nuclear waste and the extent of *5f* orbital involvement in actinide chemical bonding. Thirty-four ThO LIF transitions involving previously unobserved vibronic states were characterized, observing the O'(0⁺) and L'(1) states for the first time. Vibrationally hot spectra allowed calculation of the potential energy curve of the X¹Σ⁺ state. Eleven vibronic transitions of ThN were observed in the range of 19,600-21,000 cm⁻¹, determining molecular constants and fluorescence lifetimes which were complemented by electronic structure calculations.

CaO has an extremely complex excited state electronic structure, which can be explained by extreme electron localization on the Ca⁺ and O⁻ centers. Higher levels of the A'¹Π(Xσπ⁻¹) state (ν = 10-17) were observed, as well as a perturbation of the A'¹Π(Xσπ⁻¹) ν = 17. DLIF spectroscopy was used to examine the homogenous perturbation of the C¹Σ⁺(Bσσ⁻¹) ν = 7, assigning the perturbing Ω = 0⁺ state as the g³Π(0⁺)(Bσπ⁻¹) ν = 12 state.

The chemi-ionization of lanthanide metals is being employed as a method of increasing the atmospheric electron density for communication applications. Chemical launches have produced space clouds with visible emissions but spectroscopic data is lacking for cloud characterization. Molecular constants for sixteen bands of NdO as well as vibrational parameters for the X4 ground state and five low-lying excited states were determined from LIF and DLIF spectra. Molecular constants for four bands of SmO from 15,270-15420 cm⁻¹ were determined for the ¹⁵²SmO and ¹⁵⁴SmO isotopologues. High-resolution LIF was used to observe the hyperfine structure of the [15.35]1 state and Einstein coefficients were determined from DLIF spectra. While no direct LIF observation of NdO⁺ or SmO⁺ was successful using photoionization spectroscopy, atomic and molecular fluorescence depletion was observed. Dispersed fluorescence of UV-excited gas expansions was recorded to compare to space launch results. Future work should search for NdO⁺ and SmO⁺ LIF in the near-UV range.

Spectroscopic Characterization of the Low-Lying States of $\text{MX}^{0/+}$

(M = Ca, Nd, Sm, Th; X = N,O) Molecules

By

Joel R. Schmitz

M.S., Wright State University, 2017

B.S., Wright State University, 2014

Advisor: Michael C. Heaven, Ph.D.

A dissertation submitted to the Faculty of the
James T. Laney School of Graduate Studies of Emory University
in partial fulfillment of the requirements for the degree of
Doctor of Philosophy
in Chemistry
2022

Acknowledgements

I would like to thank my advisor Dr. Michael Heaven for his scientific knowledge and assistance over the past five years. Without him, this dissertation could not literally be written. I would also like to thank Dr. Anh Le and Dr. Timothy Steimle for their assistance with the high-resolution LIF chamber and assisting me with understanding and fitting the SmO hyperfine spectra. I would also like to thank Dr. David Dolson for introducing me to spectroscopy and igniting my passion in this field. Finally, I would like to thank my partner Eric Townsley for his support and pressing me forward toward this goal.

Table of Contents

CHAPTER 1: INTRODUCTION	1
1.1 Introduction	2
1.2 Chapter 1 References	8
CHAPTER 2: EXPERIMENTAL METHODS	10
2.1 Laser Ablation and Supersonic Expansion	11
2.2 Laser-induced Fluorescence (LIF)	14
2.2.1 Overview of LIF	14
2.2.2. Low-Resolution LIF Experimental Setup	15
2.2.3. High-Resolution LIF Experimental Setup	18
2.3. Dispersed Laser-Induced Fluorescence (DLIF)	20
2.4 Vacuum Ultraviolet (VUV) Single-Photon Ionization	24
2.5 Chapter 2 References	26
CHAPTER 3: CHARACTERIZATION OF THE LOW-LYING STATES OF THO AND THN	28
3.1. Introduction	29
3.1.1. Motivation for Electronic Structure Characterization of Actinides ..	29
3.1.2 Previous Studies of ThO	32
3.1.3 Previous Studies of ThN	36
3.2 ThO Results	39
3.2.1 ThO LIF Spectra and Fitting Results	39
3.2.2 $X^1\Sigma^+$ Ground State Potential Energy Curve Generation	43
3.3 ThO Discussion	46
3.3.1 Vibrational Extension of the $C^1\Pi$, $D^1\Pi$, $E^1\Sigma^+$, $I^1\Pi$, and $F^1\Pi$ Electronic States	46
3.3.2 Characterization of New $O'(0^+)$ and $L'(1)$ Electronic States	48
3.4 ThN Results	49
3.4.1 ThN Experimental Results	49
3.4.2 Electronic Structure Calculations	56

3.5 ThN Discussion	60
3.6 Chapter 3 References	63
CHAPTER 4: PETURBATIONS OF THE $A^1\Pi(X\sigma\pi^{-1})$ AND $C^1\Sigma^+(B\sigma\sigma^{-1})$ STATES OF CAO	71
4.1 Introduction	72
4.2 CaO Results	76
4.2.1 The $A^1\Pi(X\sigma\pi^{-1})$ - $X^1\Sigma^+$ bands	76
4.2.2 Wavelength and Time-Resolved Fluorescence Measurements for the $C^1\Sigma^+(B\sigma\sigma^{-1})$ and γ_0^+ States	80
4.3 Discussion	82
4.3.1 $A^1\Pi(X\sigma\pi^{-1})$ $v = 17$ Perturbation	82
4.3.2 Assignment of the γ_0^+ state as the $g^3\Pi_{0+}(B\sigma\pi^{-1})$ state	85
4.4 Chapter 4 References	89
CHAPTER 5: CHARACTERIZATION OF THE LOW-LYING STATES OF NdO and SMO AND THE SEARCH FOR NdO⁺ AND SmO⁺	93
5.1 Introduction	94
5.1.1 The Chemi-ionization of Lanthanides	94
5.1.2 Previous Studies of NdO and NdO ⁺	97
5.1.3 Previous Studies of SmO and SmO ⁺	100
5.2 Preliminary NdO Results	105
5.3 NdO ⁺ Results	113
5.3.1 Search for NdO ⁺ LIF	113
5.3.2 Emission Spectra of Nd-based Gas Expansions	114
5.4 NdO and NdO ⁺ Discussion	115
5.5 SmO Results	119
5.5.1 Low-Resolution LIF and DLIF Results	119
5.5.2 Fluorescence Lifetime and Einstein coefficients A_{ij} Determination ..	124
5.5.3 Hyperfine Structure of the [15.35]1 State	125
5.6 Preliminary SmO ⁺ Results	127
5.6.1. Sm and SmO Depletion	127
5.6.2. Emission Spectra of UV-Excited Sm-based Gas Expansions	130

5.7 SmO and SmO ⁺ Discussion	131
5.8 SmO Einstein A_{ij} Coefficients	136
5.9 Chapter 5 References	139

List of Figures

CHAPTER 2: EXPERIMENTAL METHODS	10
2.1. Ablation and supersonic expansion experimental design	12
2.2 Laser-induced fluorescence (LIF) in a diatomic molecule AB	14
2.3 Experimental setup for the low-resolution laser-induced fluorescence (LIF) collection and processing	16
2.4 Experimental setup for the sub-Doppler absorbance spectrum of iodine	19
2.5 Illustration of dispersed laser-induced fluorescence (DLIF)	21
2.6 Experimental setup for acquisition of dispersed laser-induced fluorescence (DLIF) spectra	23
 CHAPTER 3: CHARACTERIZATION OF THE LOW-LYING STATES OF THO AND THN	 28
3.1 ThN survey recorded using REMPI spectroscopy	36
3.2 Rotationally resolved spectrum of the $D^1\Pi-X^1\Sigma^+$ 2-0 transition with a rotational temperature of 80K	40
3.3 RKR potential energy curve for the ground $X^1\Sigma^+$ state of ThO	46
3.4 Energy diagram of selected $F^1\Sigma^+-X^1\Sigma^+$ and $O'(0^+)-X^1\Sigma^+$ vibronic transitions with vibrational intervals for the $F^1\Sigma^+$. All energy values are in cm^{-1} and the schematic is not to scale	48
3.5 Rotational spectrum of $\Omega'=3/2-X^2\Sigma^+$ band centered at 20605 cm^{-1} . The downward trace is a theoretical fit assuming a rotational temperature of 90 K ...	50
3.6 Rotational structure of the perturbed $\Omega'=1/2-X^2\Sigma^+$ band centered at 20197 cm^{-1} . The downward trace is a fit assuming a rotational temperature of 40 K	53
3.7 DLIF spectra for the observed ThN bands. The excitation photon energies are listed to the left-hand column and the ground state vibrational levels are listed across the top of the figure	55
3.8 Calculated potential energy curves for the low-energy doublet states of ThN .	57
3.9 Calculated potential energy curves for the low-energy quartet states of ThN ..	58

CHAPTER 4: PETURBATIONS OF THE $A^1\Pi(X\sigma\pi^{-1})$ AND $C^1\Sigma^+(B\sigma\sigma^{-1})$ STATES OF CAO	71
4.1 Illustration of the molecular orbitals of the CaO $X\sigma\pi^{-1}$ and $B\sigma\sigma^{-1}$ electronic configurations	73
4.2 LIF spectrum of the CaO $A^1\Pi(X\sigma\pi^{-1})$ - $X^1\Sigma^+$ 10-0 band. The downward going trace is a simulation at a rotational temperature of 60 K generated in PGOHPER .	77
4.3 Dispersed fluorescence spectra for CaO of the states $C^1\Sigma^+(B\sigma\sigma^{-1})$ $v = 6,7,8$ and $\gamma 0^+ v = n-1, n, n+1$. The filled symbols indicate the lower electronic state with $\bullet = X^1\Sigma^+$, $\blacksquare = A^1\Sigma^+(X\sigma\sigma^{-1})$, and $\blacktriangle = a^3\Pi_{0+}(X\sigma\pi^{-1})$	81
CHAPTER 5: CHARACTERIZATION OF THE LOW-LYING STATES OF NdO and SMO AND THE SEARCH FOR NdO⁺ AND SmO⁺	93
5.1 Thermodynamic pathway for the chemi-ionization of lanthanide M	85
5.2 Rotationally-resolved LIF spectrum of the NdO [16.17]4-X4 $v'' = 0$ transition	105
5.3 Dispersed fluorescence spectrum induced by excitation of the NdO [16.17]4-X4 $v'' = 0$ transition. Emissions are assigned with the vibronic identities	107
5.4 Rotationally fit of the ^{142}NdO isotope in the [20.82]4-X4 $v'' = 2$ transition . . .	109
5.5 Dispersed fluorescence spectra of NdO bands at excitation energies from 15,153 cm^{-1} to 17,601 cm^{-1}	110
5.6 Dispersed fluorescence spectra of NdO bands at excitation energies from 18,075 cm^{-1} to 20,852 cm^{-1}	111
5.7 NdO vibronic energies of the electronic ground and low-lying states determined from the DLIF spectra, plotted as a function of $v + 0.5$	112
5.8 Emission spectra from Nd-containing gas expansions excited at a 193 nm ArF excitation wavelength	115
5.9 Rotationally-resolved LIF spectrum of the SmO [15.35]1-X0 ⁻ ($v=0$) transition. The insert shows the isotopic splitting of the rotational lines as well the natural abundance for the four prominent SmO isotopes	119
5.10 Dispersed fluorescence spectra of seven observed SmO bands	121
5.11 DLIF spectrum of the SmO [15.35]1-X0 ⁻ 0-0 excitation	122

5.12 Vibronic energies of the electronic ground and low-lying states determined from the DLIF spectra plotted as a function of $v + 0.5$	123
5.13 Hyperfine structure of the [15.35]1-X0 ⁻ 0-0 R(4) line of the ¹⁴⁹ SmO, ¹⁴⁸ SmO, and ¹⁴⁷ SmO isotopologues	125
5.14 Sm fluorescence at 17,778 cm ⁻¹ depletion measurements	129
5.15 SmO [15.35]-X0 ⁻ 0-0 fluorescence depletion measurements	130
5.16 Emission spectra from Sm-based gas expansions excited at a 193 nm ArF excitation wavelength	131

List of Tables

CHAPTER 2: EXPERIMENTAL METHODS	10
2.1 Gas expansion conditions for optimal production of MX species	13
CHAPTER 3: CHARACTERIZATION OF THE LOW-LYING STATES OF ThO AND ThN	28
3.1 States arising from low-energy electronic configurations of ThN	38
3.2 Band origins and rotational constants for newly observed vibronic states of ThO	42
3.3 Molecular constants of unassigned ThO bands	43
3.4 Vibrational constants for ThO	43
3.5 RKR potential energy curve data for the ThO ground $X^1\Sigma^+$ state	44
3.6 Expanded morse oscillator potential energy parameters for the ground $X^1\Sigma^+$ state of ThN	45
3.7 Ground ThN $X^2\Sigma^+ v'' = 0$ state rotational constants reproduced from Le <i>et al.</i> ⁵⁰	51
3.8 Excited state molecular constants determined from unperturbed bands of ThN	52
3.9 Excited state molecular constants derived from the three observed perturbed bands of ThN	54
3.10 Molecular constants for the doublet and quarter states of ThN up to 17,000 cm^{-1}	58
3.11 Calculated doublet energy levels of ThN at an internuclear distance of $r = 1.82 \text{ \AA}$	60
CHAPTER 4: PERTURBATIONS OF THE $A^1\Pi(X\sigma\pi^{-1})$ AND $C^1\Sigma^+(B\sigma\sigma^{-1})$ STATES OF CaO	71
4.1 Molecular constants for the $A^1\Pi(X\sigma\pi^{-1})$ state determined from rotational fits of the LIF spectra and lifetime measurements	78
4.2 Rovibrational constants of the $A^1\Pi(X\sigma\pi^{-1})$ state obtained vibrational energy fits	79
4.3 Fluorescence decay lifetimes for the $C^1\Sigma^+(B\sigma\sigma^{-1})$ and γ_0^+ vibrational states ..	82
4.4 Low-lying excited states of CaO with their electronic configuration and CaF parentage	86

4.5 Singlet-triplet energy splitting of various electronic configurations of CaO . .	87
--	----

CHAPTER 5: CHARACTERIZATION OF THE LOW-LYING STATES OF NdO and SmO AND THE SEARCH FOR NdO⁺ AND SmO⁺ 93

5.1 Molecular constants obtained from fitting results of rotationally-resolved NdO LIF bands	108
5.2 Fitting results for the isotopically resolved rotational fit of the [20.82]4-X4 $v'' = 2$ transition	110
5.3 Vibrational parameter ω_e for the electronic ground X4 and low-lying states of NdO determined from dispersed fluorescence spectra	112
5.4 Molecular constants determined from rotational fits of SmO bands	150
5.5 Vibrational parameter ω_e for the electronic ground X0 ⁻ and low-lying states determined from dispersed spectra	123
5.6 Measured fluorescence lifetimes of SmO transitions	124
5.7 Determined Einstein coefficients A_{ij} for emissions observed in the [15.35]1-X0 ⁻ 0-0 DLIF spectrum	124
5.8 Hyperfine fitting results for the [15.35]1-X0 ⁻ 0-0 R lines	127
5.9 Einstein coefficients for the [15.03]state	136
5.10 Einstein coefficients for the [15.25] state	136
5.11 Einstein coefficients for the [15.43]0 ⁻ state	137
5.12 Einstein coefficients for the [15.35]1 $v = 1$ state	137
5.13 Einstein coefficients for the [17.21]2 state	137
5.14 Einstein coefficients for the [15.45] state	138

“This is the awe-inspiring universe of magic: there are no atoms, only waves and motions all around. Here, you discard all belief in barriers to understanding. You put aside understanding itself. This universe cannot be seen, cannot be heard, cannot be detected in any way by fixed perceptions. It is the ultimate void where no preordained screens occur upon which forms may be projected. You have only one awareness here – the screen of the magi: imagination! Here, you learn what it is to be human. You are a creator of order, of beautiful shapes and systems, an organizer of chaos.”

Frank Herbert, *Heretics of Dune*

Chapter 1

Introduction

1.1 Introduction

Physical, chemical, and optical properties of chemical systems are dictated by the motion of electrons in atomic or molecular systems known as the *electronic structure*. With the advent of quantum mechanics in the early 20th century, chemists have been able to predict the properties of chemical systems by describing the total energy of the system in terms of the electronic energy. In the early stages of quantum mechanics development, it was shown that particles possess a particle-wave duality and that their motion can be described in terms of a wavefunction $\psi(r,t)$, where the square of the wavefunction is the probability that a particle is at a given point in space. In 1936, Erwin Schrodinger introduced the notion that chemical systems can be described in terms of a Hamiltonian operator \hat{H} , which includes the total potential and kinetic energy of the system. This led rise to the time-independent Schrodinger equation¹

$$\hat{H}\Psi = E\Psi \quad (1.1)$$

which allows the energy E of a system to be determined by operating the Hamiltonian on the system's total wavefunction Ψ . In 1927, Max Born and J. Robert Oppenheimer² introduced the Born-Oppenheimer approximation, which allowed separation of electronic and nuclear wavefunctions on the basis that the much slower motion of the heavier nuclei can be considered stationary relative to the electronic motion. This allowed determination of the potential energy of a chemical system to be defined in terms of solely the electronic wavefunction. Modern electronic structure theory seeks to determine the energy of chemical systems by defining a Hamiltonian of the system, which is then operated on an approximate electronic wavefunction describing the chemical system. Trial wavefunctions can be altered until resulting energies converge to the true energy of the system.

One of the postulates of quantum mechanics states that if the wavefunction $\Psi(r, t)$ of a system is known, physical properties of that system can be determined³. If an approximate wavefunction is used, the value of the physical property will of course be approximate as well. Due to the Born-Oppenheimer approximation, only the electronic wavefunction is needed to describe the total wavefunction of the system, which negates the need for nuclear motion to determine physical properties of the systems. By using the electronic wavefunction of a system, physical properties which include but are not limited to the geometrical structure, thermochemistry, ionization energy, electron affinities, and dipole moments can be determined for a chemical system.

While many computational advances have been made in determining the electronic structure of chemical systems through solving the Schrodinger equation, electronic structure can also be determined experimentally through chemical spectroscopy. In the late 19th century, scientists were able to obtain emission spectra of atomic and molecular gases. These spectra were obtained by running a discharge through low-pressure chemical gases which produced discrete spectral lines at certain wavelengths. Niels Bohr in 1913 determined⁴ that these lines must be a result of electrons transitioning between discrete, quantized energy levels, with the energies of the photons emitted equal to the energy difference between the electronic states. Thus, the operating principle of spectroscopy was founded: by observing the energy of emitted photons, one can determine the electronic energy structure of a chemical system.

Today, spectroscopy is still a useful tool for electronic structure characterization of chemical systems. As the electronic structure of each chemical system is unique, the spectra corresponding to a chemical system will also be unique. Not only is spectroscopy useful in characterizing ground state characteristics of atomic and molecular systems but it can also be

used to characterize excited states, provide enough spectral emissions can be observed. Beyond electronic structure characterization, spectroscopy can also be analytically used in chemical systems to determine the chemical composition of systems with unknown chemical identities.

Experimental spectroscopy requires three components, the first being a light source. Traditionally, light sources used were broadband sources but the advent⁵ of the laser in 1960 permitted monochromatic, high intensity light sources with narrow linewidths. Laser spectroscopy has become its own field today, allowing characterization of electronic energy levels all the way down to hyperfine nuclear energy splitting. The second spectroscopy component, which is not always employed, is a method to disperse emitted light. This is commonly done with diffraction gratings in techniques like dispersed laser induced fluorescence (DLIF) in which emitted light is wavelength-selected by the angle at which light hits the diffraction grating. The final component is a detector to record either directly the emitted light or a physical result of the chemical system interacting with the excitation light. Common detectors include but are not limited to photomultiplier tubes (PMT), charged coupled devices (CCDs), and multi-channel plates (MCPs).

In this work, the electronic structure of small metal-containing molecules was characterized by employing laser spectroscopy methods including low- and high-resolution laser induced fluorescence (LIF), dispersed laser-induced fluorescence (DLIF), and fluorescence lifetime analysis. Spectroscopic results were complemented with electronic structure calculations and results are explained in a chemical model framework.

In Chapter 2, the experimental methods employed in this work will be discussed, the first of which will be laser ablation and supersonic expansions techniques. These techniques are commonly employed to generate gas-phase species as they can provide collision free

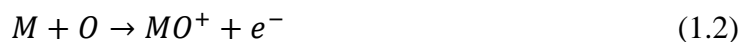
environments and cooled internal degrees of freedom of the target species^{6, 7}. Spectroscopic methods use to characterize the target molecule such as low- and high-resolution laser-induced fluorescence (LIF) along with dispersed laser induced fluorescence (DLIF) will then be discussed, both in their fundamental principles and the experimental setup used in this work. Finally, cation generation employing vacuum ultraviolet (VUV) single photon photoionization will be discussed, specifically in relation to the generation of lanthanide oxide cations in Chapter 5.

Chapter 3 is related to the spectroscopic characterization of small actinide molecules for both real world and fundamental applications. Actinide metals are commonly employed in nuclear reactors which generate large amounts of radioactive, toxic waste^{8, 9}. Scientists desire to be able to process the non-radioactive waste separately from its radioactive counterpart but extraction techniques¹⁰ require knowledge of the chemical bonding properties of actinide complexes. From a fundamental perspective, there exists little knowledge on the participation of the *5f* orbitals of actinides in chemical bonding^{11, 12}. Computational efforts on the electronic structure of actinide molecules is also challenging due to high-relativistic effects and a high-density of low-lying states¹³. Spectroscopically characterizing the electronic structure of small actinide molecules can reveal the extent of *5f* orbital involvement in chemical bonding as well as provide benchmarks for chemical calculations. Chapter 2 will detail the characterization of ThO and ThN through LIF and DLIF methods and compare the results to theoretically predicted molecular properties.

In Chapter 4, the electronic structure of CaO is discussed. There has been a long history on characterizing the complex electronic structure of CaO, whose excited states can be described in terms of extreme electronic location^{14, 15} on Ca⁺ and O⁻ centers. CaF and NaO orbitals are used

to model the Ca^+ and NaO^- centers and CaO excited states are described in terms of the CaF and NaO orbitals from which they arise. There were two motivations for this work, the first being the search for the hypermetallic CaOCa . While CaOCa was not observed, CaO transitions involving vibrational excited levels of the $A^1\Pi(X\sigma\pi^{-1})$ state were observed, allowing further characterization of this state. The second motivation concerned a perturbation of the $C^1\Sigma^+(B\sigma\sigma^{-1})$ - $X^1\Sigma^+$ 7-0 band by a nearby $\Omega = 0^+$ state, which was unable to be electronically assigned in past work. With DLIF techniques available, this work was able to assign this perturbing state as the $g^3\Pi(0^+)(B\sigma\pi^{-1}) \nu = 12$ state. Chapter 4 details these analyses.

Finally, in Chapter 5, the spectroscopic characterization of lanthanide metal oxides and cations are discussed in relation to United States Air Force (USAF) space cloud launches^{16, 17}. To improve radio wave communications, the USAF desired to artificially increase the atmospheric electron density through the chemi-ionization of lanthanide metals. In this process, the lanthanide metal M reacts with atmospheric oxygen O to produce the lanthanide oxide cation MO^+ along with an excess electron.



The USAF has conducted launches, where they have released 10 kg of either neodymium (Nd) or samarium (Sm) metal into the atmosphere and have recorded the emission profiles of the launches¹⁶. Broad emission profiles were observed in the visible spectral region but due to the lack of spectroscopic characterization of SmO and NdO and their cations, it is unclear to whether the chemi-ionization process occurred during the launches. In this work, NdO and SmO have been characterized through LIF and DLIF techniques to assist with space cloud characterization. Attempts were made to produce NdO^+ and SmO^+ through photoionization but no LIF transitions were observed, possibly due to poor photoionization or searching in the incorrect spectral region.

Emission spectra of the lanthanide-based supersonic expansion upon excitation with the ArF photon were taken to confirm space launch results and these results are detailed in Chapter 5.

1.2. Chapter 1 References

1. Schrodinger, E., An Undulatory Theory of the Mechanics of Atoms and Molecules. *Phys. Rev.* **1926**, 28, 1049.
2. Born, M.; Oppenheimer, R., Zur Quantentheorie der Molekeln. *Annalen der Physik* **1927**, 389 (20), 457-484.
3. Dirac, P., *The Principles of Quantum Mechanics*. 1930.
4. Bohr, N., I. On the constitution of atoms and molecules. *The London, Edinburgh, and Dublin Philosophical Magazine and Journal of Science* **1913**, 26 (151), 1-25.
5. Maiman, T. H., Stimulated Optical Radiation in Ruby. *Nature* **1960**, 187 (4736), 493-494.
6. Duncan, M. A., Invited Review Article: Laser vaporization cluster sources. *Review of Scientific Instruments* **2012**, 83 (4), 041101.
7. Morse, M., Supersonic Beams. In *Experimental Methods in the Physical Sciences*, Elsevier: 1996; Vol. 29, pp 21-47.
8. Runde, W.; Neu, M. P., Actinides in the Geosphere. Springer Netherlands: 2010; pp 3475-3593.
9. Vermeul, V. R.; Fruchter, J. S.; Fritz, B. G.; Mackley, R. D.; Wellman, D. M.; Williams, M. D., *In-Situ Uranium Stabilization Through Polyphosphate Injection: Pilot-Scale Treatability Test at the 300 Area, Hanford Site - 8187*. In *WM2008*, Phoenix, AZ, 2008.
10. Nash, K. L.; Madic, C.; Mathur, J. N.; Lacquement, J., Actinide Separation Science and Technology. In *Chemistry of the Actinide and Transactinide Elements*, Springer: Berlin, 2006; Vol. 4, pp 2622-2798.

11. Crosswhite, H. M.; Crosswhite, H.; Carnall, W. T.; Paszek, A. P., Spectrum analysis of $U^{3+}:\text{LaCl}_3$. *The Journal of Chemical Physics* **1980**, *72* (9), 5103-5117.
12. Choppin, G. R., Covalency in f-element bonds. *Journal of Alloys and Compounds* **2002**, *344* (1-2), 55-59.
13. Dolg, M.; Cao, X., Relativistic Pseudopotentials: Their Development and Scope of Applications. *Chemical Reviews* **2012**, *112* (1), 403-480.
14. Norman, J. B.; Cross, K. J.; Schweda, H. S.; Polak, M.; Field, R. W., The $\text{CaO } c^3\Sigma^+ - a^3\Pi_i(0,0)$ band. *Molecular Physics* **1988**, *66* (1), 235-268.
15. Baldwin, D. P.; Hill, E. J.; Field, R. W., Electron affinity of O- and diabatic $\text{CaO}(g)$ integer charge potential curves. *Journal of the American Chemical Society* **1990**, *112* (25), 9156-9161.
16. Holmes, J. M.; Dressler, R. A.; Pedersen, T. R.; Caton, R. G.; Miller, D., A combined spectroscopic and plasma chemical kinetic analysis of ionospheric samarium releases. *Radio Science* **2017**, *52* (5), 521-538.
17. Shuman, N. S.; Hunton, D. E.; Viggiano, A. A., Ambient and Modified Atmospheric Ion Chemistry: From Top to Bottom. *Chemical Reviews* **2015**, *115* (10), 4542-4570.

Chapter 2

Experimental Techniques

2.1 Laser Ablation and Supersonic Expansion

In this work, laser ablation and supersonic expansion techniques were coupled to generate the desired diatomic MX in the gas-phase. Laser ablation is a commonly employed technique¹ for metal-containing molecule or cluster generation as it does not require extreme working conditions or thermal energies above room temperature, unlike discharge or thermally heated oven sources. Another advantage of laser ablation is that the metal production quantity can be easily controlled by controlling the output power of the ablation laser. A variety of metal sources not limited to but including metal rods, films, and metal disks can be used with laser ablation. An advantage of metal rods as ablation sources is that the rods can be continuously rotated and translated, ensuring a fresh ablation surface for each pulse. Metal rods are also advantageous to use as rods with certain diameters and lengths are readily available from retailers.

Supersonic expansions are a common method employed in gas-phase spectroscopy to obtain a molecular beam with a low-internal temperature, which greatly reduces spectral congestion². In these expansions, a high-pressure gas, undergoing many collisions, is expanded into a vacuum through a small orifice. Once the gas enters the vacuum through the orifice, the number of collisions is greatly reduced which limits the velocity distribution and consequently the translational energy of the molecular gas jet. In the early stages of the expansions, i.e. close to the orifice, the molecular collisions result in the cooling of the vibrational and rotational degrees of freedom of the molecule³. This is specifically important for spectroscopists since the cooling of the vibrational and rotational temperature of the molecule limits spectra congestion and facilitates the rovibrational characterization of the molecular beam. While the rotational temperature is almost always cooled, cooling of the electronic and vibrational states is dependent

on the energy spacing between the states. It is not at all uncommon to see rotationally cooled but vibronically excited molecules in supersonic expansions. Supersonic expansions are often coupled with laser ablation to generate low-internal energy, rotationally cooled metal-containing molecules and clusters.

In this work, to produce the desired molecule, a 0.25" diameter metal rod was coupled to a 3D-printed (Original Prusa i3 MK3S, PC-blend filament) ablation block, which is shown in Figure 2.1.

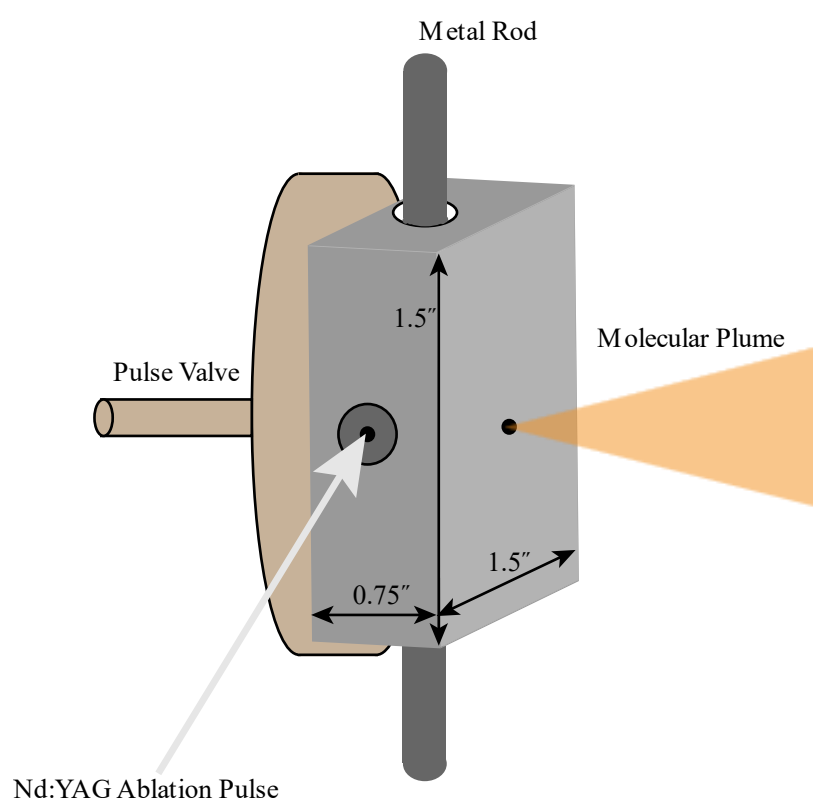


Figure 2.1. Ablation and supersonic expansion experimental design.

Initially, the ablation block was machined out of stainless steel, but it was found that aluminum clusters could be produced in the laser ablation process, whose chemiluminescence could be detected in the dispersed fluorescence measurements. A switch to carbon-based 3D printed blocks was initiated, as carbon clusters were less likely to be formed from the ablation process

and 3D printing the ablation block was much less time consuming as opposed to machining the block. The ablation block was designed with a 0.30" diameter orifice for the metal rod, as well as an inlet perpendicular to the rod for the ablation pulse, allowing the pulse diameter to be narrowed from 0.45" to 0.10". Inside the ablation block, the metal rod was coupled to two stepper motors which continuously translated and rotated the rod. The metal was ablated with pulsed 1064 nm light from a Nd:YAG laser (QuantaRay, DCR 1A) which was focused onto the rod using a 30 cm focal length lens. The plane polarized output from the Nd:YAG laser was attenuated to the 1-10 mJ/pulse range by means of a Glan-Taylor prism housed in a rotatable stage (Thorlabs CCM1-PBS25-1064- HP/M).

To produce the desired molecule, the metal vapor was then entrained in a gas mixture containing He and either an oxygen- or nitrogen-containing gas for oxide or nitride generation, respectively. Gas pulses were generated by a pulse valve (Parker-Hannifin General Valve Series 9) mounted to the back end of the ablation block and the durations of the gas pulses were varied from 230 μ s to 1 ms depending on the molecule desired. Table 2.1 lists the optimal gas mixtures, backing pressures, and pulse durations for the diatomic molecules produced in this work.

Table 2.1. Gas expansion conditions for optimal production of MX species.

MX Diatomic	Gas Mixture	Backing Pressure (psi)	Pulse Duration (μ s)
CaO	1% O ₂ /He	200	1000
NdO	1% N ₂ O/He	120	230
SmO	1% N ₂ O/He	120	330
ThN	1% NH ₃ /He	120	390
ThO	He	120	350

After passing through a 0.75" reaction channel, the entrained metal vapor-gas mixture was supersonically expanded through a 3 mm diameter orifice into a vacuum chamber. The vacuum was maintained by a Roots blower (Leybold, RUVAC WSU 251) backed by a rotary

vane pump (Leybold, TRIVAC D65B) and the average background pressure in the chamber was typically less than 100 mtorr under gas loading, such that a Campargue⁴ expansion was formed. Molecules in the expansion were typically cooled down to rotational temperatures of 10-90 K.

2.2 Laser-induced Fluorescence (LIF)

2.2.1. Overview of LIF

Laser-induced fluorescence (LIF) is a commonly employed spectroscopic technique for obtaining structural information and chemical dynamics⁵ of atomic and molecular species. The operating principle of LIF is quite simple⁶ and is illustrated in Figure 2.2 for a diatomic molecule AB.

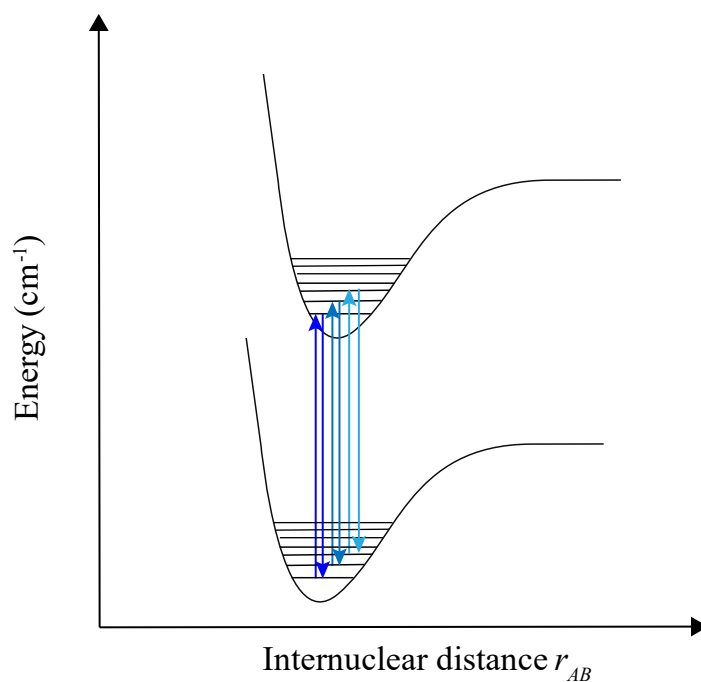


Figure 2.2. Laser-induced fluorescence (LIF) in a diatomic molecule AB.

In LIF, a laser with some frequency ν is tuned to an absorption line in the desired chemical species. Upon absorption of the photon, the species is electronically excited to an upper state, with some lifetime τ . The species then spontaneously radiates down to a lower state, emitting a photon with a frequency equal to the radiation energy. Emitted photons are then detected

typically with a photomultiplier tube (PMT), which amplifies the photon signal through electron multiplication. When the electronic structure of a species is unknown, the laser frequency can be stepped, and the chemical species will be excited by the laser photon each time the laser photon frequency is resonant with an absorption transition. By measuring the fluorescence as a function of the excitation energy, one can obtain an emission spectrum revealing the internal energy structure of the desired chemical species.

Employing LIF has many advantages over using absorption techniques⁷. The first advantage is that no background subtraction is needed. With LIF, there will be an absence of signal if the incident photon is not resonant with an internal transition. This results in a great detection sensitivity in LIF. Another advantage with LIF is that the fluorescence can be collected orthogonal to the incident laser. This allows 2D and 3D imaging of the fluorescence which is quite useful in techniques⁸ like 2D-LIF, in which the fluorescence is monitored as a function of both the incident photon and emission photon energies.

In this work, both low-resolution and high-resolution LIF was used to characterize the rovibronic and hyperfine structure of the desired diatomic molecules as well as the lifetime of the upper transition states. The following sections detail the experimental setups for acquiring the low- and high-resolution laser-induced fluorescence.

2.2.2 Low-Resolution LIF Experimental Setup

Figure 2.3 shows a diagram of the low-resolution LIF experimental setup.

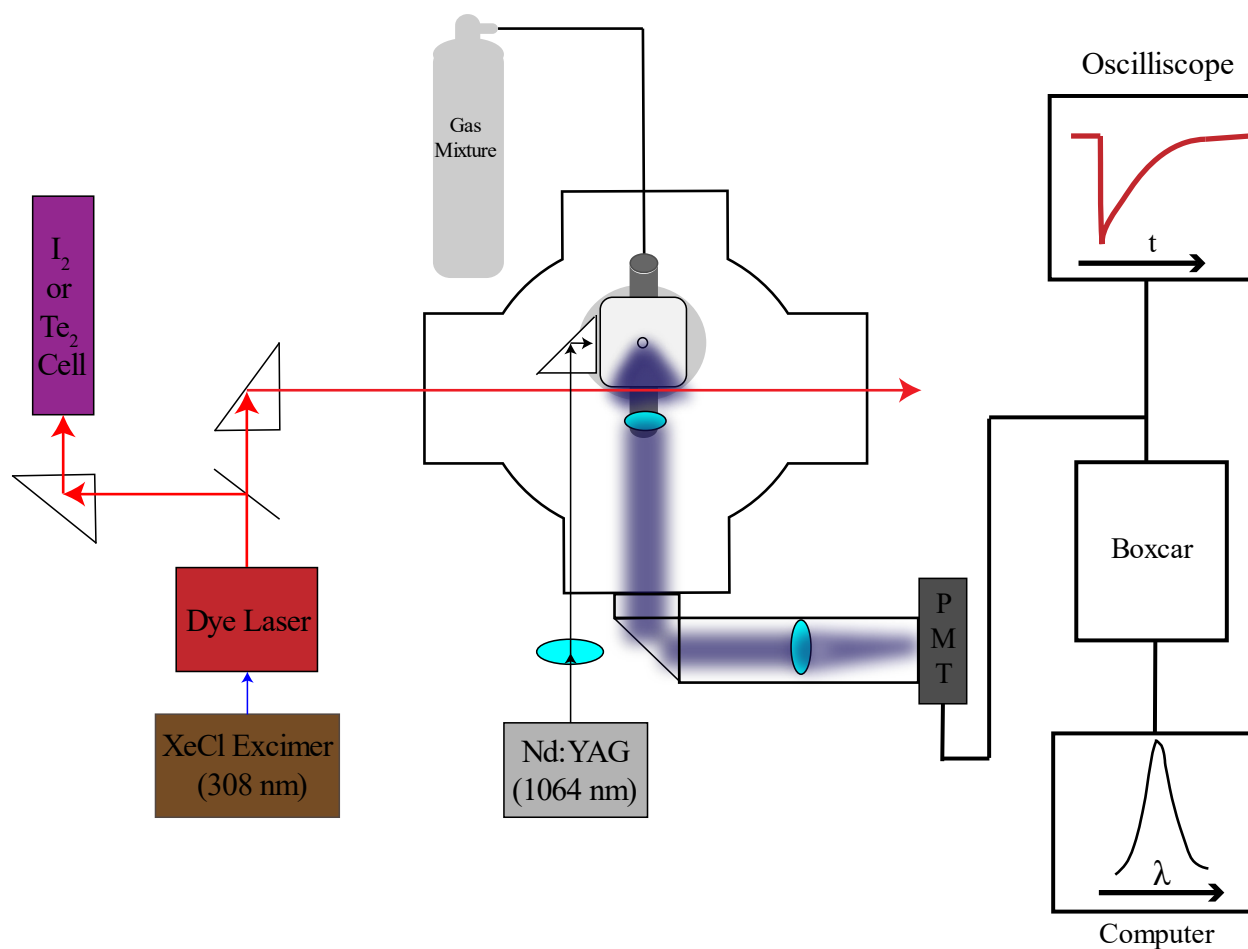


Figure 2.3. Experimental setup for the low-resolution laser-induced fluorescence (LIF) collection and processing.

Ablation products were probed with a pulsed tunable dye laser (Lambda-Physik, FL3002e), pumped by a 308 nm XeCl excimer (Lambda-Physik, Compex Pro 201), with a pulse repetition frequency of 10 Hz, nominal pulse duration of 10 ns and linewidth (FWHM) of 0.3 cm^{-1} . Two 4-channel digital delay generators (DDG) were used to control the timings between the ablation and probe lasers, as well as the data collecting equipment (Quantum Composers Model 9614 and Stanford Research Systems DG535). For the recording of rotationally resolved data, the linewidth was reduced to 0.06 cm^{-1} by adding an intracavity etalon. The laser light was sent into the vacuum chamber perpendicular to the supersonic expansion, roughly 3 cm from the

expansion nozzle. The fluorescence orthogonal to both the probing laser and expansion was collimated (Thorlabs, focal length $f = 6$ cm, diameter $D = 5.1$ cm) and focused (Thorlabs, $f = 25$ cm $D = 5.1$ cm) onto a photomultiplier tube (Hamamatsu R955) outside of the chamber. A long-pass filter with a cut-on wavelength 20 nm longer than the laser light was attached to the PMT to reduce laser scatter. The signal from the PMT was amplified using an DC-300 MHz amplifier (Stanford Research Systems, SR445) and then sent to both an oscilloscope (Tektronix TDS 2014) and a boxcar integrator (Stanford Research Systems, SRS 250). For lifetime measurements, the fluorescence decay curve was signal averaged for 256 laser pulses and then downloaded directly from the oscilloscope. Background measurements were taken without the dye laser entering the chamber and were then subtracted from the fluorescence decay curves to correct for the chemiluminescence of the ablation products. To record LIF spectra, voltage readings from the boxcar were digitized by a National Instruments Data Acquisition Device (NI DAQ) which was also used to step the dye laser in 0.003 nm increments and record 30 averages at each wavelength step.

The absolute wavenumber calibration was established by recording either the absorbance spectrum of $^{130}\text{Te}_2$ for photon energies of 18,500-20,000 cm^{-1} or the fluorescence spectrum of I_2 for energies of 15,600-20,000 cm^{-1} . To obtain the absorbance spectrum of $^{130}\text{Te}_2$, a sealed cell containing ^{130}Te was heated in an oven to 650°C to produce a sufficient vapor pressure of Te_2 . After passing through the vacuum chamber, the dye laser beam was directed through the cell. A photodiode was used to detect $^{130}\text{Te}_2$ *A-X* and *B-X* absorbance, averaging 30 laser pulses for each wavelength step. Absorbance spectra were fit to the line positions of a standard spectral atlas⁹ for Te_2 . For wavenumber calibration using I_2 fluorescence, the dye laser was directed through a cell containing iodine vapor, exciting the I_2 *B-X* spectrum, and the resulting fluorescence

perpendicular to the laser was recorded with a photomultiplier tube (Hamamatsu R955). Spectra were fitted to the I_2 spectral transition energies of Salami and Ross¹⁰. For the characterization of CaO, some UV states were accessed by frequency-doubling the output of the dye laser using an angle-tuned BBO crystal (Lambda-Physik, FL30). In this case, the I_2 $B-X$ fluorescence was stimulated by only sending the dye laser fundamental through the iodine cell.

2.2.3. High-Resolution LIF Experimental Setup

The high-resolution LIF experiments were performed in a different chamber than the low-resolution work in Section 2.2.2. In the high-resolution experiments, the second harmonic of a Nd:YAG (532 nm, 20 Hz, New Wave Tempest) was used to ablate a metal rod which was then expanded in the desired gas mixture. Gas pulses were supplied by a solenoid pulse valve (Parker Precision Fluid Corp, Series 9) at a backing pressure of 600 psi. The supersonic expansion was then skimmed to produce a well collimated molecular beam, using an adjustable iris ($d = 2.5$ cm) placed 5 cm downstream from the expansion orifice. In high-resolution experiments, skimming the beam is important as it reduces the spread of molecular velocities, which in turn reduces Doppler broadening of the beam. The reaction chamber was pumped by rotary and diffusion pumps, maintaining a constant background pressure of 80 microtorr. For high-resolution LIF measurements, the molecular beam was excited by a single-frequency continuous wave ring dye laser (Coherent 899) pumped by a 532 nm diode-pumped solid-state laser (Coherent Verdi-V10) with an operating power of 5W. The dye laser has a linewidth of ~ 1 MHz and typically laser powers of 100-150 mW entered the chamber. The resulting LIF signal was focused onto a cooled PMT (Hamamatsu R093) and collected using a gated photon counter (Stanford Research System SR400).

For absolute wavelength calibration of the high-resolution spectra, laser light from the ring laser was sent through a wavemeter (Burleigh, WA-1500) with a built-in HeNe laser wavelength standard with an absolute wavelength precision of $\pm 0.002 \text{ cm}^{-1}$. For further absolute wavelength calibration, the wavenumber of the laser was calibrated to $\pm 0.0001 \text{ cm}^{-1}$ by recording the sub-Doppler absorption spectrum¹¹ of molecular iodine. Figure 2.4 shows the setup for acquiring the sub-Doppler spectrum.

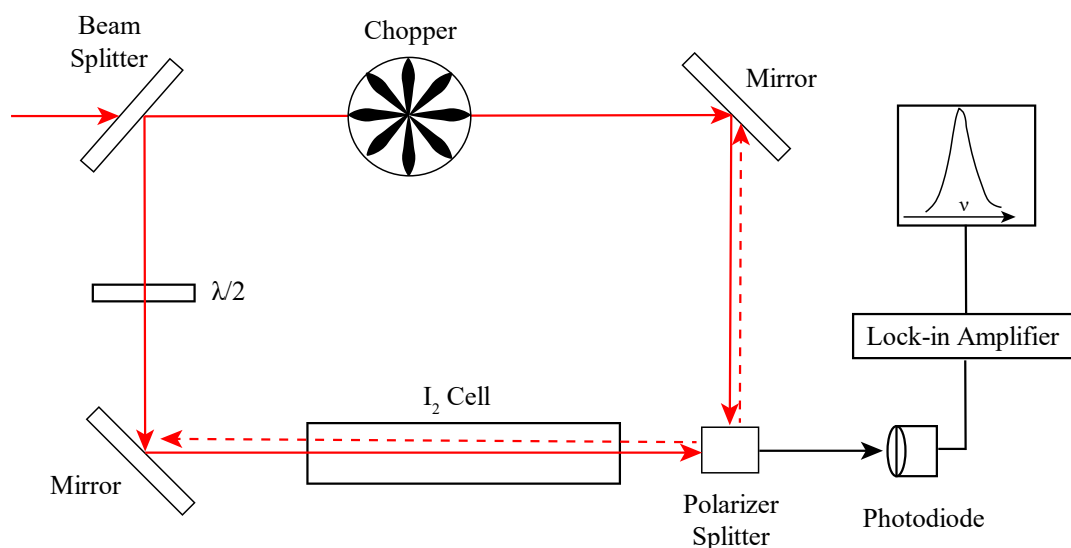


Figure 2.4. Experimental setup for the sub-Doppler absorbance spectrum of iodine.

In sub-Doppler absorbance spectroscopy¹², Doppler broadening is countered through velocity selection, in which molecules only belonging to a velocity spread are excited by counter-propagating beams. A strong intensity pump beam saturates a molecular absorbance transition, exciting only a narrow velocity spread of molecules on axis with the pump beam. If the strong pump and weak probe beams have the same frequency, only molecules with the same velocities will interact with both the beams. This results in a molecular velocity spread that is very narrow and centered around zero. When the molecules interact with the weak probe beam, the pump beam experiences a reduction in absorbance as those molecules are not available to be excited by

the pump beam. This creates a narrow dip in the Doppler-broadened absorbance line. To separate the dip from the Doppler-broadened background signal, the pump beam is chopped at frequencies on the order of kilohertz and the background-free signal is obtained with a lock-in amplifier.

In this work, light from the single-frequency ring dye laser was divided into two nearly equal intense beams using a cube beam splitter. The two beams were then passed through a heated (313 K) iodine cell in opposite directions. A mechanical chopper with a frequency of 1970 Hz was used to chop one beam, after which the beam passed through a polarizer splitter. The other beam was sent through a 90° polarizer rotator, denoted as " $\lambda/2$ " in Figure 2.4. When molecules with the same velocity in the iodine cell simultaneously interacted with the counter polarized laser beams, modulated signal was detected by the photodiode. The output signal from the photodiode was then sent to a lock-in amplifier (EG&G 5207). To interpolate between I_2 absorbance lines, a plano-flat etalon with a free spectral range of 315 MHz was used.

2.3 Dispersed Laser-Induced Fluorescence (DLIF)

One issue with resonant laser-induced fluorescence is that photons of all energies are detected at a specific excitation photon energy. This can be a problem if different chemical species fluorescence at the same excitation energy and one is only interested in the fluorescence of a single chemical species. To remedy this issue, one can disperse the emitted fluorescence. Figure 2.5 shows the operating principle of DLIF.

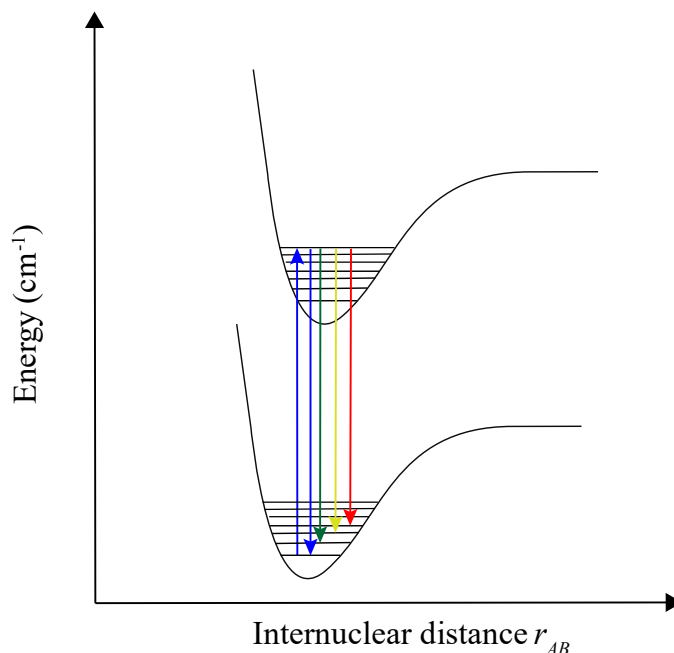


Figure 2.5. Illustration of dispersed laser-induced fluorescence (DLIF).

In DLIF, the excitation photon is fixed to be resonant with an absorption transition, which results in emission to lower states. Photons release in the emission process are then dispersed with a monochromator equipped with a diffraction grating¹³, which is a multi-slit surface which disperses light based on the incident angle. By adjusting the angle at which the light entering the monochromator hits the diffraction grating, photons with a single energy will leave the monochromator to be detected by a PMT, allowing observation of single energy emission. DLIF spectra are generated by recording the fluorescence as a function of wavelength.

The application for dispersed fluorescence is two-fold. First, it allows a simplification of the spectral analysis. As there is no inherent capability of mass-selection in LIF, it is common for different chemical species to fluoresce at the same excitation energy. Species with weaker emission intensities than others can cause the noise baseline level to rise in emission spectra or emissions may overlap, resulting in the broadening of spectral features which may complicate the analysis of the emission spectrum. If one knows an emission energy in the desired molecule,

the fluorescence can be directed through a monochromator at that emission wavelength, which prohibits molecules emitting at different wavelengths from being detected. One can then step the excitation energy while observing the fluorescence through a monochromator to obtain an emission spectrum corresponding to the internal energy of solely the desired molecule.

The second application of dispersed fluorescence is that it allows for characterization of the vibronic structure of molecules. DLIF spectra plotted as a function of the relative energy to the excitation photon can reveal to which state the molecule emits. This can result in the observation of emissions to low-lying electronic states and well as emissions to different vibrational levels of the same electronic states, whose energy separations can be used to determine vibrational parameters specific to that electronic state. As most of the population of jet-cooled molecules resides in the ground electronic state, the dispersed fluorescence spectra often reveal emissions to vibrationally excited levels of the ground electronic state. This allows vibrational characterization of the ground electronic state which is highly important for providing benchmarks for theoretical methods. Furthermore, the relative intensities of the emissions observed in DLIF spectra can be used along with a lifetime measurement of the upper state to determine Einstein coefficients A_{ij} since the fluorescence intensities are directly related to the molecular population emitting from the upper state to the lower energy states.

In this work, DLIF was used to vibronically characterize the desired diatomic molecules and Figure 2.6 shows the DLIF acquisition setup. The DLIF experiments were performed in the same chamber as the low-resolution LIF in section 2.2.2.

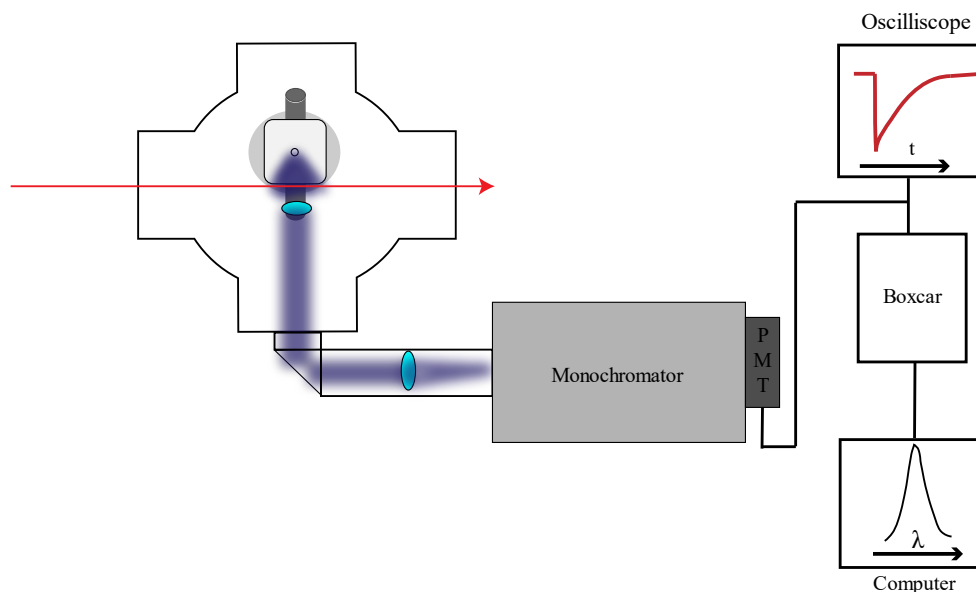


Figure 2.6. Experimental setup for acquisition of dispersed laser-induced fluorescence (DLIF) spectra.

For dispersed fluorescence measurements, the fluorescence orthogonal to the expansion was collimated and focused through the entrance slits of a monochromator (Instruments SA, 0.64m, $f/5.8$) equipped with a 1200mm/groves diffraction grating. Light exiting the monochromator was detected by a PMT (Hamamatsu R955). Digital signal was generated in the same way as the LIF spectra by integrating the dispersed fluorescence with a boxcar and then digitizing the signal with the NI-DAQ.

DLIF spectra were taken by exciting the most intense rotational feature of the desired vibronic transition and then scanning the monochromator by using a stepper motor to drive the diffraction grating. The monochromator was swept over the spectral range of 400-900 nm. Relative emission intensities were adjusted to compensate for the wavelength dependent PMT efficiency. Referring to the Hamamatsu R955 PMT datasheet, values of the cathode radiant sensitivity of the PMT at wavelengths ranging from 400-900 nm were fit to a cubic function which was then applied to the DLIF emission intensities. In order to subtract any laser scatter

from the DLIF spectrum, the scan over the emission resonant to the pump energy was repeated but with the laser parked off-resonance. This off-resonance scan was then subtracted from the on-resonance DLIF spectrum.

2.4 Vacuum Ultraviolet (VUV) Single-Photon Ionization

Photoionization is the process in which the cation of an atom or molecule is produced by ejecting an electron from the neutral species through interaction with a photon¹⁴.

Photoionization methods are particularly advantageous over other ionization methods such as flash lamps and discharges as the ionization energy is much more tunable and selective.

Depending on the energy of the photon, one can produce cations by emitting core or valence electrons by employing X-ray or ultraviolet photons, respectively. Vacuum ultraviolet (VUV) photons are commonly employed for cation production as they have enough energy to remove valence electrons without fragmenting the molecule or ionizing any present background gases¹⁵.

The photoionization efficiency is related to the photoionization cross section, which is directly related to the energy of the photon¹⁶. As the cross section is largest at the ionization threshold, it is advantageous to choose a photon energy that is at or higher than the ionization threshold energy. In relation to the production of lanthanide oxide cations in Chapter 5, an ArF (6.42 eV) excimer laser was chosen as the photoionization source as its energy is relatively close to the ionization threshold^{17, 18} of both NdO (5.55 eV) and SmO (5.64 eV). The pulsed 193 ArF excimer laser (Lambda-Physik, Compex 205) with a pulse repetition frequency of 10 Hz and maximum output energy of 500 mJ/pulse was focused (Thorlabs, $f = 752.6$ mm) into the chamber, with the focal point being 3 cm from the expansion nozzle. The ArF pulse was counter-propagated to the dye laser and fired 600 ns to 1.5 μ s before the dye laser to allow the strong

fluorescence produced by the excimer laser to decay. LIF and DLIF spectra of the cations were obtained by the methodology described above.

In order to further characterize the emissions observed in the space cloud experiments caused by solar excitation, the supersonic expansion was excited with the 193nm ArF light and the resulting dispersed fluorescence spectra were recorded from 400-900 nm. To determine whether observed emissions were atomic or molecular, backing gases of either pure He or 1% N₂O/He were chosen for individual acquisitions of the DLIF spectra. Spectra with the ArF laser focused and unfocused were also acquired, allowing determination of whether emissions were caused by species formed in the earlier or later stages of the expansion. This would reveal whether emissions came from cooled species with very little translational energy or collisionally-formed species with high temperatures.

2.5 Chapter 2 References

1. Duncan, M. A., Invited Review Article: Laser vaporization cluster sources. *Review of Scientific Instruments* **2012**, 83 (4), 041101.
2. Morse, M., Supersonic Beams. In *Experimental Methods in the Physical Sciences*, Elsevier: 1996; Vol. 29, pp 21-47.
3. Levy, D. H., The Spectroscopy of Very Cold Gases. *Science* **1981**, 214 (4518), 263-269.
4. Beijerinck, H. C. W.; Van Gerwen, R. J. F.; Kerstel, E. R. T.; Martems, J. F. M.; Van Vliembergen, E. J. W.; Smits, M. R. T.; Kaashoek, G. H., Campargue-Type Supersonic Beam Sources: Absolute Intensities, Skimmer Transmission and Scaling Laws for Mono-Atomic Gases He, Ne, and Ar. *Chemical Physics* **1985**, 96, 153-173.
5. Schultz, A.; Cruse, H. W.; Zare, R. N., Laser-Induced Fluorescence: A Method to Measure the Internal State Distribution of Reaction Products. *The Journal of Chemical Physics* **1972**, 57 (3), 1354-1355.
6. Kinsey, J. L., Laser-Induced Fluorescence. *Ann. Rev. Phys. Chem.* **1977**, 28, 349-372.
7. Zare, R. N., My Life with LIF: A Personal Account of Developing Laser-Induced Fluorescence. *Annual Review of Analytical Chemistry* **2012**, 5 (1), 1-14.
8. Gascooke, J. R.; Lawrance, W. D., Two dimensional laser induced fluorescence in the gas phase: a spectroscopic tool for studying molecular spectroscopy and dynamics. *The European Physical Journal D* **2017**, 71 (11).
9. Cariou, J. L. P., *Atlas du spectre d'absorption de la molecule de tellure*. Laboratoire Aime-Cotton: Orsay (France), 1980.
10. Salami, H.; Ross, A. J., A molecular iodine atlas in ascii format. *Journal of Molecular Spectroscopy* **2005**, 233, 157.

11. Salumbides, E. J.; Eikema, K. S. E.; Ubachs, W.; Hollenstein, U.; Knöckel, H.; Tiemann, E., The hyperfine structure of $^{129}\text{I}_2$ and $^{127}\text{I}^{129}\text{I}$ in the $\text{B}^3\Pi_{0u^+}-\text{X}^1\Sigma_g^+$ band system. *Molecular Physics* **2006**, *104* (16-17), 2641-2652.
12. Hänsch, T. W.; Levenson, M. D.; Schawlow, A. L., Complete Hyperfine Structure of a Molecular Iodine Line. *Physical Review Letters* **1971**, *26* (16), 946-949.
13. Bonod, N.; Neauport, J., Diffraction gratings: from principles to applications in high-intensity lasers. *Advances in Optics and Photonics* **2016**, *8* (1), 156.
14. Hollas, J. M., Photoelectron spectroscopy. In *High Resolution Spectroscopy*, Butterworth & Co London, 1982; pp 435-480.
15. Eschner, M. S.; Zimmermann, R., Determination of Photoionization Cross-Sections of Different Organic Molecules Using Gas Chromatography Coupled to Single-Photon Ionization (SPI) Time-of-Flight Mass Spectrometry (TOF-MS) with an Electron-Beam-Pumped Rare Gas Excimer Light Source (EBEL). *Applied Spectroscopy* **2011**, *65* (7), 806-816.
16. Green, J. C.; Decleva, P., Photoionization cross-sections: a guide to electronic structure. *Coordination Chemistry Reviews* **2005**, *249* (1-2), 209-228.
17. VanGundy, R. A.; Persinger, T. D.; Heaven, M. C., Low energy states of NdO^+ probed by photoelectron spectroscopy. *The Journal of Chemical Physics* **2019**, *150* (11), 114302.
18. Cox, R. M.; Kim, J.; Armentrout, P. B.; Bartlett, J.; Vangundy, R. A.; Heaven, M. C.; Ard, S. G.; Melko, J. J.; Shuman, N. S.; Viggiano, A. A., Evaluation of the exothermicity of the chemi-ionization reaction $\text{Sm} + \text{O} \rightarrow \text{SmO}^+ + \text{e}^-$. *The Journal of Chemical Physics* **2015**, *142* (13), 134307.

Chapter 3

Characterization of the Low-Lying States of ThO and ThN

The contents and figures of this chapter are reprinted or adapted with permission from Schmitz, J.R., Kaledin, L.A., Heaven, M.C. Laser-induced fluorescence spectroscopy of jet-cooled ThO. *J. Mol. Spec.* **2019**, *360*, 39-43.

and

Schmitz, J. R., Heaven, M.C. Spectroscopy and electronic structure of the low-energy states of ThN. *J. Mol. Spec.* **2021**, *377*, 111426.

3.1. Introduction

3.1.1 Motivation for Electronic Structure Characterization of Actinides

Characterizing the electronic structure and bonding properties of actinides is of interest both from practical and fundamental perspectives. Since their recent discovery, actinides have been used as nuclear fission sources both in nuclear power generators and nuclear weaponry¹. Uranium (U) and thorium (Th) are typically used in nuclear reactors as they are the two naturally most-abundant actinides and readily undergo nuclear fission. An issue, however, with nuclear reactors is the radioactive waste that is generated. In U-based reactors, the radioactive ²³⁵U is chosen as the fission source, which decays into radioactive products. These fission products, while only comprising a small portion (3%) of the spent nuclear fuel (SNF) of the reactors, increases the radioactivity and radiotoxicity of the SNF. While the majority of the spent SNF is typically non-fissile ²³⁸U, ²³⁸U can alpha decay into radioactive products which further increases the radiotoxicity of the SNF. Recently, the drive to switch to Th-based reactors has been initiated, partly due to the greater natural abundance of thorium but also because the thorium-decay process generates far less long-lived radioactive products, reducing the long-term radiotoxicity of thorium-based SNF. However, regardless of the fission source, SNF is radiotoxic and there is a need for a safe, cost-effective, long-term storage solution.

Currently, SNF is stored in large tanks both on and off reactor sites. However, since SNF is acidic, there have been reported cases of nuclear fuel leaking out of the tanks and into the environment, increasing the radiotoxicity of the local environment. One instance of this problematic situation occurred at the waste facility in Hanford, WA, USA^{1,2} where 67 tanks containing SNF developed leaks, leaking 4 million liters of waste containing over 100 kCi of radioactive actinides in the surrounding soil and groundwater. To prevent instances like these

from occurring again, chemists desire to be able to extract the radioactive waste from its non-radioactive counterpart so that the processing of the radioactive waste can be done on a smaller, safer scale. However, the chemical knowledge of actinide bonding needed to be able to extract actinides out of solution is lacking. Characterizing the electronic structure of small actinide molecules can reveal insight to the nature of actinide bonding and assist in developing chemical methods for actinide extraction from SNF.

As actinides are radioactive, there is an advantage to studying their electronic structure through computational chemistry. However, actinide calculations present their own problems. Due to the large nuclear charge Z of actinides, the electrons experience high relativistic effects as they approach the nucleus. Modelling the relativistic effects can prove to be a challenge. To mitigate this problem, effective core potentials (ECPs)³ are often introduced, replacing the inner most core electrons with a potential energy function. This allows only the valence electrons to be considered, which greatly reduces the cost of the calculation and allows the relativistic effects to be limited to the core electrons. Another problem with modelling actinides is that they have a high density of low-lying excited states which exhibit strong spin-orbit effects. This results in the mixing of ground and low-lying electronic states, giving the ground state multi-reference character⁴, which increases the difficulty of the computational modelling. A common solution is to employ semi-empirical methods, such as multi-configurational ligand field theory (LFT-CI), to characterize the ground and low-lying states. Of course, experimental data is needed for such methods. Experimentally characterizing the electronic structure of actinides can prove benchmarks for the challenging calculations and can be used to evaluate the computational models.

From a fundamental chemistry perspective, actinides are of interest due to the question of the involvement of the $5f$ orbitals in chemical bonding. In lanthanides, the $4f$ orbitals are compact and do not participate in chemical bonding but rather function like core orbitals. This leads to the chemistry of lanthanides being very homogenous⁵, changing little as the nuclear charge Z increases. With actinides, however, it is less clear to the extent of bonding in which the $5f$ participate. The $5f$ orbital is much less compact⁶ than the $4f$ orbital and lies similar in energy to the $6d$ orbital and $7s$ orbital. This allows the $5f$ orbital to be available for bonding under preferable conditions. Theory⁷ predicts that the $5f$ orbital actively participates in bonding in the actinide series up to americium (Ac), after which the $5f$ orbital contracts and becomes a bonding spectator, much like in the case of the lanthanides. However, there is a lack of experimental data to confirm this kind of behavior. The covalency of actinides is also not a purely fundamental issue but also one of practicality. In advanced nuclear fuel cycles, there is an industrial need to separate trivalent trans-plutonium actinides from their trivalent lanthanide fission counterparts⁸. This process is difficult to perform since hard oxygen-donor ligands conventionally used do not preferentially bond to actinides or lanthanides due to their similar ionic behavior. However, it is believed that soft oxygen-donor ligands^{9, 10} would prefer the actinides due to the greater covalent nature of the actinide-ligand bonds. Determining the covalency of the actinides will not only allow insight into the nature of actinide bonding but will also support actinide extraction methods in nuclear waste.

The electronic structure of small actinides can also be used to test fundamental physics properties. The degree of asymmetry¹¹⁻¹⁴ of matter and anti-matter in the known universe is a pressing matter in fundamental physics, as the Standard Model (SM) incorrectly predicts the excess amount of matter over antimatter by a factor of 10^9 . Beyond Standard Model (BSM)

theories with charge-parity and time (CPT) violations have been introduced and fundamental properties can be measured to determine the extent of the CPT violations. One such property is the electron electric dipole moment¹⁵⁻¹⁸ (eEDM). As the value of the eEDM is rather small, no direct measurements have been made to date but upper bounds on the eEDM have been determined. Ideal molecular candidates are polar and possess high internal electric fields¹⁵, as one can measure Stark transitions without the need for a high external electric field. Due to the internal electric field increases with nuclear charge, actinide diatomics made excellent candidates. ThO and ThF⁺ have been proposed as candidates due to internal electric fields^{19, 20} of 78 and 35 GV cm⁻¹, respectively. Typically, ³Δ₁ states are chosen due to their minimal magnetic moments and long lifetimes. The low-lying H³Δ₁ state of ThO has been used to refine the current upper bound²¹ of the eEDM to $|d_e| < 1.1 \times 10^{-29} e \text{ cm}$ and efforts using the ground electronic X³Δ₁ state of ThF⁺ are current underway^{18, 22}.

In this work, the electronic structure of ThO and ThN were characterized employing laser-induced fluorescence (LIF) and dispersed laser-induced fluorescence (DLIF) spectroscopic methods. The following sections will provide the motivation to investigate ThO and ThN, along with previous spectroscopic studies of the chosen molecules.

3.1.2 Previous Studies of ThO

Thorium monoxide (ThO) is one of the most extensively studied actinide species by gas-phase spectroscopy. Electronic transitions have been investigated by employing laser excitation and emission techniques, of which the majority of the data was contributed by Edvinsson and co-workers²³⁻³³. In these works, ThO emission was generated²⁴ by discharging ThI₄ in a microwave discharge. High resolution laser-induced fluorescence spectroscopy has been used to determine the dipole moments and magnetic *g*-factors of the ground X¹Σ⁺ state, as well as selected excited

states, by employing the Stark^{34, 35} and Zeeman^{34, 36} effects, respectively. Two-dimensional LIF has also been employed to determine fluorescence branching ratios³⁷. Microwave spectroscopy³⁸⁻⁴⁰ has been used to observe pure rotational transitions in the ground $X^1\Sigma^+$ state for vibrational levels of $v = 0-15$. As previously mentioned, ThO has been considered as a candidate^{15, 17, 19, 21} for increasing the upper bound of the electron electric dipole moment using the $H^3\Delta_1$ state. The current upper bound²¹ was established by using ThO $C^1\Pi-X^1\Sigma^+$, $C^1\Pi-H^3\Delta_1$, and $I^1\Pi-X^1\Sigma^+$ transitions for state preparation and readout.

The electronic structure of ThO has also been extensively characterized through computational efforts, employing *ab initio*^{41, 42} and ligand field theory⁴³⁻⁴⁵ (LFT) approaches to predict excited state properties. In LFT, actinide complexes are modelled in terms of an ionic atomic metal center whose energies are then perturbed to some degree by the energies of the surrounding ligand(s). This model is justified as the frontier *f* and *d* actinide orbitals are compact and have smaller radii than the actinide-ligand distance⁴⁵, resulting in an electron localization on the actinide metal. For example, in UO, the maximal radial distribution⁶ of the $5f$ orbital is 56 pm while the UO bond distance⁴⁴ in the X^4 ground state is 184 pm. This allows the ligand to essentially be treated as a structureless perturber at the internuclear distance from the actinide metal. As LFT is an ionic model, the electronic states of actinide diatomics can be characterized in terms of the electronic configurations of the metal center and the ligand. For example, in ThO the ground electron $X^1\Sigma^+$ state arises from a $Th^{2+}(7s^2)O^{2-}(2p^6)$ configuration. Excited states can then be characterized in terms of either electron promotion to a higher energy orbital on the metal center or a charge transfer to the ligand. A characteristic of electronic states arising from the same electronic configuration in LFT is that they exhibit similar molecular constants, such as vibrational energy separation and rotational constants. This feature can be quite useful in

assigning electronic configurations to electronic states. LFT can also be used to predict the energies of unobserved electronic states. Recently, a multi-configuration ligand field theory (CI-LFT) model for ThO was developed for assisting in identifying previously unreported states using unassigned data from the Vatican Atlas listings⁴⁶.

The present study of ThO was motivated by three primary concerns, the first being practicality. In investigating a range of ThX species produced by laser ablation and supersonic expansions, it was found that ThO was ever present, despite attempts to suppress oxide production. ThO was even found to be produced in the absence of oxygen-containing gases. While characterizing other ThX molecules, it was found that there were many observed ThO transitions that had not yet been reported. This was unsurprising as the conditions for the LIF measurements in this work were drastically different from Edvinsson's emission^{23-33, 47} experiments. As noted in Chapter 2, in supersonic expansions, different kinds of molecular motion can exhibit different degrees of cooling. Rotational cooling is easily achieved but vibrational as well as electronic cooling is dependent on the separation between energy states. Consequently, these degrees of freedom can exhibit temperatures that are much hotter than the rotational temperature. In Long *et al.*'s work³⁸, laser ablation was coupled with supersonic expansion to produce ThO and microwave spectroscopy was employed to characterize the ground $X^1\Sigma^+$ state. While a cold rotational temperature was observed, vibrational levels up to $v'' = 15$ were significantly populated, corresponding to a vibrational temperature of 2500 K. Since this current work employed laser ablation and supersonic expansion technique, there was a possibility that the newly observed transitions of ThO may have originated from highly excited vibrational states. Prior to the current work, only the $v = 0-3$ vibrational levels of the ground $X^1\Sigma^+$ state have been observed. The observation of new bands in this work allows

characterization of highly excited vibrational levels both in the ground and low-lying excited electronic states. To link back to the first motivation of this work, characterizing these new bands involving excited vibrational states will allow the recognition of these ThO bands when they inevitably complicated the spectra of other ThX diatomics.

The second motivation for this work is also related to the expected presence of highly excited vibrational states. With the observation of excited vibrational states, a potential energy curve of the ground $X^1\Sigma^+$ state can be determined using the Rydberg-Klein-Rees (RKR) method. In the semi-classical RKR method⁴⁸, inner and outer turning points of the potential energy curve are generated by evaluating the vibrational $G(v)$ and rotational energies $B(v)$ as a function of the vibrational quantum number v . Once the turning points are determined, they can then be fit to a realistic potential energy function. Under the assumption that transitions originating from vibrationally excited states of the electronic ground $X^1\Sigma^+$ state will be observed, those vibrational energies can be coupled with microwave rotational constants to produce a potential energy curve for the ground state of ThO using the RKR method. Typically transitions from excited vibrationally states in the electronic ground $X^1\Sigma^+$ state access vibrationally excited levels of upper electronic states. For a majority of previously observed electronic states, only the $v = 0-2$ vibrational levels have been characterized. Observing new ThO transition originating from highly excited vibrational states will allow excited vibrational states of excited electronic states to be characterized for the first time.

The final motivation for investigating ThO bands was to validate the newly developed CI-LFT model by Kaledin *et al.*⁴⁵. While it has been shown that semi-empirical models can yield good agreement with experimental observed electronic states, it has yet to be determined if such models can accurately predict the energies of states not yet observed. In this study, two

electronic states not previously reported were observed and the CI-LFT model was used to determine their identity, providing validation of the predictive capability of the CI-LFT model.

3.1.3 Previous Studies of ThN

The electronic structure of thorium nitride ThN has been investigated using previous studies that employed electronic excitation⁴⁹ and microwave spectroscopy⁵⁰. The first gas phase observations of ThN employed resonantly enhanced multi-photon ionization (REMPI) spectroscopy, which had the capability to mass-resolve ions. As previously mentioned, ThO is ever present in ThX production, even in the absence of oxygen. However, because REMPI has mass-resolution capabilities, the spectroscopy of ThN was able to be performed without interfering ThO bands. A survey spectrum of ThN recorded from 19,700-21,200 cm^{-1} revealed more than 20 vibronic bands and is reproduced in Figure 3.1.

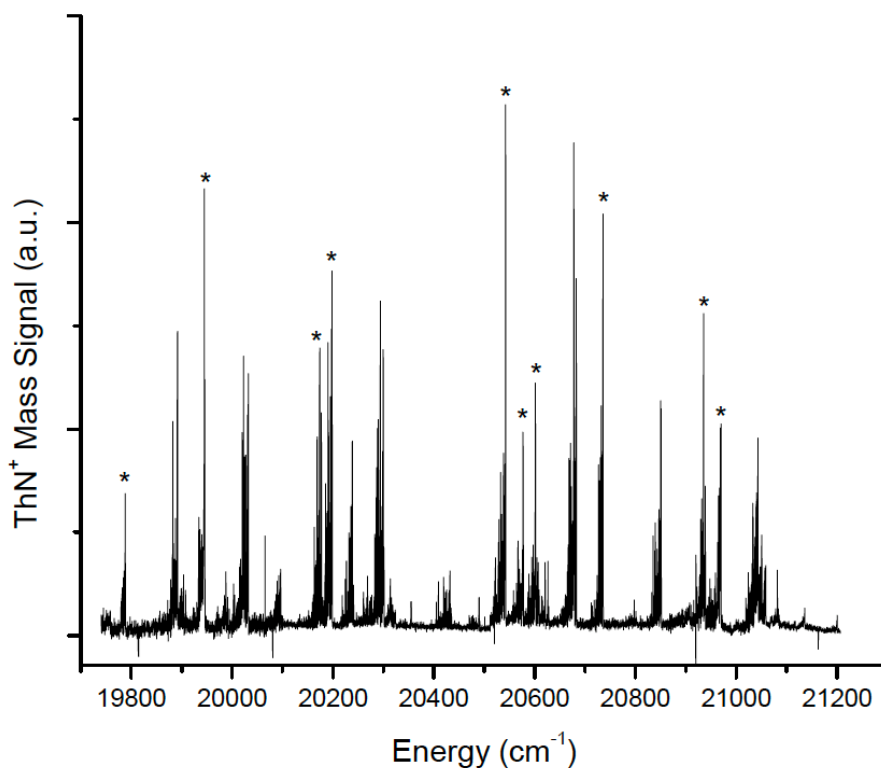


Figure 3.1. ThN survey recorded using REMPI spectroscopy.

Since Heaven *et al.*⁴⁹ produced ThN via laser ablation and supersonic expansion techniques, the ThN bands in Figure 3.1 were rotationally cooled ($T = 40$ K) and it was found that the expansion was vibrationally cooled as well, as almost all the bands originated from the $X^2\Sigma^+ \nu = 0$ state. Rotational resolution of the higher intensity bands indicated the presence of local perturbations of the excited states, while confirming the expected⁵¹ $X^2\Sigma^+$ character of the ground state. This was consistent with the formal $\text{Th}^{3+}(7s)\text{N}^{3-}(2p^6)$ electronic configuration, where the unpaired electron resides in the most non-bonding $7s$ orbital and the only electronic state that could arise from this configuration is a $^2\Sigma^+$ state.

High-resolution spectroscopy has also been performed on ThN, employing laser-induced fluorescence (LIF) and microwave-optical double resonance techniques. Le *et al.*⁵⁰ used the unperturbed $[18.03]1.5-X^2\Sigma^+$ transition to determine electric dipole moments and magnetic g -factors for the ground $X^2\Sigma^+$ by measuring Stark and Zeeman splittings, respectively. The ground $X^2\Sigma^+$ state was found to exhibit a dipole moment of $5.11(9)$ D and the Zeeman splittings were consistent with the g -factor for a free electron ($g = 2.002$). Microwave data yielded rotational constants, spin-rotation terms, ^{14}N hyperfine interaction constants and a zero-point bond length of $r_0 = 1.82222$ Å.

The electronic structure of ThN has also been investigated using *ab initio* methods. Heaven *et al.*⁴⁹ used multi-reference configuration interaction calculations that included spin-orbit coupling (MRSDCI +Q/SO) to assign electronic configurations to electronically excited states. They found that the calculated pattern of energy levels was quite consistent with a ligand field theory (LFT) model. As mentioned before, in a LFT model⁴⁵, electronically excited states can either arise from a promotion of an electron centered on the metal to a higher energy electronic configuration on the metal or they can arise from a charge transfer in which an electron from the

metal is promoted to an orbital on the ligand. In the case of ThN, it was found that electronic states above $10,000 \text{ cm}^{-1}$ arose from either a metal centered $\text{Th}^{3+}(6d)\text{N}^{3-}(2p^6)$ excited electronic configuration or from charge transfer $\text{Th}^{2+}(7s^2)\text{N}^{2-}(2p^5)$ or $\text{Th}^{2+}(7s6d)\text{N}^{2-}(2p^5)$ states. These three configurations, however, lead to a multitude of electronic states, as seen in Table 3.1. The $\text{Th}^{2+}(7s6d)\text{N}^{2-}(2p^5)$ configuration alone gives rise to 25 different electronic states not considering spin orbit separation. This large number of states arising from these electronic configurations may be responsible for the high density of states observed in Figure 3.1.

Table 3.1. States arising from low-energy electronic configurations of ThN.

Electronic Configuration	States
$\text{Th}^{3+}(7s)\text{N}^{3-}(2p^6)$	$X^2\Sigma^+$
$\text{Th}^{3+}(6d)\text{N}^{3-}(2p^6)$	$^2\Sigma^+, ^2\Pi, ^2\Delta$
$\text{Th}^{2+}(7s^2)\text{N}^{2-}(2p^5)$	$^2\Sigma^+, ^2\Pi$
$\text{Th}^{2+}(7s6d)\text{N}^{2-}(2p^5)$	$^2\Sigma^+(\text{x}4), ^4\Sigma^+(\text{x}2), ^2\Sigma^-(\text{x}2),$ $^4\Sigma^-, ^2\Pi(\text{x}6), ^4\Pi(\text{x}2),$ $^2\Delta(\text{x}4), ^4\Delta, ^2\Phi(\text{x}2), ^4\Phi$

As previously mentioned, LFT predicts that electronic states arising from the same electronic configuration possess similar molecular characteristics, e.g. vibrational frequencies and rotational constants. This can be used to facilitate the assignment of electronic states in the high-density spectrum of Figure 3.1 as currently no multi-reference or LFT calculations can provide assignments on the individual bands of Figure 3.1. Groups of states may be able to be identified based on their common molecular properties. While the congestion and erratic behavior of Figure 3.1 prevents upper state vibrational quantum number assignment, it may be possible to derive this information from the intensity distributions of the dispersed laser induced fluorescence (DLIF) spectra. Rotational constants as well as fluorescence decay lifetimes will also be useful in determining configurational assignments.

In the present study, new spectra for many of the bands in Figure 3.1 were recorded using laser-induced fluorescence (LIF), as this method yields better resolution than REMPI in the spectrometer that was used for the first measurements⁴⁹. One limitation of the LIF measurements, however, was that ThN bands that overlapped with strong ThO transitions were not investigated. For the most of the bands, DLIF spectra and fluorescence decay lifetimes were recorded. To facilitate the interpretation of these data, new electronic structure calculations for the excited states of ThN were performed, with the primary objective being to estimate the characteristic molecular constants and to provide data for the low-energy quartet states that were not considered in earlier calculations.

3.2 ThO Results

3.2.1 ThO LIF Spectra and Fitting Results

It should be noted that the time of the ThO data collected, the dispersed fluorescence setup was not yet implemented. Therefore, only LIF data was collected. Low-resolution LIF spectra of ThO were collected from 16,700-21,200 cm^{-1} . Within this range, 55 vibronic bands were of sufficient intensity for investigation using the higher resolution of the etalon-narrowed dye laser. Theoretically fits for rotationally-resolved LIF bands were simulated in PGOPHER⁵². Figure 3.2 shows a rotationally resolved spectrum of the $D^1\Pi-X^1\Sigma^+$ 2-0 transition with a downward-going PGOPHER simulation.

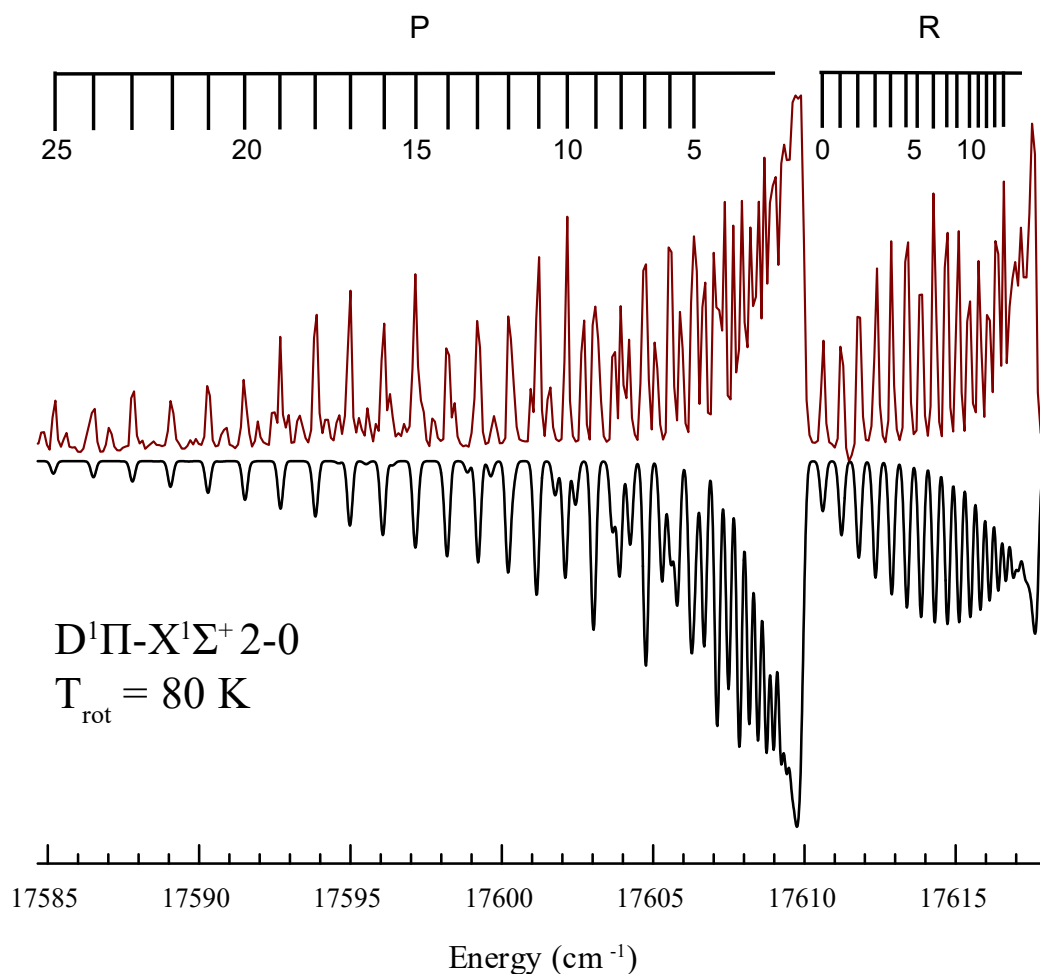


Figure 3.2. Rotationally resolved spectrum of the $D^1\Pi-X^1\Sigma^+$ 2-0 transition with a rotational temperature of 80K.

Many of the observed vibronic transitions involved upper and/or lower levels that have not been previously characterized. In order to characterize these new vibronic levels, the LIF bands were first fit in PGOPHER. The generated simulations gave upper and lower state rotational constants B' and B'' , the band origin ν_0 , and the electronic transition (either $^1\Sigma^- \rightarrow ^1\Sigma$ or $^1\Pi \rightarrow ^1\Sigma$ in terms of Hund's case (a) labels). The band centers were then compared with predicted energies for known electronic transitions. For example, the band center and rotational constants for the $D^1\Pi$ and $X^1\Sigma^+$ states were used to calculate the transitions energies of $\nu'' = 0-10$, $\nu' = 0-10$. These predictions were close enough to provide accurate assignment for previously

unobserved $D^1\Pi$ - $X^1\Sigma^+$ transitions. One issue with the PGOPHER fitting routine is that while the fitting gives accurate values for the difference between the upper and lower rotational constants, the absolute value for the individual constants is known to lower accuracy due to cross correlation. This problem can be remedied if one rotational constant is known with high accuracy. Once all assignments were made, the data was refit with the ground state rotational constants fixed using values from high-resolution microwave spectroscopy³⁸. For transitions that involved two previously uncharacterized states, both the upper state and lower state rotational constants were treated as free parameters.

Of the 55 observed bands, 34 involved vibronic states that had not been previously characterized. Of the 34 bands, 26 were able to be assigned to known electronic transitions and 5 belonged to previously unobserved electronic states. The fitting results for these 31 bands are listed in Table 3.2.

Table 3.2. Band origins and rotational constants for newly observed vibronic states of ThO.

Electronic Transition	$\nu'-\nu''$	ν_0 (cm ⁻¹)	B' (cm ⁻¹)
L'(1)-X ¹ Σ^+	0-4	20769	0.325(1)
	1-5	20711.9	0.318(2)
O'(0 ⁺)-X ¹ Σ^+	2-0	20985.5	0.3212(4)
	0-1	18390.8	0.3253(4)
	0-2	17504.6	0.3252(4)
F(0 ⁺)-X ¹ Σ^+	3-0	20618.4	0.3252(4)
	2-1	19013.3	0.3232(4)
	2-2	18127.3	0.3229(4)
	2-3	17245.2	0.3229(4)
I ¹ Π -X ¹ Σ^+	3-2	20147	0.3251(7)
	4-3	20055.8	0.3258(8)
	3-3	19265.6	0.3253(4)
	4-4	19179.1	0.3245(4)
E ¹ Σ^+ -X ¹ Σ^+	4-1	18700.4	0.3173(4)
	5-2	18620.4	0.3168(4)
	6-3	18540.6	0.3146(4)
	2-0	17965.1	0.3198(4)
	4-2	17814.2	0.3173(4)
	5-3	17739.1	0.3152(4)
	6-4	17663.9	0.3143(4)
	4-3	16932.8	0.3176(4)
	5-4	16862.3	0.3149(4)
D ¹ Π -X ¹ Σ^+	3-1	17543.9	0.3170(4)
	4-2	17477.8	0.3157(4)
	5-3	17411.7	0.3142(4)
	6-4	17345.6	0.3124(4)
	7-5	17279.4	0.3112(4)
	2-1	16719.1	0.3182(4)
	3-2	16657.7	0.3169(4)
C ¹ Π -X ¹ Σ^+	4-1	16894.2	0.3159(5)
	5-2	16820.9	0.3164(5)

Three bands were unable to be assigned. The fitting results for these bands are listed in Table

3.3.

Table 3.3. Molecular constants of unassigned ThO bands.

Transition type	ν_0 (cm ⁻¹)	B' (cm ⁻¹)	B'' (cm ⁻¹)
¹ Π - ¹ Σ	20762.3	0.320(2)	0.324(2)
¹ Π - ¹ Σ	19754.0	0.32	0.332
¹ Σ - ¹ Σ	18944.5	0.323	0.331

Band origins of known states were combined with previous studies to improved values for the vibrational constants for these known states. These results are listed in Table 3.4. For the fit for the ¹Π state, the $\nu = 4$ level was not included as it appeared to be perturbed.

Table 3.4. Vibrational constants for ThO.

Electronic State	ω_e (cm ⁻¹)	$\omega_e x_e$ (cm ⁻¹)
X ¹ Σ ⁺	895.72(21)	2.388(39)
C ¹ Π	834.65(30)	2.176(6)
D ¹ Π	839.08(11)	2.383(13)
E ¹ Σ ⁺	829.28(10)	2.309(4)
I ¹ Π	800.70(11)	1.44(1)

3.2.2 X¹Σ⁺ Ground State Potential Energy Curve Generation

Ground states of diatomic molecules are typically minimally perturbed and therefore analysis of the ground state reveals the unperturbed character of the molecule and is a good place to begin. Combination differences from the D¹Π- X¹Σ⁺ and E¹Σ⁺-X¹Σ⁺ transitions were used to define the $\nu'' = 0-4$ levels for the X¹Σ⁺ state. While the D¹Π- X¹Σ⁺ 7-5 transition was observed, there was no other transition observed from the $\nu'' = 5$ state that could be used to determine the energy of $\nu'' = 5$. The energies of the $\nu'' = 0-2$ states were taken from Edvinsson *et al*²⁴. The vibrational energies of the X¹Σ⁺ state were fit to determine vibrational constants ω_e and $\omega_e x_e$. Including $\omega_e y_e$ in the vibrational fits did not improve the fits and it was found that the value obtained was statistically insignificant. The vibrational constants in Table 3 along with the

rotational constants from Long³⁸ were used to generate a pointwise RKR potential energy curve of the $X^1\Sigma^+$. The resulting rotational constants, vibrational energies, vibrational intervals, and turning points are listed in Table 3.5.

Table 3.5. RKR potential energy curve data for the ThO ground $X^1\Sigma^+$ state.

v	B_v (cm ⁻¹)	$G(v)$ cm ⁻¹	$\Delta G_{v+1/2}$ (cm ⁻¹)	R_{min} (cm ⁻¹)	R_{max} (cm ⁻¹)
0	0.33204	447.28	890.92	1.7919	1.8923
1	0.330737	1338.21	886.17	1.7587	1.933
2	0.329434	2224.37	881.41	1.7369	1.9625
3	0.32813	3105.79	876.66	1.7198	1.9873
4	0.031211	3982.44	871.9	1.7054	2.0093
5	0.325522	4854.34	867.14	1.6928	2.0296
6	0.324218	5721.48	862.39	1.6816	2.0486
7	0.322914	6583.87	857.63	1.6714	2.0666
8	0.321609	7441.5	852.87	1.6621	2.0837
9	0.320304	8294.37	848.12	1.6535	2.1002
10	0.318998	9142.49	843.36	1.6454	2.1162
11	0.317692	9985.85	838.61	1.6379	2.1317
12	0.316386	10824.46	833.85	1.6308	2.1468
13	0.31508	11658.31	829.09	1.624	2.1616
14	0.313773	12487.4	824.34	1.6176	2.1761
15	0.312466	13311.74	819.58	1.6116	2.1903

To generate a continuous potential energy curve, the RKR turning points were fit to an Expanded Morse Oscillator (EMO) function using LeRoy's program betaFIT⁵³, using the specific EMO model

$$V(r) = D_e(1 - \text{Exp}(-\beta(R)(R - R_e)))^2 \quad (3.1)$$

where D_e is the dissociation energy and R_e is the equilibrium bond length. The Morse parameter $\beta(R)$ can be expanded as a radially dependent polynomial in $\gamma_p^{R_e}(R)$

$$\beta(R) = \sum_{i=0}^N \beta_i \gamma_p^{R_e}(R)^i \quad (3.2)$$

where

$$\gamma_p^{R_e}(R) = \frac{R^p - R_e^p}{R^p + R_e^p} \quad (3.3)$$

The number of terms included in the polynomial is $N + 1$. Per LeRoy's recommendations, the value of p was set to 3 and D_e was fixed to the value obtained from fitting the data to a standard Morse potential where $N = 0$ and $D_e = 80,500 \text{ cm}^{-1}$. The data was fit to values of $N = 0, 1, 2, 3$ and the corresponding deviations were 10.6, 7.3, 2.7, and 0.24. For fits with $N > 3$, improvements in the fit were minimal and resulted in questionable statistical significance. Using the Level 8.0 program⁵⁴, rotational and vibrational energies were recovered from the $N = 3$ fit and were in good agreement with the experimental input data. The EMO parameters are listed in Table 5 along with their standard deviations which were optimized by betaFIT. As the value of D_e was fixed, no standard deviation is listed for it in Table 3.6.

Table 3.6. Expanded morse oscillator potential energy parameters for the ground $X^1\Sigma^+$ state of ThO.

Parameter	Value
D_e	80,500 ^a
R_e	1.8420327(23)
β_0	1.4871657(210)
β_1	$-1.090(19) \times 10^{-2}$
β_2	$8.702(45) \times 10^{-2}$
β_3	$5.08(31) \times 10^{-2}$

Figure 3.3 shows the computed $X^1\Sigma^+$ potential energy curve fitted to the RKR points.

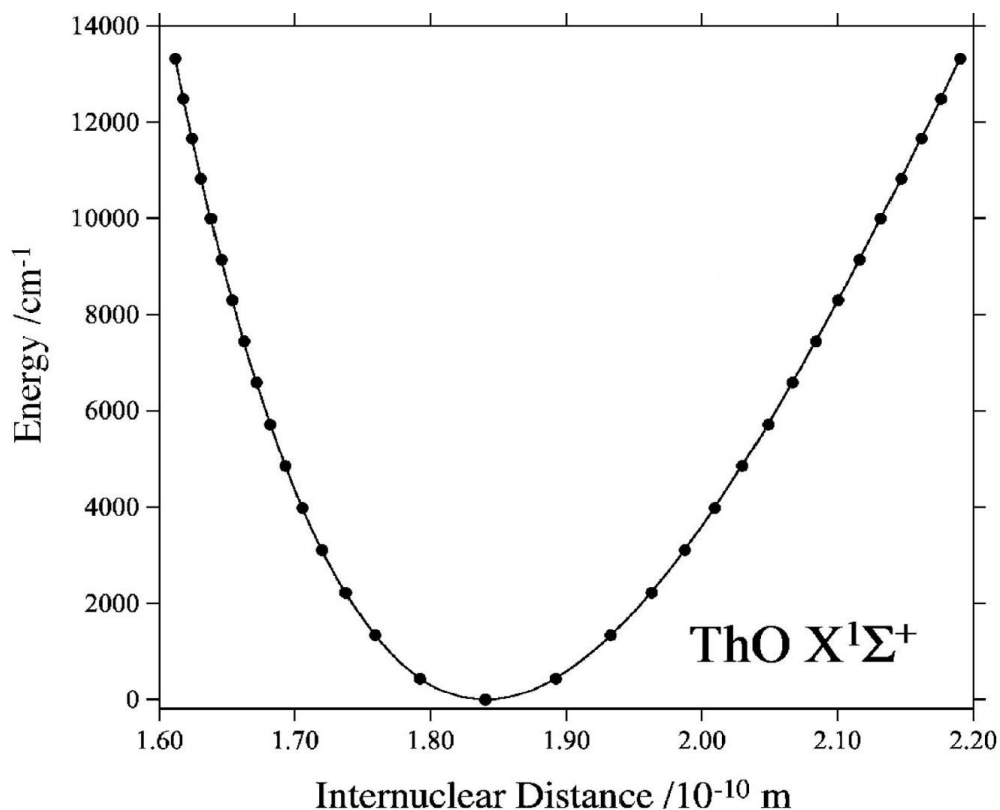


Figure 3.3. RKR potential energy curve for the ground $X^1\Sigma^+$ state of ThO.

3.3 ThO Discussion

3.3.1 Vibrational Extension of the $C^1\Pi$, $D^1\Pi$, $E^1\Sigma^+$, $I^1\Pi$, and $F^1\Pi$ Electronic States

The range of the upper vibrational states for the $C^1\Pi$ - $X^1\Sigma^+$, $D^1\Pi$ - $X^1\Sigma^+$, and $E^1\Sigma^+$ - $X^1\Sigma^+$ transitions was extended, adding $\nu' = 4,5$ for the $C^1\Pi$ state, $\nu' = 4-6$ for the $E^1\Sigma^+$ state, and $\nu' = 2-7$ for the $D^1\Pi$ state. These results and previously determined energies for lower vibrational levels^{24,26} were fit to determine new vibrational constants for the above electronic states and are given in Table 3. The vibrational manifold for the three electronic states appeared to be free of perturbations at the level of accuracy of the band origins ($\pm 0.11 \text{ cm}^{-1}$).

Previously only the $I^1\Pi \nu' = 0,1$ states were observed²⁴ from $I^1\Pi$ - $X^1\Sigma^+$ 0-0 and 1-1 transitions. This work expands the $I^1\Pi$ state to the $\nu' = 2-4$ levels via the $I^1\Pi$ - $X^1\Sigma^+$ 2-2, 3-3, 4-4, 4-3, 3-2, and 2-1 bands. Using the ground state vibrational intervals from the $D^1\Pi$ - $X^1\Sigma^+$, and

$E^1\Sigma^+ - X^1\Sigma^+$ transitions, the excited state vibrational intervals of the $I^1\Pi$ state were calculated. For $\nu' = 0-3$, the $I^1\Pi$ intervals were consistent with the simple Morse expression

$$\Delta G_{\nu+1/2} = \omega_e - 2\omega_e x_e(\nu + 1) \quad (3.4)$$

The 4-3 interval, however, was 1.9 cm^{-1} lower than the extrapolated value, indicating the presence of a local perturbation.

Edvinsson *et al.*²⁴ previously reported the $F^1\Sigma^+ - X^1\Sigma^+$ 0-0 and 1-1 transitions, tentatively assigning these bands to a common electronic transition due to a small excited state vibrational interval implied by the 1-1 assignment. This work expands the characterization of the $F^1\Sigma^+$ state to the $\nu' = 2,3$ levels through the 3-0, 2-1, 2-2, and 2-3 $F^1\Sigma^+ - X^1\Sigma^+$ transitions. Using the band centers for these transitions, along with this work's band centers for the 1-0 and 1-2 transitions and Edvinsson's 0-0 and 1-1 values, the vibrational intervals in the $F^1\Sigma^+$ state can be determined. Figure 3.4 shows an energy diagram of the $F^1\Sigma^+$ and $X^1\Sigma^+$ $\nu = 0-3$ states with experimental transition energies.

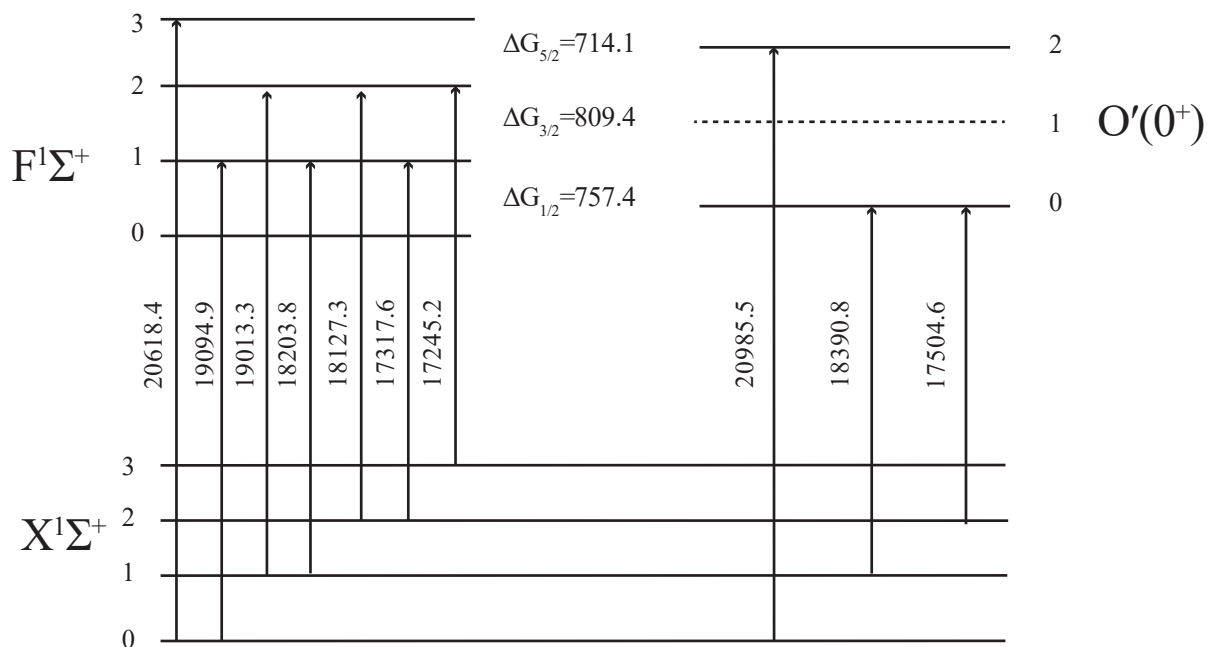


Figure 3.4. Energy diagram of selected $F^1\Sigma^+$ - $X^1\Sigma^+$ and $O'(0^+)$ - $X^1\Sigma^+$ vibronic transitions with vibrational intervals for the $F^1\Sigma^+$. All energy values are in cm^{-1} and the schematic is not to scale. It can be seen from the values for the $F^1\Sigma^+$ vibrational intervals that $\Delta G_{3/2}$ is considerably larger than both $\Delta G_{1/2}$ and $\Delta G_{5/2}$. If it is assumed that the $v' = 2$ level is strongly perturbed by roughly 48 cm^{-1} , the average vibrational interval in the $F^1\Sigma^+$ state is 760 cm^{-1} .

3.3.2 Characterization of New $O'(0^+)$ and $L'(1)$ Electronic States

In the same energy range as the $F^1\Sigma^+$ - $X^1\Sigma^+$ transitions, transitions to two vibronic levels that do not belong to any known electronic states were observed. These vibronic levels have $\Omega = 0^+$ symmetry and are tentatively labeled as $O'(0^+)$ $v' = 0$ and 2 in Table 3.2 and the energies are shown in Figure 3.4. This assignment was made as Kaledin's CI-LFT model⁴⁵ predicts a value of 18922 cm^{-1} for the $O'(0^+)$ $v' = 0$ state which is consistent with the experimental value of 19281 cm^{-1} . Another confirmation of this assignment comes from the Vatican Atlas⁴⁶, which lists the $O'(0^+)$ $v' = 0$ state at 19271 cm^{-1} . Assignment of the transition at 20985.5 cm^{-1} as the $O'(0^+)$ - $X^1\Sigma^+$

2-0 transition gives an approximate $O'(0^+)$ ω_e value of 852 cm^{-1} but as no bands were observed originating from $O'(0^+) v' = 1$, this is a tentative assignment.

Two transitions within the energy range of $20700\text{-}20770\text{ cm}^{-1}$ that could not be assigned to known electronic states were observed. The rotational structures of these bands were consistent with $(\Omega'=1)\text{-}X^1\Sigma^+$ transitions and the fitted B'' values suggested they originated from high vibrational levels of the $X^1\Sigma^+$ state. Using CI-LFT⁴⁵ predictions, the 20769.0 cm^{-1} band was assigned as the $L'(1)\text{-}X^1\Sigma^+$ 0-4 transition. This would give a value of 24304.2 cm^{-1} for $L'(1) v' = 0$ which reasonably agrees with the CI-LFT value of 23008 cm^{-1} and the value derived from the Vatican Atlas data of 24325 cm^{-1} . Two bands nearby in energy are good candidates for the 1-5 transition and assignment of the lower of the two at 20711.9 cm^{-1} gives a $L'(1)$ vibrational interval of $\Delta G_{1/2} = 814.8\text{ cm}^{-1}$. This value is typical of unperturbed excited states in this energy range and therefore gives good confirmation that the $207119.\text{cm}^{-1}$ band is indeed the $L'(1)\text{-}X^1\Sigma^+$ 1-5 transition.

Some of the listed spectra originate from the $X^1\Sigma^+ v'' = 5$ level which lies 44070.0 cm^{-1} above the $v'' = 0$ state. As the first electronically excited state $H^3\Delta_1$ has an energy of 5316.6 cm^{-1} , it was considered that the unassigned transitions in Table 3.3 may have originated from the $H^3\Delta_1$ state. However, scans over the regions where the $P^3\Pi_0\text{-}H^3\Delta_1$ and $O^3\Pi_0\text{-}H^3\Delta_1$ 0-0 bands should be located revealed such bands. It is therefore concluded that the population in the $H^3\Delta_1$ was too low for detection.

3.4 ThN Results

3.4.1 ThN Experimental Results

Rotationally resolved laser-induced fluorescence (LIF) spectra were recorded for 11 bands from $19655\text{-}21200\text{ cm}^{-1}$. Figure 3.1 shows 10 of these bands that were previously

observed⁴⁹ using resonantly enhanced two-photon ionization (REMPI) spectroscopy. The LIF band at 19,655 cm⁻¹ is not shown in Figure 3.1 as it is out of the spectral range. Figure 2 shows the rotational structure of a band center near 20,605 cm⁻¹ with a rotational temperature of 90K. Typically, ThN spectra exhibit rotational temperatures ranging from 40 to 90 K.

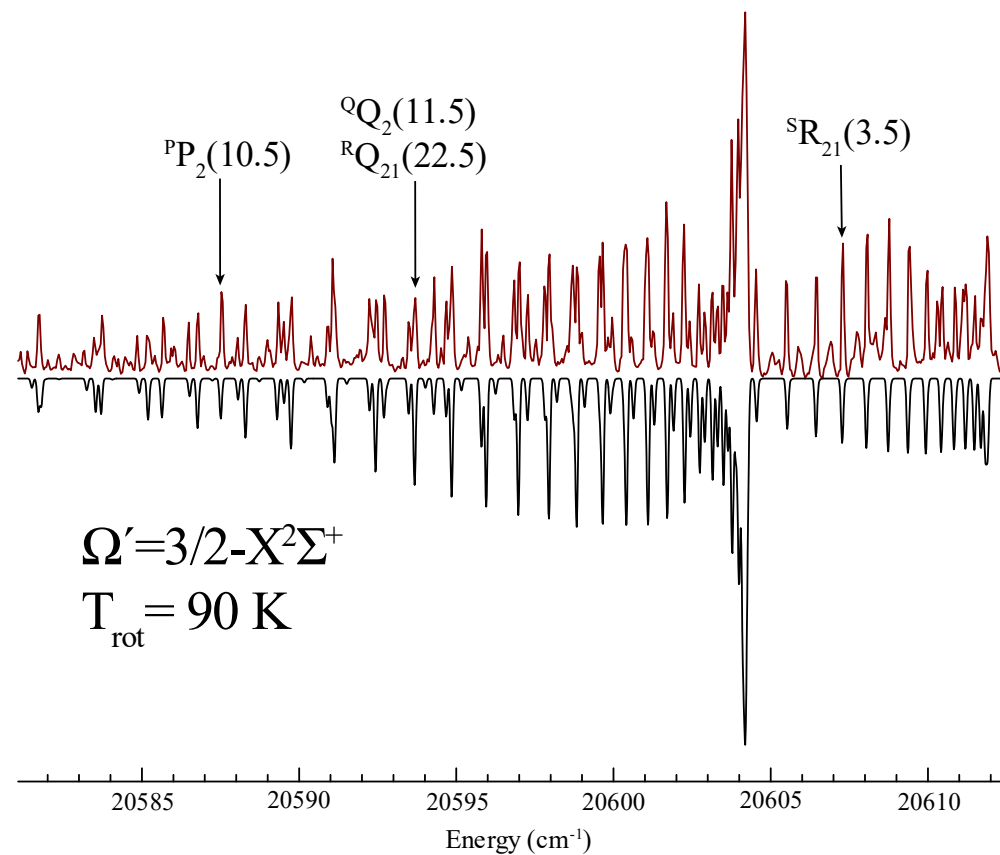


Figure 3.5. Rotational spectrum of $\Omega' = 3/2 - X^2\Sigma^+$ band centered at 20605 cm⁻¹. The downward trace is a theoretical fit assuming a rotational temperature of 90 K.

In Figure 3.5, the downward trace is a theoretical simulation generated by PGOPHER⁵². The rotational energies were determined by

$$F''_1(J'') = B''_0 \left(J'' - \frac{1}{2} \right) \left(J'' + \frac{1}{2} \right) - D''_0 \left[\left(J'' - \frac{1}{2} \right) \left(J'' + \frac{1}{2} \right) \right]^2 + \frac{1}{2} \gamma'' \left(J'' - \frac{1}{2} \right) \quad (3.5)$$

and

$$F''_2(J'') = B''_0 \left(J'' + \frac{1}{2} \right) \left(J'' + \frac{3}{2} \right) - D''_0 \left[\left(J'' + \frac{1}{2} \right) \left(J'' + \frac{3}{2} \right) \right]^2 - \frac{1}{2} \gamma'' \left(J'' - \frac{3}{2} \right) \quad (3.6)$$

where B_0'' , D_0'' , and γ'' are the rotational, centrifugal distortion, and spin-rotational constants of the ground $X^2\Sigma^+ v'' = 0$ state. In the fitting process, the ground state constants were fixed using the values from Le *et al.*⁵⁰ and these values are reproduced in Table 1.

Table 3.7. Ground ThN $X^2\Sigma^+ v'' = 0$ state rotational constants reproduced from Le *et al.*⁵⁰

Constant	Value (cm ⁻¹)
B_0''	0.3846
D_0''	2.47×10^{-7}
γ''	0.016399

The upper state was treated as a Hund's case (c) with $\Omega' = 3/2$. This was implemented in PGOPHER by setting the upper state term symbol to $^2\Pi$ and selecting the Ω -component. Only the upper state vibronic term energy (T'_0) and the rotational constant (B') were able to be determined due to the low-resolution of the spectrum. Using these variables and the above method to constraint for Hund's case (c), the effective energy expressions for the upper state energies were

$$E'_{3/2}(J') = T'_0 + B' \left(\left(J' + \frac{1}{2} \right)^2 - 1 \right) \quad (3.7)$$

and

$$E'_{1/2}(J') = T'_0 + B' \left(\left(J' + \frac{1}{2} \right)^2 + 1 \right) \quad (3.8)$$

for $\Omega' = 3/2$ and $1/2$, respectively.

Eight bands were found to be relatively unperturbed, yielding acceptable fits to the given energy expressions assuming that they originated from the ground state zero-point level. The constants from these fits are listed in Table 3.8, along with the constants from the [18.00]3/2- $X^2\Sigma^+$ band that was report by Le *et al.*⁵⁰. Note that the definition of T'_0 in this work differs by that

of Le by an offset of B' i.e., T_0' (this work) = T_0' (Le) - B' . Table 2 also lists the average residuals of the fits as well as the lifetime of the molecular upper states. It should be noted that the bands centered at 19,950 and 20,970 cm^{-1} were consistent with ${}^2\Sigma^+$ upper states with energy levels represented by Equations (1) and (2). The data for the [20.94]3/2 band was taken from Heaven *et al.*⁴⁹.

Table 3.8. Excited state molecular constants determined from unperturbed bands of ThN.

$[T_0/1000 \text{ cm}^{-1}]\Omega'$	$\nu_0 \text{ (cm}^{-1}\text{)}$	$B' \text{ (cm}^{-1}\text{)}$	$\gamma' \text{ (cm}^{-1}\text{)}$	Avg Res (cm^{-1})	$\tau \text{ (ns)}$
[18.00]3/2	18005.0720	0.352274	---	0.0004	---
[19.79]1/2	19789.2(1)	0.3224(5)	---	0.13	---
[19.95] ${}^2\Sigma^+$	19946.0(1)	0.3352(5)	0.137(1)	0.05	281(4)
[20.18]3/2	20176.1(1)	0.3208(5)	---	0.09	462(7)
[20.58]3/2	20576.3(1)	0.3454(7)	---	0.10	317(3)
[20.60]3/2	20603.5(1)	0.3487(5)	---	0.04	220(3)
[20.74]1/2	20735.9(1)	0.322(2)	---	0.11	---
[20.94]3/2	20937.2(1)	0.3190(5)	---	0.02	422(4)
[20.97] ${}^2\Sigma^+$	20969.1(1)	0.3328(5)	0.172(2)	0.06	743(2)

Three bands were observed that displayed local perturbations and were also modeled in PGOPHER. Two of the bands were treated as Hund's case (c) ${}^2\Pi_{1/2}$ states and the third was modeled as a ${}^4\Sigma^+$ state. The perturbed states could be accurately modeled under the assumption that the perturbing interactions were of kind ${}^2\Pi_{1/2} \leftrightarrow {}^2\Sigma^-$ (mediated by the $\hat{J}^\pm \hat{L}^\mp$ operators) and ${}^4\Sigma^+ \leftrightarrow {}^4\Sigma^+$ (mediated by the $\hat{J}^\pm \hat{S}^\mp$ operators). Figure 3.6 shows the perturbed band at 20196.6 cm^{-1} with a best fit simulation modeling a ${}^2\Pi_{1/2} \leftrightarrow {}^2\Sigma^-$ perturbation interaction.

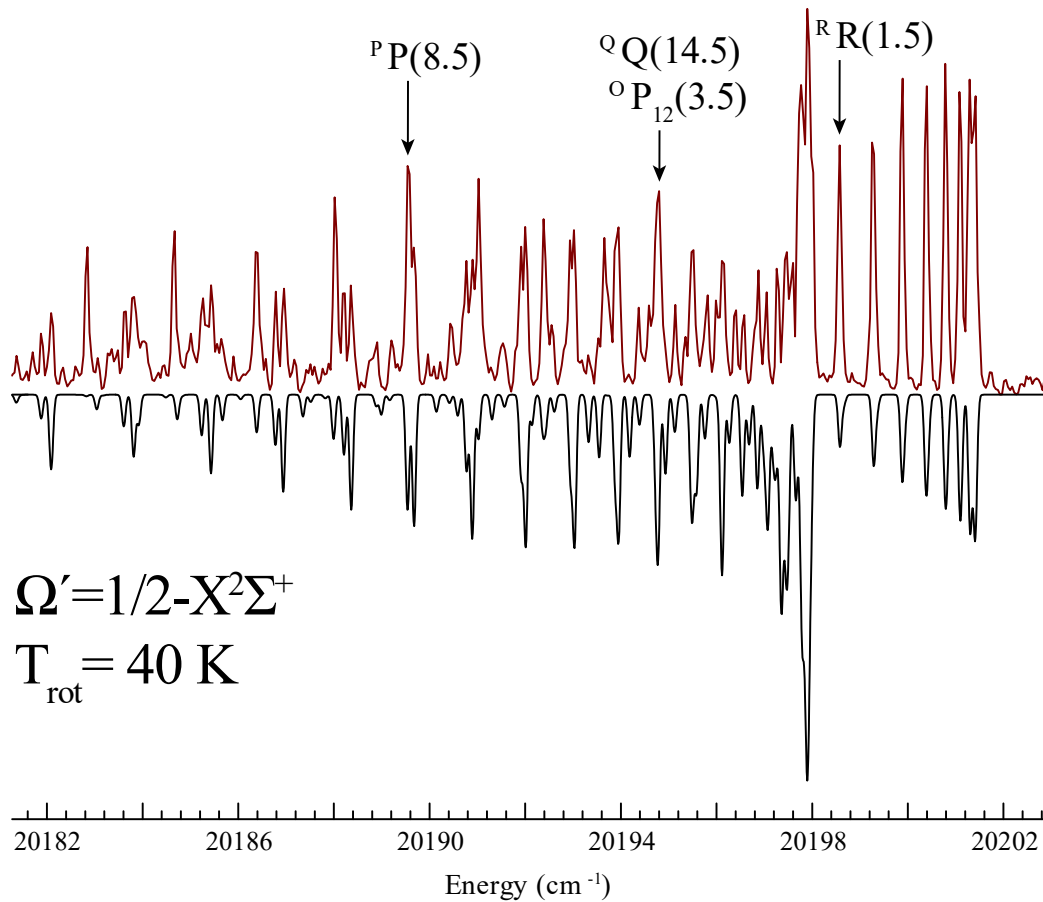


Figure 3.6. Rotational structure of the perturbed $\Omega' = 1/2 - X^2 \Sigma^+$ band centered at 20197 cm^{-1} . The downward trace is a fit assuming a rotational temperature of 40 K.

Table 3.9 lists the molecular constants derived from fitting the three perturbed bands.

Table 3.9. Excited state molecular constants derived from the three observed perturbed bands of ThN.

Parameter	$\Omega'=1/2$	$\Omega'=1/2$	$\Omega'=3/2$
T_0' (cm ⁻¹)	19655.1(1)	20196.6(1)	20542.1(1)
B_0' (cm ⁻¹)	0.34368	0.3349(1)	0.3492
γ' (cm ⁻¹)	-0.062	---	0.059
λ_{ss} (cm ⁻¹)	---	---	-0.074
τ (ns)	289(2)	310(10)	265(11)
Perturbing State	$^2\Sigma^-$	$^2\Sigma^-$	$^4\Sigma^+$
$\nu_{0,p}$ (cm ⁻¹)	19732.5	20197.7(1)	20550.1
B'_p (cm ⁻¹)	0.34	0.379(2)	0.33
Coupling term	$\hat{f}^\pm \hat{L}^\mp$	$\hat{f}^\pm \hat{L}^\mp$	$\hat{f}^\pm \hat{S}^\mp$
Coupling coefficient	0.05	0.05	0.02

Fluorescence decay curves were recorded for most of the excited states reported here. The decay curves were taken by parking the dye laser on the most intense feature of the band, typically the Q or R bandhead. The observed curves exhibiting single exponential behavior and the fitted decay lifetimes are listed in Tables 3.8 and 3.9.

Dispersed fluorescence spectra were recorded using excitation of nine of the rotationally resolved bands and two other vibronic transitions at 20679 cm⁻¹ and 21055 cm⁻¹ that were only studied at low resolution. The DLIF spectra were obtained up to 860 nm, limited by the response of the PMT. Based on the electronic structure calculations of Heaven *et al.*⁴⁹, it was expected that only transitions down to the ground state would be observed due to Ω selection rules. Figure 3.7 shows a composite DLIF spectrum relative to the energy of the ground $X^2\Sigma^+ \nu'' = 0$ state.

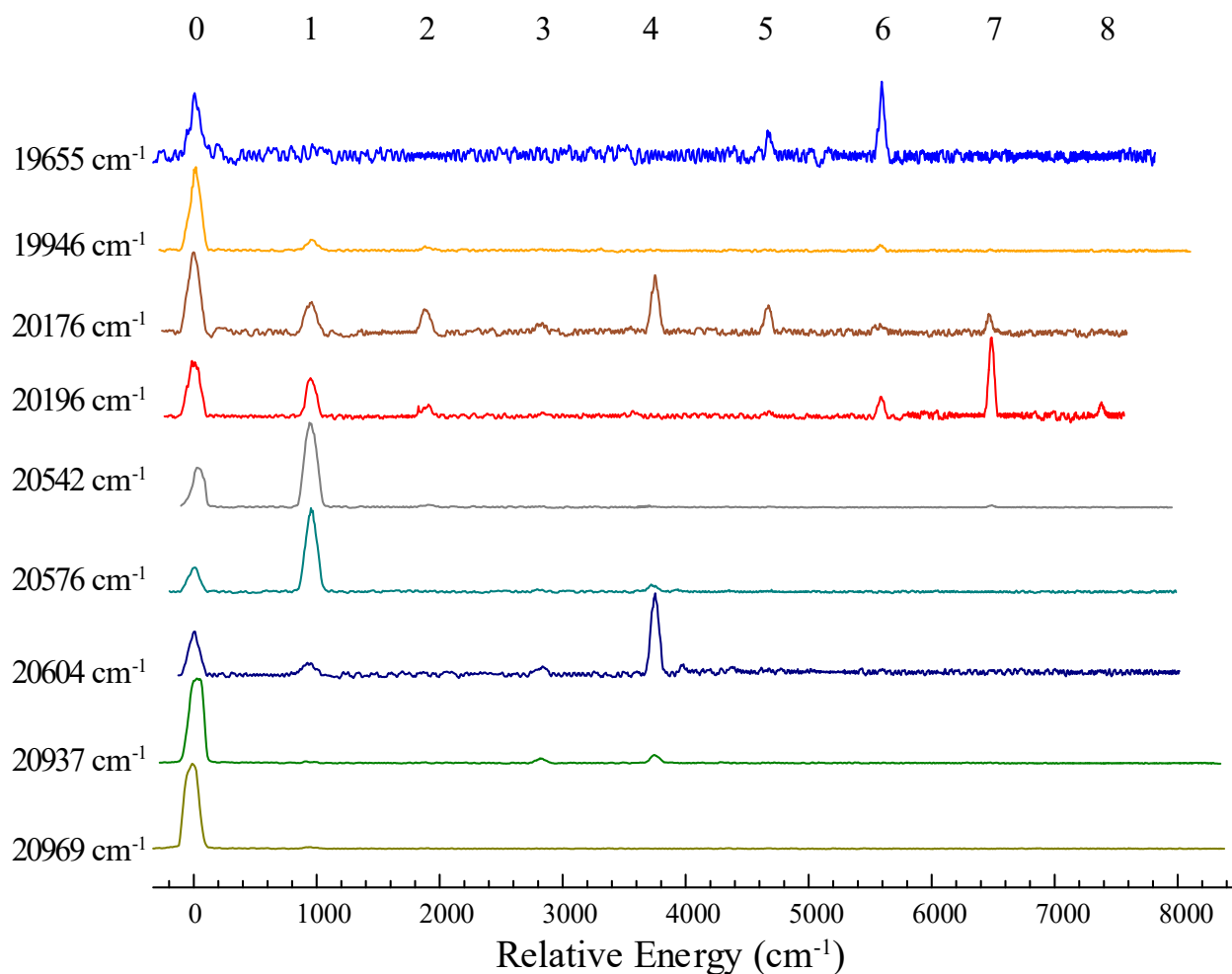


Figure 3.7. DLIF spectra for the observed ThN bands. The excitation photon energies are listed to the left-hand column and the ground state vibrational levels are listed across the top of the figure.

The DLIF spectra reveal simple vibrational progressions in the ground electronic state.

Previously, only the $v'' = 0, 1$ levels had been observed using DLIF measurements, so the only vibrational interval determined was $\Delta G''_{1/2}$. Figure 3.7 shows vibrational progressions up to $v'' = 8$, with vibrational energies that are well defined by the simple Morse expression in Equation 3.4. Fitting the vibrational energies to Equation 3.4 yielded values of $\omega_e = 962(4)$ and $\omega_e x_e = 4.43(42)$ cm^{-1} .

3.4.2 Electronic Structure Calculations

Previously, electronic structure calculations only considered the lowest energy doublet states⁴⁹ so efforts were taken in this work to calculate a greater number of excited states as well as low-lying quartet states. All calculations done in this work were executed with the Molpro2015.1 suite of programs^{55, 56} Calculations began with the restricted Hartree-Fock model to generate starting orbitals, which was then followed by state-averaged complete active space self-consistent field (SA-CASSCF) calculations. Dynamical weighting was then implemented using DYNW=2. Then configuration interaction (CI) was implemented using the multi-reference single and double excitation CI method including Davidson correction (MRSDCI+Q). Finally, the spin-orbit interaction was considered by diagonalizing the matrix of the Breit-Pauli operator constructed in the SA-CASSCF eigenbasis. In this procedure, the spin-free energies of the MRSDCI + Q calculations were used in the diagonal matrix elements.

The effective core potential basis set^{57, 58} ECP60MWB_ANO was used for Th, excluding *g*-orbitals. For N, the aug-cc-pVTZ basis set⁵⁹ was used. In Molpro, orbitals were symmetry adapted using the C_{2v} point group which is the highest symmetry available for a heteronuclear diatomic. The active space consisted of eight molecular orbitals ($3a_1 \oplus 2b_1 \oplus 2b_2 \oplus a_2$) constructed from the Th $7s$ and $6d$ and N $2s$ and $2p$ orbitals. The calculations included 14 spin-free doublet states ($5a_1 \oplus 3b_1 \oplus 3b_2 \oplus 3a_2$) and 16 spin-free quarter sets ($4a_1 \oplus 4b_1 \oplus 4b_2 \oplus 4a_2$). The validity of the SA-CASSCF calculations was confirmed through the \hat{L}_z^2 expectation values. Spin-orbit mixing between the doublet and quarter states was excluded by performing the doublet and quarter calculations separately.

Potential energy curves for the doublet and quarter states were then constructed by calculating single-point energies for a range of internuclear distances of 1.62-2.22 Å in steps of

0.04 Å. Figures 3.8 and 3.9 show the potential energy curves for the calculated doublet and quarter states, respectively.

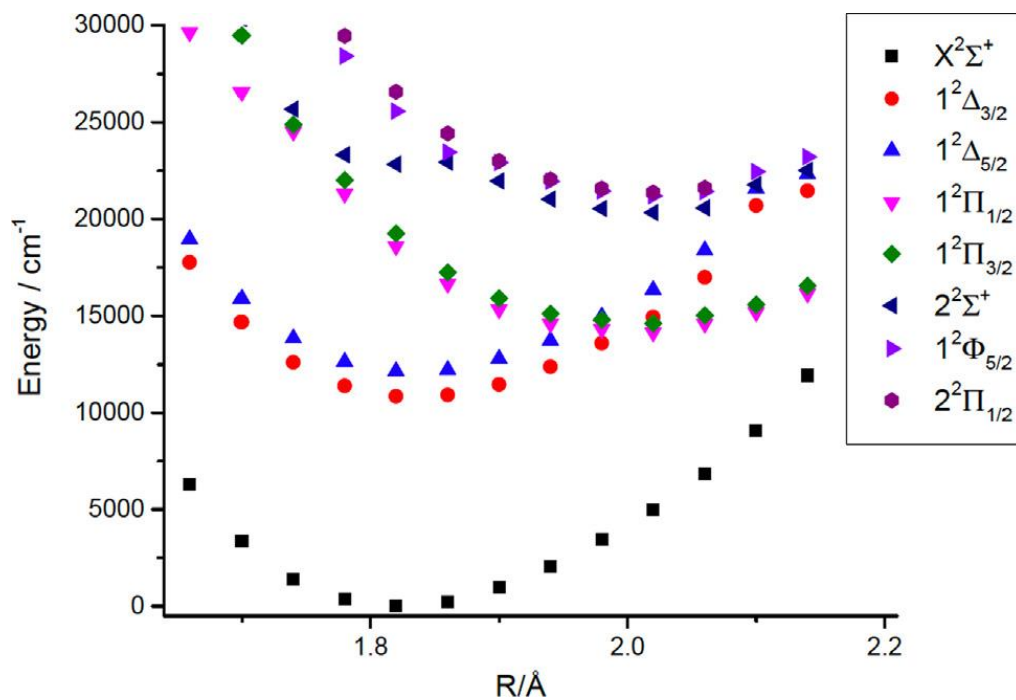


Figure 3.8. Calculated potential energy curves for the low-energy doublet states of ThN.

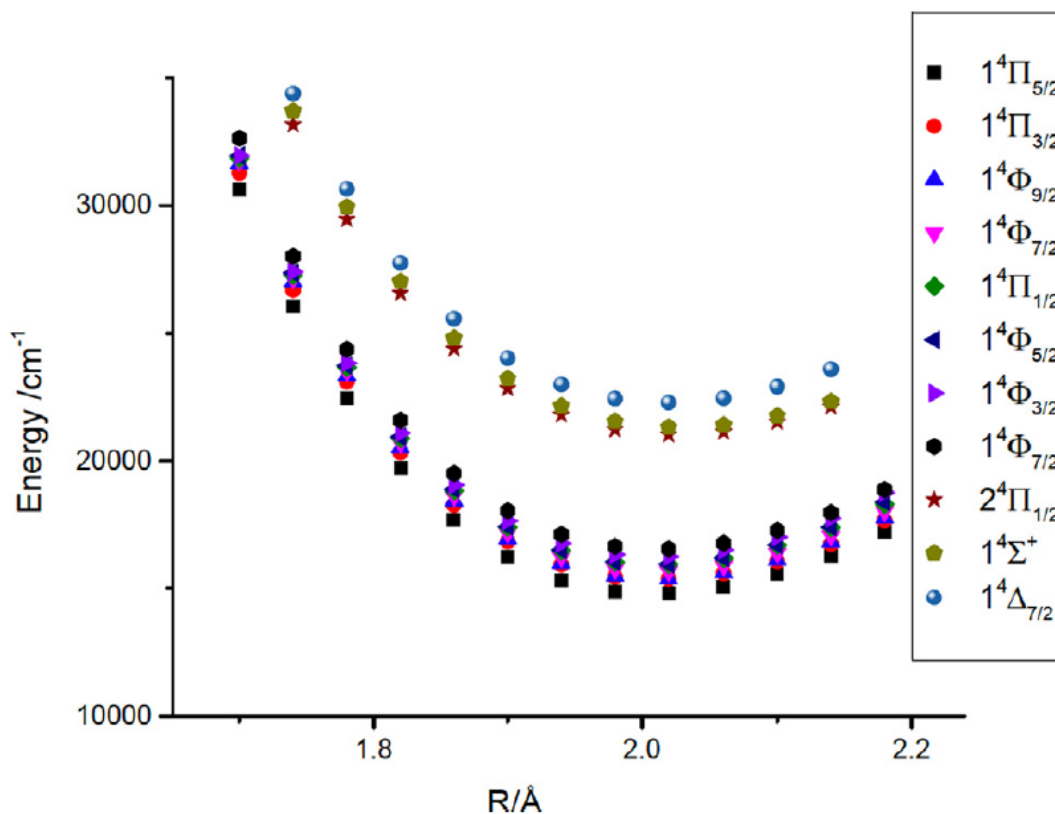


Figure 3.9. Calculated potential energy curves for the low-energy quartet states of ThN.

Molecular constants were determined by fitting Morse potential energy functions to the curves.

The resulting constants are listed in Table 3.10. In the state notation in Table 4, the index before the Hund's case (a) $^{2\Sigma+1}\Lambda_{\Omega} n$ label refers to n th state with that label.

Table 3.10. Molecular constants for the doublet and quarter states of ThN up to 17,000 cm^{-1} .

State	T_e (cm^{-1})	ω_e (cm^{-1})	$\omega_e x_e$ (cm^{-1})	r_e (\AA)	B_e (cm^{-1})
$X^2\Sigma^+$	0	956	3.8	1.82	0.385
$1^2\Delta_{3/2}$	10,815	925	3.6	1.84	0.379
$1^2\Delta_{5/2}$	12,110	929	3.6	1.83	0.380
$1^2\Pi_{1/2}$	14,194	742	2.7	2.00	0.320
$1^2\Pi_{3/2}$	14,669	738	2.8	2.00	0.320
$1^4\Pi_{1/2}$	14,788	730	2.7	2.01	0.317
$1^4\Phi_{3/2}$	16,537	728	2.8	2.01	0.317

From Figure 3.8, it can be seen that the pattern of low-energy doublet states is consistent with LFT expectations, as was first noted by Heaven *et al.*⁴⁹. The first three states $X^2\Sigma^+$, $1^2\Delta_{3/2}$, and $1^2\Delta_{5/2}$ are consistent with a $\text{Th}^{3+}\text{N}^{3-}$ configuration near the equilibrium bond length r_e . It can be seen from Figure 3.8 and Table 3.10 and that these three states exhibit the short equilibrium bond lengths and highest vibrational frequencies ω_e . For the next group of doublet states, the equilibrium bond lengths increase to approximately 2 Å and the vibrational frequencies decrease to around 740 cm^{-1} . The change in vibrational frequency is characteristic of electronic states arising from a different electronic configuration. These doublet states arise from a $\text{Th}^{2+}\text{N}^{2+}$ configuration, with the lowest energy states $1^2\Pi_{1/2}$ and $1^2\Pi_{3/2}$ states arising from a $\text{Th}^{2+}(7s^2)\text{N}^{2-}(2p^5)$ configuration. As the energy of ThN is increased, they are several similar potential energy curves that arise from a $\text{Th}^{2+}(7s6d)\text{N}^{2-}(2p^5)$ configuration. Table 3.8 gives the energy of the electronic states at an internuclear distance equal to the equilibrium bond length for the $^2\Sigma^+$ state ($r = 1.82$ Å). The states are denoted by a Hund's case (a) $^{2\Sigma+1}\Lambda_\Omega$ label that report the basis functions that make the leading contributions. Due to many state interactions, the basis function contributions significantly change with increase internuclear distance over the examined range.

Table 3.11. Calculated doublet energy levels of ThN at an internuclear distance of $r = 1.82 \text{ \AA}$.

Electronic Configuration	State	Energy (cm ⁻¹)
Th ³⁺ (7s)N ³⁻ (2p ⁶)	X 1 ² Σ ⁺	0
Th ³⁺ (6d)N ³⁻ (2p ⁶)	1 ² Δ _{3/2}	10,855
	1 ² Δ _{5/2}	12,141
	2 ² Σ ⁺	22,832
Th ²⁺ (7s ²)N ²⁻ (2p ⁵)	1 ² Π _{3/2}	18,603
	1 ² Π _{1/2}	19,258
Th ²⁺ (7s6d)N ²⁻ (2p ⁵)	1 ² Φ _{5/2}	25,571
	2 ² Π _{1/2}	26,575
	1 ² Φ _{7/2}	26,621
	2 ² Π _{3/2}	27,303

It can be seen from Figures 3.8 and 3.9, that the lowest energy quartet states have similar potential energy curves to those of the 1²Π_{1/2} and 1²Π_{3/2} doublet states arising from the Th²⁺N²⁻ configuration. This is expected as the lowest electronic configuration that can produce quartet states is Th²⁺(7s6d)N²⁻(2p⁵). Table 3.11 lists the molecular constants and energies for the lowest quartet states. The lowest quartet state has an energy of 14,788 cm⁻¹ and many quartet states fall in the energy range that was probed in the REMPI and LIF experiments.

3.5 ThN Discussion

The congestion of the spectrum in Figure 3.1 can easily be explained by the predicted high density of states. The calculations also support the expectation that an ionic bonding model (more specifically one using ligand field theory) can be used to anticipate the families of the low-lying electronically excited state. *Ab initio* calculations for these families yielded molecular constants that were characteristic of the electronic configuration. In this study, groups of

electronic states exhibiting similar molecular constants can provide insight concerning the electronic configuration for those excited states.

Unfortunately, there was a lack of vibrational intervals in the observed spectra, which prohibits determination of the upper state vibrational assignments. Also, the DLIF spectra were not as useful as hoped. Spectra recorded with excitation of 19,946, 20,679, 20,937, 20,969, and 21,055 cm^{-1} had intensity distributions typical of $\nu' = 0$ states. The other transitions exhibited emissions to a range of ground $X^2\Sigma^+$ state vibrational levels. While these upper levels could be vibrationally excited, they also could be $\nu' = 0$ states that are considerably perturbed. Ambiguous results were also yielded from the fluorescence lifetime measurements. As can be seen from Tables 3.8 and 3.9, while the lifetimes were dependent on the excited state, no systematic trends were able to be established. Perturbed states exhibited lifetimes that were within the range of values of those of non-perturbed states. Similarly, states that exhibited quantitatively different DLIF spectra did not show characteristically different lifetimes.

One can also infer whether different electronic states arise from the same electronic configuration based on the similarity of their rotational constants. As can be seen from Tables 3.10 and 3.11, the *ab initio* results indicate that excited states with the formal $\text{Th}^{2+}\text{N}^{2-}$ configuration should have rotational constants slightly below 0.32 cm^{-1} . Most of the rotational constants obtain from fitting the band spectra were larger than 0.32 cm^{-1} but smaller than the $\text{Th}^{3+}\text{N}^{3-}$ value of 0.38 cm^{-1} . Looking at a simple model, it may be expected that excited states that yield long vibrational progressions in the ground state would have smaller rotational constants. This however was not supported by the experimental results. For example, the $20,604 \text{ cm}^{-1}$ state, which strongly emits down to the $X^2\Sigma^+ \nu'' = 4$, has a rotational constant of $B' = 0.3487 \text{ cm}^{-1}$.

Overall, the lack of systematic trends for ThN excited state properties indicates extensive state mixing that involves both doublet and quartet state manifolds. Dipole moment and magnetic g -factors⁶⁰⁻⁶³ provide other flags for configurational assignment but it seems likely that the information obtained will have similar ambiguities. For example, Le *et al.*⁵⁰ found that the magnetic g -factor for the [18.0]3/2 state was consistent with a Hund's case (a) $^2\Pi_{3/2}$ state. However, Le's interpretation required the assumption that this state was a double state and therefore did not yield any configurational insight. Measurements of the electric dipole moments for the [18.0]3/2 and $X^2\Sigma^+$ states yielded values of $\mu = 4.38$ and 5.11 D, respectively. In a first-order model, the change in the dipole moment upon excitation could indicate a charge-transfer transition as opposed to a transition of an electron within the metal center. However, the [18.0]3/2 rotational constant of 0.3525 cm^{-1} is significantly larger than the constants predicted for the charge transfer states and the change in the dipole moment is smaller than the *ab initio* predictions of $\Delta\mu > 2\text{D}$. This suggests that there are state mixings that not captured by the calculations performed in this work. Given, the similar characteristics of the charge-transfer potential energy curves of the doublet and quartet states, it does not appear that mixing of these manifolds would resolve this shortcoming. Higher level calculations, such as including the $6d$ orbital of Th in the active space, are needed to achieve a better understand of the low-lying electronically excited states of ThN.

3.6 Chapter 3 References

1. Runde, W.; Neu, M. P., Actinides in the Geosphere. Springer Netherlands: 2010; pp 3475-3593.
2. Vermeul, V. R.; Fruchter, J. S.; Fritz, B. G.; Mackley, R. D.; Wellman, D. M.; Williams, M. D., *In-Situ* Uranium Stabilization Through Polyphosphate Injection: Pilot-Scale Treatability Test at the 300 Area, Hanford Site - 8187. In *WM2008*, Phoenix, AZ, 2008.
3. Dolg, M.; Cao, X., Relativistic Pseudopotentials: Their Development and Scope of Applications. *Chemical Reviews* **2012**, *112* (1), 403-480.
4. Marsh, M. L.; White, F. D.; Galley, S. S.; Albrecht-Schmitt, T. E., Comparison of the Electronic Properties of f^7 , f^8 , and f^9 Lanthanides With Formally Isoelectronic Actinides. In *Handbook on the Physics and Chemistry of Rare Earths*, 2018; Vol. 53, pp 1-33.
5. Crosswhite, H. M.; Crosswhite, H.; Carnall, W. T.; Paszek, A. P., Spectrum analysis of U^{3+} : $LaCl_3$. *The Journal of Chemical Physics* **1980**, *72* (9), 5103-5117.
6. Choppin, G. R., Covalency in f-element bonds. *Journal of Alloys and Compounds* **2002**, *344* (1-2), 55-59.
7. Neidig, M. L.; Clark, D. L.; Martin, R. L., Covalency in f-element complexes. *Coordination Chemistry Reviews* **2013**, *257* (2), 394-406.
8. Nash, K. L.; Madic, C.; Mathur, J. N.; Lacquement, J., Actinide Separation Science and Technology. In *Chemistry of the Actinide and Transactinide Elements*, Springer: Berlin, 2006; Vol. 4, pp 2622-2798.
9. Prodan, I. D.; Scuseria, G. E.; Martin, R. L., Covalency in the actinide dioxides: Systematic study of the electronic properties using screened hybrid density functional theory. *Physical Review B* **2007**, *76* (3).

10. Jensen, M. P.; Bond, A. H., Comparison of Covalency in the Complexes of Trivalent Actinide and Lanthanide Cations. *Journal of the American Chemical Society* **2002**, *124* (33), 9870-9877.
11. Dine, M.; Kusenko, A., Origin of the matter-antimatter asymmetry. *Reviews of Modern Physics* **2003**, *76* (1), 1-30.
12. Sakharov, A. D., Violation of CP Invariance, C Asymmetry, and Baryon Asymmetry of the Universe. *JETP Lett.* **1966**, *5*, 24-27.
13. Engel, J.; Ramsey-Musolf, M. J.; Van Kolck, U., Electric dipole moments of nucleons, nuclei, and atoms: The Standard Model and beyond. *Progress in Particle and Nuclear Physics* **2013**, *71*, 21-74.
14. Safronova, M. S.; Budker, D.; Demille, D.; Kimball, D. F. J.; Derevianko, A.; Clark, C. W., Search for new physics with atoms and molecules. *Reviews of Modern Physics* **2018**, *90* (2).
15. Meyer, E. R.; Bohn, J. L., Prospects for an electron electric-dipole moment search in metastable ThO and ThF⁺. *Physical Review A* **2008**, *78* (1).
16. Fleig, T.; Nayak, M. K., Electron electric dipole moment and hyperfine interaction constants for ThO. *Journal of Molecular Spectroscopy* **2014**, *300*, 16-21.
17. Baron, J.; Campbell, W. C.; Demille, D.; Doyle, J. M.; Gabrielse, G.; Gurevich, Y. V.; Hess, P. W.; Hutzler, N. R.; Kirilov, E.; Kozyryev, I.; O'Leary, B. R.; Panda, C. D.; Parsons, M. F.; Petrik, E. S.; Spaun, B.; Vutha, A. C.; West, A. D., Order of Magnitude Smaller Limit on the Electric Dipole Moment of the Electron. *Science* **2014**, *343* (6168), 269-272.

18. Loh, H.; Cossel, K. C.; Grau, M. C.; Ni, K. K.; Meyer, E. R.; Bohn, J. L.; Ye, J.; Cornell, E. A., Precision Spectroscopy of Polarized Molecules in an Ion Trap. *Science* **2013**, *342* (6163), 1220-1222.
19. Denis, M.; Fleig, T., In search of discrete symmetry violations beyond the standard model: Thorium monoxide reloaded. *The Journal of Chemical Physics* **2016**, *145* (21), 214307.
20. Denis, M.; Norby, M. S.; Jorgen Aa Jensen, H.; Severo Pereira Gomes, A.; Nayak, M. K.; Knecht, S.; Fleig, T., Theoretical Study on ThF⁺, a prospective system in search of time-reversal violation. *New. J. Phys.* **2015**, *17*, 043005.
21. Andreev, V.; Ang, D. G.; Demille, D.; Doyle, J. M.; Gabrielse, G.; Haefner, J.; Hutzler, N. R.; Lasner, Z.; Meisenhelder, C.; O'Leary, B. R.; Panda, C. D.; West, A. D.; West, E. P.; Wu, X., Improved limit on the electric dipole moment of the electron. *Nature* **2018**, *562* (7727), 355-360.
22. Zhou, Y.; Ng, K. B.; Cheng, L.; Gresh, D. N.; Field, R. W.; Ye, J.; Cornell, E. A., Visible and ultraviolet laser spectroscopy of ThF. *Journal of Molecular Spectroscopy* **2019**, *358*, 1-16.
23. Edvinsson, G.; Selin, L. E., The band spectrum of thorium oxide. *Physics Letters* **1964**, *9* (3), 238-239.
24. Edvinsson, G. S., Lars-Erik; Aslund, Nils, On the band spectrum of ThO. *Arkiv For Fysik* **1965**, *30* (22), 283-319.
25. Edvinsson, G.; von Bornstedt, A.; Nylen, P., Rotational analysis for a perturbed ¹Π state in ThO. *Arkiv For Fysik* **1968**, *28*, 193-218.
26. Edvinsson, G.; Lagerqvist, A., Rotational Analysis of Yellow and Near Infrared Bands in ThO. *Physica Scripta* **1984**, *30*, 303-320.

27. Edvinsson, G.; Lagerqvist, A., A low-lying state in the ThO molecule. *Journal of Molecular Spectroscopy* **1985**, *113* (1), 93-104.
28. Edvinsson, G.; Lagerqvist, A., Rotational Analysis of two Red Band Systems in the ThO Spectrum. *Phys. Scr.* **1985**, *32*, 602-610.
29. Edvinsson, G.; Lagerqvist, A., Rotational analysis of some violet and green bands in the ThO spectrum. *Journal of Molecular Spectroscopy* **1987**, *122* (2), 428-439.
30. Edvinsson, G.; Lagerqvist, A., Two band systems of ThO in the near ultraviolet. *Journal of Molecular Spectroscopy* **1988**, *128* (1), 117-125.
31. Edvinsson, G.; Lagerqvist, A., Two New Band systems in ThO. *Phys. Scr.* **1990**, *41*, 316-320.
32. von Bornstedt, A.; Edvinsson, G., Rotational Analysis of two Mutually Interacting Electron States of $^1\Pi$ Character in ThO. *Phys. Scr.* **1970**, *2*, 205-210.
33. von Bornstedt, A.; Edvinsson, G.; Lagerqvist, A.; Renhorn, I., The Spectrum of ThO: Rotational Analysis of the $L^1\Pi-X^1\Sigma^+$ and $N^1\Pi-X^1\Sigma^+$ Systems. *Phys. Scr.* **1979**, *20*, 599-602.
34. Kokkin, D. L.; Steimle, T. C.; Demille, D., Characterization of the $I(|\Omega|=1)-X^1\Sigma^+(0,0)$ band of thorium oxide. *Physical Review A* **2015**, *91* (4).
35. Wang, F.; Le, A.; Steimle, T. C.; Heaven, M. C., Communication: The permanent electric dipole moment of thorium monoxide, ThO. *The Journal of Chemical Physics* **2011**, *134* (3), 031102.
36. Vutha, A. C.; Spaun, B.; Gurevich, Y. V.; Hutzler, N. R.; Kirilov, E.; Doyle, J. M.; Gabrielse, G.; Demille, D., Magnetic and electric dipole moments of the $H^3\Delta_1$ state in ThO. *Physical Review A* **2011**, *84* (3).

37. Kokkin, D. L.; Steimle, T. C.; Demille, D., Branching ratios and radiative lifetimes of the U,L, and I states of thorium oxide. *Physical Review A* **2014**, *90* (6), 062503.
38. Long, B. E.; Novick, S. E.; Cooke, S. A., Measurement of the J=1–0 pure rotational transition in excited vibrational states of X¹Σ thorium(II) oxide, ThO. *Journal of Molecular Spectroscopy* **2014**, *302*, 1-2.
39. Dewberry, C. T.; Etchison, K. C.; Cooke, S. A., The pure rotational spectrum of the actinide-containing compound thorium monoxide. *Physical Chemistry Chemical Physics* **2007**, *9* (35), 4895.
40. Dewberry, C. T.; Etchison, K. C.; Grubbs II, G. S.; Powoski, R. A.; Serafin, M. M.; Peebles, S. A.; Cooke, S. A., Oxygen-17 hyperfine structures in the pure rotational spectra of SrO, SnO, BaO, HfO and ThO. *Physical Chemistry Chemical Physics* **2007**.
41. Tyagi, R. Ab initio Studies of Systems Containing Actinides using Relativistic Effective Core Potentials. The Ohio State University, 2005.
42. Küchle, W.; Dolg, M.; Stoll, H.; Preuss, H., Energy-adjusted pseudopotentials for the actinides. Parameter sets and test calculations for thorium and thorium monoxide. *The Journal of Chemical Physics* **1994**, *100* (10), 7535-7542.
43. Goncharov, V.; Kaledin, L. A.; Heaven, M. C., Probing the electronic structure of UO⁺ with high-resolution photoelectron spectroscopy. *The Journal of Chemical Physics* **2006**, *125* (13), 133202.
44. Kaledin, L. A.; McCord, J. E.; Heaven, M. C., Laser Spectroscopy of UO: Characterization and Assignment of States in the 0- to 3-eV Range, with a Comparison to the Electronic Structure of ThO. *Journal of Molecular Spectroscopy* **1994**, *164* (1), 27-65.

45. Kaledin, L. A.; Kaledin, A. L.; Heaven, M. C., The electronic structure of thorium monoxide: Ligand field assignment of states in the range 0–5 eV. *Journal of Computational Chemistry* **2019**, *40* (2), 430-446.
46. Gatterer, A.; Junkes, J.; Salpeter, E. W.; Rosen, B., Molecular spectra of metallic oxides. *Specola Vaticana* **1957**.
47. Edvinsson, G.; Lageqvist, A., Rotational Analysis of two Red Band Systems in the ThO Spectrum. *Phys. Scr.* **1982**, *32*, 602-610.
48. Castano, F.; De Juan, J.; Martinez, E., The calculation of potential energy curves of diatomic molecules: the RKR method. *Journal of Chemical Education* **1983**, *60* (2), 91.
49. Heaven, M. C.; Barker, B. J.; Antonov, I. O., Spectroscopy and structure of the simplest actinide bonds. *J Phys Chem A* **2014**, *118* (46), 10867-81.
50. Le, A. T.; Nakhate, S. G.; Nguyen, D.-T.; Steimle, T. C.; Heaven, M. C., Characterization of gas-phase thorium nitride. *The Journal of Chemical Physics* **2019**, *150* (14), 144304.
51. Kushto, G. P.; Souter, P. F.; Andrews, L., An infrared spectroscopic and quasirelativistic theoretical study of the coordination and activation of dinitrogen by thorium and uranium atoms. *The Journal of Chemical Physics* **1998**, *108* (17), 7121-7130.
52. Western, C. M., PGOPHER: A program for simulating rotational, vibrational and electronic spectra. *Journal of Quantitative Spectroscopy and Radiative Transfer* **2017**, *186*, 221-242.
53. LeRoy, R. J., Pashov, Asen, betaFIT; A computer program to fit pointwise potentials to selected analytic functions. *Journal of Quantitative Spectroscopy and Radiative Transfer* **2017**, *186*, 210-220.

54. Leroy, R. J., LEVEL: A computer program for solving the radial Schrodinger equation for bound and quasibound levels. *Journal of Quantitative Spectroscopy and Radiative Transfer* **2017**, *186*, 167-178.
55. Werner, H.-J.; Knowles, P. J.; Knizia, G.; Manby, F. R.; Schütz, M., Molpro: a general-purpose quantum chemistry program package. *Wiley Interdisciplinary Reviews: Computational Molecular Science* **2012**, *2* (2), 242-253.
56. Werner, H.-J.; Knowles, P. J.; Manby, F. R.; Black, J. A.; Doll, K.; Heßelmann, A.; Kats, D.; Köhn, A.; Korona, T.; Kreplin, D. A.; Ma, Q.; Miller, T. F.; Mitrushchenkov, A.; Peterson, K. A.; Polyak, I.; Rauhut, G.; Sibae, M., The Molpro quantum chemistry package. *The Journal of Chemical Physics* **2020**, *152* (14), 144107.
57. Cao, X.; Dolg, M., Segmented contraction scheme for small-core actinide pseudopotential basis sets. *Journal of Molecular Structure (Theochem)* **2004**, *673*, 203-209.
58. Cao, X.; Dolg, M.; Stoll, H., Valence basis sets for relativistic energy-consistent small-core actinide pseudopotentials. *The Journal of Chemical Physics* **2003**, *118* (2), 487-496.
59. Dunning, T. H., Gaussian basis sets for use in correlated molecular calculations. I. The atoms boron through neon and hydrogen. *The Journal of Chemical Physics* **1989**, *90* (2), 1007-1023.
60. Heaven, M. C.; Goncharov, V.; Steimle, T. C.; Ma, T.; Linton, C., The permanent electric dipole moments and magnetic g factors of uranium monoxide. *The Journal of Chemical Physics* **2006**, *125* (20), 204314.
61. Linton, C.; Adam, A. G.; Steimle, T. C., Stark and Zeeman effect in the [18.6]3.5 – X(1)4.5 transition of uranium monofluoride, UF. *The Journal of Chemical Physics* **2014**, *140* (21), 214305.

62. Nguyen, D.-T.; Steimle, T.; Linton, C.; Cheng, L., Optical Stark and Zeeman Spectroscopy of Thorium Fluoride (ThF) and Thorium Chloride (ThCl). *The Journal of Physical Chemistry A* **2019**, *123* (7), 1423-1433.
63. Schall, H.; Gray, J. A.; Dulick, M.; Field, R. W., Sub-Doppler Zeeman spectroscopy of the CeO molecule. *The Journal of Chemical Physics* **1986**, *85* (2), 751-762.

Chapter 4

Perturbations of the $A'^1\Pi(X\sigma\pi^{-1})$ and

$C^1\Sigma^+(B\sigma\sigma^{-1})$ States of CaO

The contents and figures of this chapter are reprinted or adapted with permission from
Bresler, S.M., Schmitz, J.R., Heaven, M.C., Field, R.W. Perturbations of the $A'^1\Pi$ and $C^1\Sigma^+$
states of CaO. *J. Mol. Spec.* **2020**, 370, 111293.

4.1 Introduction

The electronic spectrum of CaO is complex due to the large number of low-lying electronic states and the numerous rovibronic interactions between them. The ground and low-lying excited states CaO have been extensively theoretically and experimentally characterized¹⁻¹³, with the majority of experimental methods employing laser-induced fluorescence. To explain the electronic structure of the excited states of CaO, Field and co-workers have developed an atomic-ions-in-molecule ligand field model, as well as a configurational notation^{8,14} that greatly facilitates the discussion of the excited states. The ground state of CaO is $X^1\Sigma^+$ is formally attributed to a closed-shell $\text{Ca}^{2+}(^1S_0)\text{O}^{2-}(^1S_0)$ configuration and is the only electronic state arising from this configuration. The low-lying excited states are attributed to configurations arising from a $\text{Ca}^+ + \text{O}^-$ atomic pair. and can be mapped as combinations of molecular states of CaF and NaO. The molecular states of CaF are chosen to model the free Ca^+ ion¹⁵, treating the closed-shell halide as a polarizable point charge that minimally perturbs the atomic energies of Ca^+ . In the same way, NaO molecular states¹⁶ are used to model the free $\text{O}^-(2p^5)$ atom, treating the closed-shell Na^+ atom as a point charge. The resulting picture is one of extreme electron localization: one electron localized on a Ca^{2+} center and an electron p -hole on O^- . In the notation for the excited states of CaO, Ca^+ orbitals are labeled with their corresponding CaF electronic states. For example, the Ca^+ orbitals $X\sigma$, $A\pi$, and $B\sigma$ correspond to the CaF $X^2\Sigma^+$, $A^2\Pi$, and $B^2\Sigma^+$ states. For O^- , the p -hole orbitals are labeled as π^{-1} or σ^{-1} depending on their orientation with respect to the Ca^+ atom and correspond to the $X^2\Pi$ and $A^2\Sigma^+$ NaO states, respectively. Various permutations of these atomic-ion orbitals give the electronic configurations of CaO. For example, the $\text{Ca}^+(4s)\text{O}^-(2p\sigma^2 2p\pi^3)$ configuration is specified as $X\sigma\pi^{-1}$ and gives rise to the molecular states $A^1\Pi$ and $a^3\Pi$

states. Figure 4.1 shows a simplification of the molecular orbitals for the $X\sigma\pi^{-1}$ and $B\sigma\sigma^{-1}$ CaO configurations.

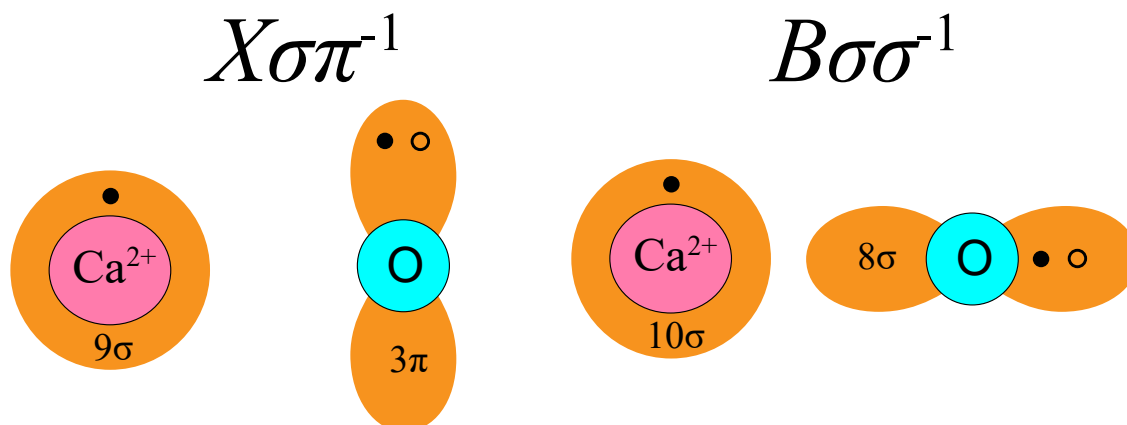


Figure 4.1. Illustration of the molecular orbitals of the CaO $X\sigma\pi^{-1}$ and $B\sigma\sigma^{-1}$ electronic configurations.

High-level theoretical studies have also been performed on CaO, focused mainly on the ground $^1\Sigma^+$ state and the excited electronic states arising from the $X\sigma\pi^{-1}$ ($A^1\Pi$ and $a^3\Pi$) and $X\sigma\sigma^{-1}$ ($A^1\Sigma^+$ and $b^3\Sigma^+$) configurations^{4, 17-21}. Khalil *et al.*^{19, 20} used high-level multi-reference configuration (MRCI) methods of basis sets of 5-zeta to predict the potential energy curves, dipole moments, and electronic transition dipole moments for the $X^1\Sigma^+$, $A^1\Sigma^+$, $A^1\Pi$, $a^3\Pi$, and $b^3\Sigma^+$ states. The potential energy curves and wavefunctions were then used to calculate the rovibronic eigenstates¹⁹. Spin-orbit and L -uncoupling perturbations were included and produced results that were directly comparable with measured term energies. In 2016, Yurchenko *et al.*²² refined the potential energy curves along with the perturbation matrix elements of Khalil *et al.* by fitting to a very extensive set of experimentally determined term energies. Yurchenko also determined Einstein A_{ij} coefficients for spontaneous emission. The ExoMol database²³ has since included Yurchenko's data, being used for the identification of molecular species in the

absorption and emission spectra of astrophysical objects. The database was used in 2018 to detect CaO orange emission bands from the wake of a meteorite²⁴.

Yurchenko *et al.*²² provided a comprehensive summary of the experimental studies of the CaO spectrum. Specific studies will be mentioned here that are relevant to this work. Data for the $A^1\Pi(X\sigma\pi^{-1})$ state was obtained from emission spectra and deperturbation analyses. Field *et al.*¹² vibrationally resolved $A^1\Pi(X\sigma\pi^{-1})$ - $X^1\Sigma^+$ chemiluminescence and reported band heads that included the $A^1\Pi(X\sigma\pi^{-1})$ vibrational levels $\nu = 9$ -21. Focsa *et al.*²⁵ obtained rotationally resolved $A^1\Pi(X\sigma\pi^{-1})$ - $X^1\Sigma^+$ emission bands, originating from the $A^1\Pi(X\sigma\pi^{-1})$ $\nu = 0$ -3 levels. Perturbations of the $A^1\Pi(X\sigma\pi^{-1})$ $\nu = 2,3$ levels were analyzed and attributed to interactions with the $b^3\Sigma^+(X\sigma\sigma^{-1})$ state.

The $a^3\Pi(X\sigma\pi^{-1})$ state was observed as part of the orange bands of CaO and the $\nu = 0$ level was characterized through $c^3\Sigma^+(A\pi\pi^{-1})$ - $a^3\Pi(X\sigma\pi^{-1})$, $d^3\Delta(A\pi\pi^{-1})$ - $a^3\Pi(X\sigma\pi^{-1})$, and $e^3\Sigma^-(A\pi\pi^{-1})$ - $a^3\Pi(X\sigma\pi^{-1})$ 0-0 bands^{5, 8, 10, 11}. Data for the vibrationally excited levels was taken from the $d^3\Delta(A\pi\pi^{-1})$ - $a^3\Pi(X\sigma\pi^{-1})$ 1-1 and $B^1\Pi(A\pi\sigma^{-1})$ - $a^3\Pi_{0+}(X\sigma\pi^{-1})$ 3-0 bands. Information for the $a^3\Pi_{0+}(X\sigma\pi^{-1})$ $\nu = 6,9,12$ levels were taken from perturbations from the $a^3\Pi_{0+}(X\sigma\pi^{-1})$ state interacting with the $A^1\Sigma^+(X\sigma\sigma^{-1})$ state. Field¹³ and Fosca *et al.*²⁵ also investigated perturbations between the $A^1\Sigma^+(X\sigma\sigma^{-1})$ and $b^3\Sigma^+(X\sigma\sigma^{-1})$ states.

Spin-orbit perturbations between the $A^1\Pi(X\sigma\pi^{-1})$ and $b^3\Sigma^+(X\sigma\sigma^{-1})$ states have also been observed. The $A^1\Pi(X\sigma\pi^{-1})$ state is a pure $\Omega = 1$ state, with each rotational J level being split into two states with e - and f -symmetry components. The $b^3\Sigma^+(X\sigma\sigma^{-1})$ state has three spin-components: F_1 , F_2 , and F_3 . F_1 and F_3 are of f -symmetry and approximately 50:50 mixtures of $\Omega = 0$ and 1 whereas F_2 is of e -symmetry and pure $\Omega = 1$ character. The spin-orbit interaction between the $A^1\Pi(X\sigma\pi^{-1})$ and $b^3\Sigma^+(X\sigma\sigma^{-1})$ states is homogeneous and therefore follows the $\Delta\Omega = 0$ selection

rule. Perturbations involving the F_1 and F_3 components of the $b^3\Sigma^+(X\sigma\sigma^{-1})$ state will be observable in the Q-branch of the $A^1\Pi(X\sigma\pi^{-1})-X^1\Sigma^+$ transition while those involving the F_2 component will be observable in the P/R branches.

Higher energy states originating from the $A\pi\pi^{-1}$, $A\pi\sigma^{-1}$, $B\sigma\pi^{-1}$, and $B\sigma\sigma^{-1}$ configurations have also been investigated^{1,2,7-9,26}. Stewart *et al.*²⁶ examined the laser-induced fluorescence (LIF) spectrum of jet-cooled CaO in the energy range of 28,000-33,150 cm^{-1} . Vibrationally-excited $C^1\Sigma^+(B\sigma\sigma^{-1})-X^1\Sigma^+$ and $F^1\Pi(B\sigma\pi^{-1})-X^1\Sigma^+$ transitions were observed as well as three vibrational bands of an unidentified $\Omega = 0^+-X^1\Sigma^+$ ($v'' = 0$) transition. This 0^+ state will further be identified as the $\gamma 0^+$ state in this work. One of the $\gamma 0^+$ vibrational states was found to perturb the $C^1\Sigma^+(B\sigma\sigma^{-1}) v = 7$ level, pushing the state up by nearly 7 cm^{-1} . By extrapolating the known vibrational levels of the $C^1\Sigma^+(A\pi\pi^{-1})$ state, Stewart *et al.*²⁶ proposed that the $\gamma 0^+-X^1\Sigma^+$ bands could be part of the $C^1\Sigma^+(A\pi\pi^{-1})-X^1\Sigma^+$ system. However, based on the spin-orbit selection rules of perturbations mediated by a one-electron operator, Field²⁷ argued that the matrix elements between the $C^1\Sigma^+(A\pi\pi^{-1})$ and $C^1\Sigma^+(B\sigma\sigma^{-1})$ states would be too small. He therefore proposed that the $g^3\Pi_{0+}(B\sigma\pi^{-1})$ or $f^3\Pi_{0+}(A\pi\sigma^{-1})$ states would be more viable candidates for the $\gamma 0^+$ state and that the triplet character could be established through the dispersed fluorescence spectrum.

In this work, there were two motivations for the reexamination of the spectrum of jet-cooled CaO. Initially a search for the hypermetallic oxide CaOCa was carried out in the red spectral range of 13,700-17,150 cm^{-1} . CaO bands were present under the survey conditions and rotationally-resolved spectra for the $A^1\Pi(X\sigma\pi^{-1})-X^1\Sigma^+$ transitions with $v' = 10-17$ were obtained. The second objective was to determine the identity of the $\gamma 0^+$ state perturbing the $C^1\Sigma^+(B\sigma\sigma^{-1}) v = 7$ state through wavelength- and time-resolved fluorescence. This work will describe the effort to

characterize the $A'^1\Pi(X\sigma\pi^{-1})-X^1\Sigma^+ v' = 10-17$ transitions as well as the identification of the $\gamma 0^+$ state.

4.2 CaO Results

4.2.1 The $A'^1\Pi(X\sigma\pi^{-1})-X^1\Sigma^+$ bands

LIF spectra were recorded from 13,700-17,150 cm^{-1} , which was mostly dominated by $A^1\Sigma^+(X\sigma\sigma^{-1})-X^1\Sigma^+$ and $A'^1\Pi(X\sigma\pi^{-1})-X^1\Sigma^+$ transitions. The two different kinds of transitions were distinguishable from each other due to the Q-branches in the $A'^1\Pi(X\sigma\pi^{-1})-X^1\Sigma^+$ bands resulting from the change in orbital angular momentum $\Delta\Lambda = 1$. The lifetimes of the $A'^1\Pi(X\sigma\pi^{-1})-X^1\Sigma^+$ bands were also much longer than those of the $A^1\Sigma^+(X\sigma\sigma^{-1})-X^1\Sigma^+$ bands, providing another source of distinguishability. Figure 4.2 shows the rotational structure of the $A'^1\Pi(X\sigma\pi^{-1})-X^1\Sigma^+$ 10-0 band along with a theoretical simulation generated by PGOPHER²⁸, which was also used to fit the $A'^1\Pi(X\sigma\pi^{-1})$ state band origins and rotational constants.

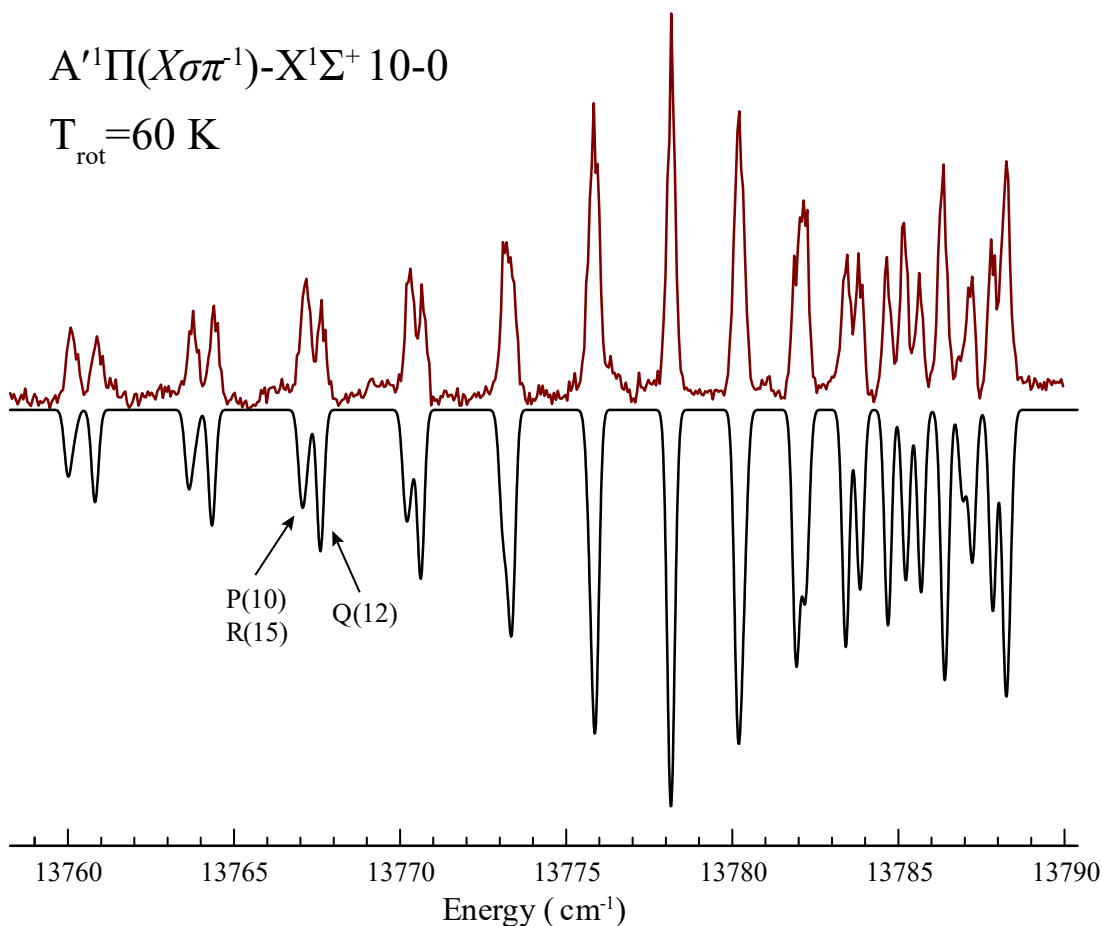


Figure 4.2. LIF spectrum of the CaO $A'^1\Pi(X\sigma\pi^{-1})-X^1\Sigma^+ 10-0$ band. The downward going trace is a simulation at a rotational temperature of 60 K generated in PGOHPER.

Focsa *et al.*²⁵ observed a combination difference defect between the Q lines and the P/R lines in the $A'^1\Pi(X\sigma\pi^{-1})-X^1\Sigma^+$ bands due to these transitions sampling f - and e -symmetry lambda-doublet components, respectively. However, this combination defect was below the precision of this work and the bands observed were fit without any lambda-doubling parameters. An attempt was made to fit centrifugal distortion constants but the results were statistically insignificant due to the limited number of observed rotational levels, an effect of the cold rotational temperature of the molecule. The theoretical calculations of Yurchenko *et al.*²² provide some indication of the magnitude of the neglected constants. Examination of the $A'^1\Pi(X\sigma\pi^{-1})$ energy levels from the

Exomol database indicates that the lambda doubling splitting of $\nu = 10$ increases from 5×10^{-4} cm^{-1} for $J = 1$ to 0.08 cm^{-1} at $J = 25$ (the typical rotational range observed in the spectrum). Fitting to the mean energies of the e - and f -parity levels yields a centrifugal distortion constant of $4.4 \times 10^{-7} \text{ cm}^{-1}$, which is in reasonable agreement with the prediction from the Kratzer relationship of $D_e = 5.5 \times 10^{-7} \text{ cm}^{-1}$. In this work, these constants were set to zero in the rotational fits, as the sufficient resolution to determine the lambda doubling splitting and the distortion constants was lacking. There also was no reliable method to predict their values due to the presence of perturbations. Therefore, only the band origins and upper state rotational constants were varied in the spectral fitting. A ground $X^1\Sigma^+ \nu'' = 0$ value²⁵ of 0.4428 cm^{-1} was fixed in the fits. The fitting results are listed in Tables 4.1. The 1σ errors in B_ν and $T_{\nu,0}$ are 0.0005 and 0.05 cm^{-1} , respectively.

Table 4.1. Molecular constants for the $A^1\Pi(X\sigma\pi^1)$ state determined from rotational fits of the LIF spectra and lifetime measurements.

ν	B_ν (cm^{-1})	$T_{\nu,0}$ (cm^{-1})	δE (cm^{-1}), Field <i>et al.</i> ¹²	δE (cm^{-1}), Yurchenko <i>et al.</i> ²²	Number of lines in fit	τ (μs)
10	0.3175	13787.23	2.8	-0.8	38	2.4
11	0.3148	14276.94	3.1	-1.1	63	2.7
12	0.3121	14761.41	1.6	-1.7	60	2.6
13	0.3101	15240.50	2.5	-2.1	52	2.5
14	0.3074	15714.72	0.3	-2.8	64	2.6
15	0.3039	16184.08	2.5	-3.5	26	2.8
16	0.3014	16648.80	5.2	-4.5	20	2.9
17	0.3016	17180.85	4.2	-10.7	24	2.7

Rovibrational constants for the $A^1\Pi(X\sigma\pi^1)$ state were determined by fitting the non-perturbed vibrational levels. Values for the energies of the $\nu = 0,1$ states were used from Focsa *et al.*²⁵ and the values for the $\nu = 10-15$ states were taken from this work. Vibrational energies were fit to

$$T_{v,0} = T_{0,0} + \omega_e v - \omega_e x_e v(v + 1) \quad (4.1)$$

The standard deviation of the fit was 0.23 cm⁻¹ and the constants are listed in Table 4.2.

Including the anharmonic constant $\omega_e y_e$ did not yield a statistically significant value so it was not included in the final fits. Rotational parameters for the same vibrational levels were fit according to

$$B_v = B_e - \alpha_e \left(v + \frac{1}{2} \right) \quad (4.2)$$

The standard deviation of $B_v(obs) - B_v(fit)$ was 0.0007 cm⁻¹ and the resulting constants are listed as well in Table 4.2.

Table 4.2. Rovibrational constants of the A¹Π(Xσπ⁻¹) state obtained vibrational energy fits.

Parameter	Value (cm ⁻¹)
$T_{0,0}$	8608.1(2)
ω_e	546.2(1)
$\omega_e x_e$	2.57(1)
B_e	0.3440(15)
α_e	2.55(11) x 10 ⁻³

Fluorescence decay lifetimes were recorded for all rotationally resolved A¹Π(Xσπ⁻¹)-X¹Σ⁺ bands. It was found that there was no significant difference in the fluorescence lifetimes with the rotational level within the same vibronic transition. Consequently, the lifetimes reported here were obtained from measurements made using excitation of the most intense rotational line of a given band. Each fluorescence decay curve was well-defined by a single exponential function and the fitted lifetimes are listed in Table 4.1. The determined standard deviation of the lifetime measures was ±0.2 μs.

4.2.2 Wavelength and Time-Resolved Fluorescence Measurements for the $C^1\Sigma^+(B\sigma\sigma^{-1})$ and $\gamma 0^+$ States

Stewart *et al.*²⁶ observed $\gamma 0^+ - X^1\Sigma^+$ transitions at 32037.0, 32479.5, and 32955.2 cm^{-1} , corresponding to upper vibrational states levels denote as $n - 1$, n , and $n + 1$. The $\gamma 0^+$ n state interacts strongly with the $C^1\Sigma^+(B\sigma\sigma^{-1})$ $\nu = 7$ level while the $n - 1$ and the $n + 1$ levels lie above and below the $C^1\Sigma^+(B\sigma\sigma^{-1})$ $\nu = 6$ and $\nu = 8$ states, respectively. The smaller vibrational spacing of the $\gamma 0^+$ state relative to that of the $C^1\Sigma^+(B\sigma\sigma^{-1})$ state suggests that the $\gamma 0^+$ state arises from a π^{-1} configuration. To assign a configuration to the $\gamma 0^+$, DLIF spectra were recorded for excitation to each of the $\gamma 0^+$ levels and to the $C^1\Sigma^+(B\sigma\sigma^{-1})$ $\nu = 6, 7, 8$ levels. Figure 3 shows these spectra, where the energy scale is relative to the $X^1\Sigma^+$ $\nu'' = 0$ level.

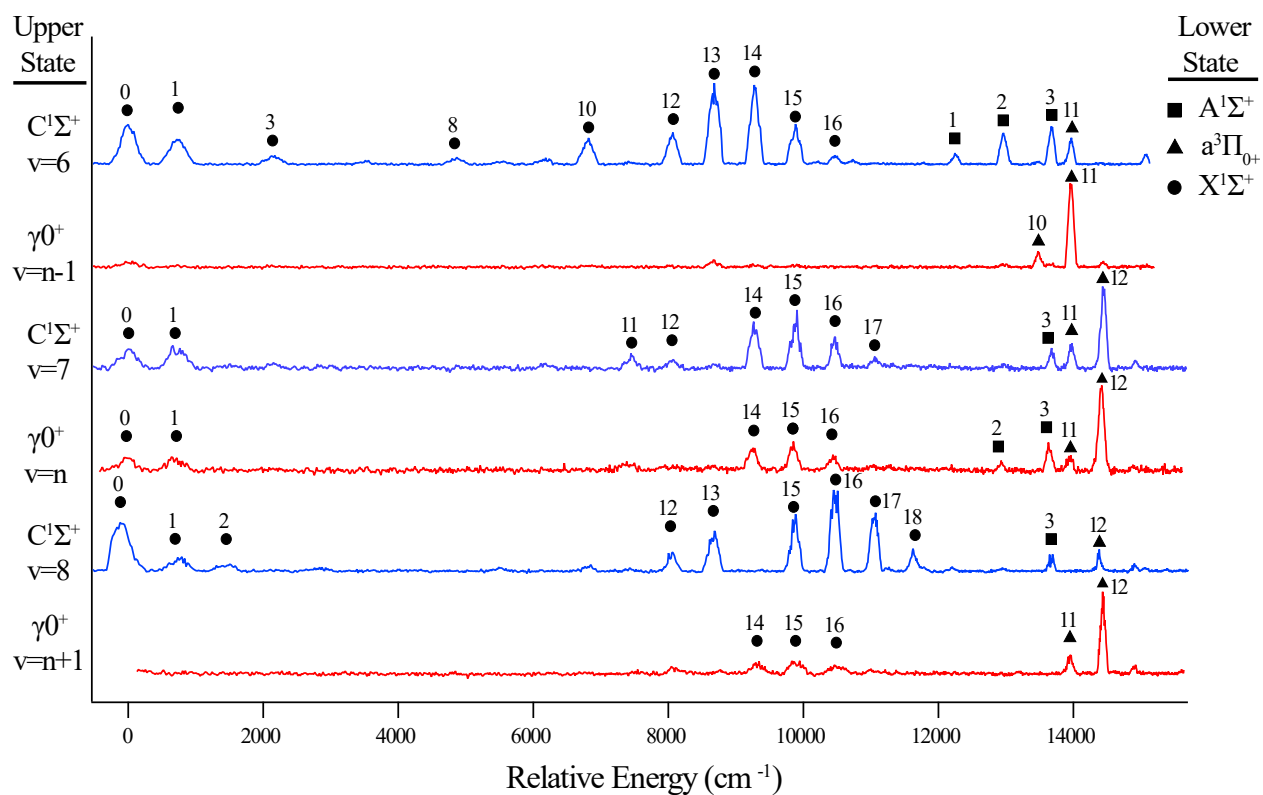


Figure 4.3. Dispersed fluorescence spectra for CaO of the states $C^1\Sigma^+(B\sigma\sigma^{-1}) v = 6, 7, 8$ and $\gamma^0 v = n-1, n, n+1$. The filled symbols indicate the lower electronic state with $\bullet = X^1\Sigma^+$, $\blacksquare = A^1\Sigma^+(X\sigma\sigma^{-1})$, and $\blacktriangle = a^3\Pi_{0+}(X\sigma\pi^{-1})$.

All of the fluorescence transitions to states within $12,000 \text{ cm}^{-1}$ of the $X^1\Sigma^+ v'' = 0$ state terminate on vibrationally-excited levels of the ground $X^1\Sigma^+$ state. The emissions observed in the $12,000$ - $16,000 \text{ cm}^{-1}$ range terminate on either $A^1\Sigma^+(X\sigma\sigma^{-1}) v = 1-5$ or $a^3\Pi_{0+}(X\sigma\pi^{-1}) v = 10-12$ states.

Fluorescence lifetimes were measured for the six upper states and are presented in Table 4.3. The standard deviation for the lifetime measurements was $\pm 5 \text{ ns}$. Decay curves were obtained by with the dye laser tuned to the band head for each vibronic transition, corresponding to upper state of $J' = 4$.

Table 4.3. Fluorescence decay lifetimes for the $C^1\Sigma^+(B\sigma\sigma^{-1})$ and $\gamma 0^+$ vibrational states.

Electronic State	ν	τ (ns)
$C^1\Sigma^+(B\sigma\sigma^{-1})$	6	29
	7	32
	8	24
$\gamma 0^+$	$n - 1$	46
	n	35
	$n + 1$	42

4.3 Discussion

4.3.1 $A^1\Pi(X\sigma\pi^{-1}) \nu = 17$ Perturbation

In Table 4.1, the band origin data for the $A^1\Pi(X\sigma\pi^{-1})$ state are compared to the experimental results of Field *et al.*¹² and the ExMol²² line lists with the energy difference between the values of this work and literature. Field *et al.* reported band head data for the red-shaded emission bands so it was expected that the reported band heads would lie roughly 2 cm^{-1} higher in energy than the band origins from this work. This expectation is realized in Table 4.1 where most of the band origins lie within this 2 cm^{-1} difference of Field's band head measurements. The difference between the ExoMol value for the R(0) transition energy and the measured values in this work are also listed in Table 4.1. This difference is seen to increase with increasing ν , with the $\nu = 17$ exhibiting a significant deviation. From both the band origin and its rotational constant, the $\nu = 17$ state appears to be greatly perturbed. Rotational constants from the ExoMol data were generated by fitting the rotational energy to the rigid rotor energy expression

$$E_\nu(J) = B_\nu J(J + 1) \quad (4.3)$$

for the range of rotational levels observed in the LIF spectra ($J = 1-25$). The ExoMol rotational constants generated agreed within the experimental uncertainties of the constants in Table 4.1, with the exception of B_{16} and B_{17} . The predicted values of 0.3026 and 0.3062 cm^{-1} disagreed with

the experimental values of 0.3014 and 0.3016 cm^{-1} , further indicating the presence of a perturbation in the energy range of the $A'^1\Pi(X\sigma\pi^{-1})$ $v = 17$ levels.

The energy level predictions from the ExoMol model were examined to identify the source of the perturbation of the $A'^1\Pi(X\sigma\pi^{-1})$ $v = 17$ state. It became apparent that the calculated energies of the $A'^1\Pi(X\sigma\pi^{-1})$ $v = 17$ (17098.7 cm^{-1}) and $b^3\Sigma^+(X\sigma\sigma^{-1})$ $v = 14$ (17109.9 cm^{-1}) were close enough for a significant interaction. These states can be coupled by the one-electron spin-orbit operator to give matrix elements of the form^{13, 25}

$$H_{SO} = \frac{a_\pi}{\sqrt{2}} \langle A', v' | b, v \rangle \quad (4.4)$$

where a_π is the spin-orbit constant for O^- with an approximate value¹³ of 121 cm^{-1} and the bra-ket term is the vibrational wavefunction overlap integral. This model was quantitatively tested by making Morse potential energy curves for the $A'^1\Pi(X\sigma\pi^{-1})$ and $b^3\Sigma^+(X\sigma\sigma^{-1})$ states to generate vibrational wavefunctions and overlap integrals. The molecular constants listed in Table 4.1 were used to generate the potential energy curve for the $A'^1\Pi(X\sigma\pi^{-1})$ state. Generating the potential energy curve for the $b^3\Sigma^+(X\sigma\sigma^{-1})$ was more difficult due to the lack of spectroscopic data, as only the $v = 1$ state has been observed⁶. As a starting point, theoretically predicted values²⁰ of $T_0 = 9282$, $\omega_e = 585.7$, and $\omega_{ex_e} = 3.16$ cm^{-1} with an equilibrium bond length of $r_e = 1.96$ Å were used. The generated energy levels were then compared to the experimentally determined term energy for $b^3\Sigma^+(X\sigma\sigma^{-1})$ $v = 1$ and the ExoMol predictions. Using the above molecular constants, the energy of the $b^3\Sigma^+(X\sigma\sigma^{-1})$ $v = 1$ state is underestimated, as well as the ExoMol prediction that the $b^3\Sigma^+(X\sigma\sigma^{-1})$ $v = 14$ state lies just above the $A'^1\Pi(X\sigma\pi^{-1})$ $v = 17$ state. Consequently, the values for T_0 , ω_e , and ω_{ex_e} were adjusted to produce both the experimentally determined energy for the $b^3\Sigma^+(X\sigma\sigma^{-1})$ $v = 1$ state as well as the ExoMol prediction for the $b^3\Sigma^+(X\sigma\sigma^{-1})$ $v = 14$ state. This resulted in values of $T_0 = 9489$, $\omega_e = 590.4$, and $\omega_{ex_e} = 3$ cm^{-1} . Frank-Condon factors for

$A'^1\Pi(X\sigma\pi^-)$ - $b^3\Sigma^+(X\sigma\sigma^-)$ were then calculated using LeRoy's²⁹ program Level 8.0 and the unsigned overlap integrals were obtained as the square roots of the Franck Condon factors. This yielded $|\langle v' = 17 | v = 14 \rangle| = 0.054$ and a spin-orbit matrix element of $|H_{SO}| = 4.6 \text{ cm}^{-1}$. Unperturbed rotational constants were predicted to be $B_{17} = 0.300 \text{ cm}^{-1}$ for $A'^1\Pi(X\sigma\pi^-)$ and $B_{14} = 0.344 \text{ cm}^{-1}$ for $b^3\Sigma^+(X\sigma\sigma^-)$. With an energy gap of 12 cm^{-1} between the $J=0$ levels of the unperturbed $A'^1\Pi(X\sigma\pi^-)$ $v = 17$ and $b^3\Sigma^+(X\sigma\sigma^-)$ $v = 14$ levels, a two-state perturbation model produced the experimental value for the effective rotational constant for the low rotational levels of $A'^1\Pi(X\sigma\pi^-)$ $v = 17$. The model indicated that the band origin had been pushed down by 1.6 cm^{-1} . The $A'^1\Pi(X\sigma\pi^-)$ $v = 16$ and $b^3\Sigma^+(X\sigma\sigma^-)$ $v = 13$ pair was also investigated to observe the degree of their interaction, as compared to the perturbing $A'^1\Pi(X\sigma\pi^-)$ $v = 17$ and $b^3\Sigma^+(X\sigma\sigma^-)$ $v = 14$ pair. It was found that the $b^3\Sigma^+(X\sigma\sigma^-)$ $v = 13$ state lied 30 cm^{-1} below the $A'^1\Pi(X\sigma\pi^-)$ $v = 16$ level with a small overlap integral of $|\langle v' = 16 | v = 13 \rangle| = 0.0046$, making this interaction irrelevant with respect to the resolution of previous experiments. Overall, this analysis supports the assignment of the $A'^1\Pi(X\sigma\pi^-)$ $v = 17$ perturbation to interaction with the $b^3\Sigma^+(X\sigma\sigma^-)$ $v = 14$ state.

Fluorescence lifetime measurements for the $A'^1\Pi(X\sigma\pi^-)$ state were found to be nearly independent of the vibrational state over the range of $v = 10$ - 17 . Field¹³ reported that the transition dipole moment for $A'^1\Pi(X\sigma\pi^-)$ - $X^1\Sigma^+$ is small, resulting in spontaneous lifetimes on the order of $10 \mu\text{s}$. The lifetimes reported in Table 4.1 are not quite that long but are consistent with the argument by Field¹³. As the ExoMol database includes Einstein A_{ij} coefficients, it was possible to generate theoretical values for the lifetime of the $A'^1\Pi(X\sigma\pi^-)$ state by summing the Einstein coefficients over all final states. This resulted in lifetimes that decreases from $11.4 \mu\text{s}$ for $v = 10$ down $8.5 \mu\text{s}$ for $v = 15$. The predicted lifetime for $v = 17$ was $15.4 \mu\text{s}$. These results

suggest that the calculated Einstein coefficient for the $A^1\Pi(X\sigma\pi^{-1}) v = 17$ level has been decreased by mixing with a long-lived state. This prediction, however, is not supported by the lifetime measurements of this work.

4.3.2 Assignment of the $\gamma 0^+$ state as the $g^3\Pi_{0+}(B\sigma\pi^{-1})$ state

Dispersed fluorescence and lifetime measurements for both the $C^1\Sigma^+(B\sigma\sigma^{-1})$ and $\gamma 0^+$ states provide useful insights for determination of the configurational parentage of the $\gamma 0^+$ state. If one considers the $C^1\Sigma^+(B\sigma\sigma^{-1}) v = 6$ and $\gamma 0^+ n - 1$ states, the energy separation between them is 59.4 cm^{-1} , large enough to expect only weak state mixing. The DLIF spectrum of the $C^1\Sigma^+(B\sigma\sigma^{-1}) v = 6$ state in Figure 4.3 shows that this state radiates down to $X^1\Sigma^+$ and $A^1\Sigma^+(X\sigma\sigma^{-1})$, which is expected with respect to Hund's case (a) angular momentum selection rules. There is however a transition to the $a^3\Pi_{0+}(X\sigma\pi^{-1}) v = 11$ state, probably mediated by the mixing of the lower level with $X^1\Sigma^+$ and $A^1\Sigma^+(X\sigma\sigma^{-1})$ states as reported by Khalil *et al.*¹⁹. In contrast, the DLIF spectrum of $\gamma 0^+ n - 1$ is dominated by transitions to the $a^3\Pi_{0+}(X\sigma\pi^{-1}) v = 10, 11$ levels. In the $\gamma 0^+ n - 1$ spectrum, emissions to singlet states are barely discernable above the noise level. This is a clear indicator that the $\gamma 0^+$ state is a triplet state. Furthermore, the short radiative lifetime of the $\gamma 0^+ n - 1$ state infers that the $\gamma 0^+ - a^3\Pi_{0+}(X\sigma\pi^{-1})$ transition has a large transition dipole moment. Similar trends exist for the $C^1\Sigma^+(B\sigma\sigma^{-1}) v = 8$ and $\gamma 0^+ n + 1$ pair, which are separated by 52.3 cm^{-1} . As with the $\gamma 0^+ n - 1$ state, the DLIF spectrum of the $\gamma 0^+ n + 1$ state is dominated by emissions to triplet states. However, emissions to singlet states are stronger in the $\gamma 0^+ n + 1$ DLIF spectrum as compared to the $\gamma 0^+ n - 1$ emission spectrum, which suggests that the $\gamma 0^+ n + 1$ has some singlet character. The emissions from the $C^1\Sigma^+(B\sigma\sigma^{-1}) v = 8$ state are dominated by emissions to final singlet states.

Finally, the $C^1\Sigma^+(B\sigma\sigma^{-1}) v = 7$ and $\gamma 0^+ v = n$ pair are considered. The perturbation analysis by Stewart *et al.*²⁶ indicate that these states have an energy separation of 9.4 cm^{-1} prior to their mutual repulsion. Eigenvectors from the perturbation analysis indicate nearly a 50:50 mixing of the states. This prediction arose from the DLIF spectra that showed both singlet and triplet bands with similar intensities. This 50:50 mixing prediction is also consistent with the lifetime measurements. The lifetime results give values of 27 ns for the $C^1\Sigma^+(B\sigma\sigma^{-1}) v = 6,8$ states and 44 ns for the $\gamma 0^+ v = n - 1, n + 1$ states. A 50:50 mixed, in the absence of interference effects, should exhibit a lifetime of 33 ns based on the weighted sum of decay rates. This is the average the values observed for the $C^1\Sigma^+(B\sigma\sigma^{-1}) v = 7$ and $\gamma 0^+ n$ states, confirming the 50:50 state mixing prediction.

From the above analysis, it is obvious that the $\gamma 0^+$ state is indeed a triplet state. The $\gamma 0^+$ state can be identified by considering the DLIF spectra along some help from *ab initio* calculations. Table 4.4, reproduced from Norman *et al.*⁸, lists the low-lying excited states of CaO with their electronic configuration and CaF parentage.

Table 4.4. Low-lying excited states of CaO with their electronic configuration and CaF parentage.

Nominal Electronic Configuration	States	CaF and NaO Parentage
$7\sigma^2 8\sigma^2 3\pi^3 9\sigma$	$A^1\Pi, a^3\Pi$	$X\sigma\pi^{-1}$
$7\sigma^2 8\sigma^2 3\pi^3 4\pi$	$c^3\Sigma^+, C^1\Sigma^+, D^1\Delta, d^3\Delta, E^1\Sigma^-, e^3\Sigma^-$	$A\pi\pi^{-1}$
$7\sigma^2 3\pi^4 8\sigma 4\pi$	$B^1\Pi, f^3\Pi$	$A\pi\sigma^{-1}$
$7\sigma^2 8\sigma^2 3\pi^3 10\sigma$	$F^1\Pi, g^3\Pi$	$B\sigma\pi^{-1}$
$7\sigma^2 3\pi^4 8\sigma 10\sigma$	$C^1\Sigma^+, h^3\Sigma^+$	$B\sigma\sigma^{-1}$
$7\sigma^2 3\pi^4 8\sigma 9\sigma$	$A^1\Sigma^+, b^3\Sigma^+$	$X\sigma\sigma^{-1}$

It was observed in this work that the $\gamma 0^+$ state perturbs the $C^1\Sigma^+(B\sigma\sigma^{-1})$ state and emits to the $a^3\Pi_{0+}(X\sigma\pi^{-1})$ state. Based on simply the omega value of $\Omega = 0^+$, the only triplet states from Table

4.4 that are candidates for $\gamma 0^+$ are the $f^3\Pi_{0+}(A\pi\sigma^{-1})$ and $g^3\Pi_{0+}(B\sigma\pi^{-1})$. For a one-photon process, only one quantum change in angular momentum is allowed. Emission from the $f^3\Pi_{0+}(A\pi\sigma^{-1})$ state to the $a^3\Pi_{0+}(X\sigma\pi^{-1})$ would require a change of two quanta of angular momentum and therefore disqualifies it from being the $\gamma 0^+$ state, as all emissions in this work are one-photon processes. Emission from the $g^3\Pi_{0+}(B\sigma\pi^{-1})$ state to the $a^3\Pi_{0+}(X\sigma\pi^{-1})$ state requires no change in angular momentum and therefore makes the $g^3\Pi_{0+}(B\sigma\pi^{-1})$ state a viable candidate for the $\gamma 0^+$ state. Also, the observed $\gamma 0^+$ vibrational interval is typical of π^{-1} configurations. It is therefore recommended that the $\gamma 0^+$ state be assigned as the $g^3\Pi_{0+}(B\sigma\pi^{-1})$ state.

As electronic states arising from the same electronic configurations have similar vibrational constants, the vibrational character of the $g^3\Pi_{0+}(B\sigma\pi^{-1})$ can be estimated from the vibrational character of the $F^1\Pi(B\sigma\pi^{-1})$ state. The $g^3\Pi_{0+}(B\sigma\pi^{-1})$ $\nu = 0$ energy can be estimated as well from singlet-triplet splitting of electronic states arising from π^{-1} configurations. The $F^1\Pi(B\sigma\pi^{-1})$ state has term energy and vibrational constants²⁶ of $T_{00} = 26794.8$, $\omega_e = 521.3$, and $\omega_e x_e = 2.59$ cm^{-1} . Table 4.5 lists the singlet-triplet energy splitting of various electronic configurations taken from Stewart *et al.*²⁶.

Table 4.5. Singlet-triplet energy splitting of various electronic configurations of CaO.

CaF and NaO Parentage	Singlet-Triplet States	ΔE (cm^{-1})
$X\sigma\pi^{-1}$	$A^1\Pi - a^3\Pi_1$	257
$A\pi\pi^{-1}$	$D^1\Delta - d^3\Delta_2$	-210
	$E^1\Sigma^- - e^3\Sigma^-$	-53

Under the assumption that the $F^1\Pi(B\sigma\pi^{-1})$ and $g^3\Pi_{0+}(B\sigma\pi^{-1})$ states have similar vibrational constants, the energy of the $g^3\Pi_{0+}(B\sigma\pi^{-1})$ $\nu = 0$ state can be determined. Stewart *et al.*²⁶ observed the vibrational intervals of the $g^3\Pi_{0+}(B\sigma\pi^{-1})$ $n - 1$ to n and n to $n + 1$ states to be 442.5 cm^{-1} and

475.7 cm^{-1} . To determine the energy of the unperturbed n state, the average of the two vibrational intervals above can be calculated, resulting in a value of 459.1 cm^{-1} . If one calculates the vibrational intervals of the $F^1\Pi(B\sigma\pi^{-1})$ using vibrational constants from Stewart *et al.*²⁶, it is apparent that the vibrational interval between the $F^1\Pi(B\sigma\pi^{-1})$ $\nu = 11$ and $\nu = 12$ states is 459.1 cm^{-1} . Therefore, a value of $n = 12$ can be assigned to the $g^3\Pi_{0+}(B\sigma\pi^{-1})$ state. One can then extrapolate to $g^3\Pi_{0+}(B\sigma\pi^{-1})$ $\nu = 0$ to obtain a term energy of $T_{00} = 26,644 \text{ cm}^{-1}$ which results in a singlet-triplet energy splitting of $\Delta E(F^1\Pi - g^3\Pi_{0+}) = 151 \text{ cm}^{-1}$. Using values of $n = 11, 13$ give unlikely values for the singlet-triplet splitting. To conclude, this analysis shows that the assignment of $\gamma 0^+$ as the $g^3\Pi_{0+}(B\sigma\sigma^{-1})$ is consistent with the atomic-ion-in-molecule model for CaO.

4.4 Chapter 4 References

1. Lagerqvist, A., *Arkiv For Fysik* **1954**, 8, 83-95.
2. Lagerqvist, A., Das Bandenspektrum des Calciumoxyds in dem violetten und ultravioletten Gebiet. *Die Naturwissenschaften* **1953**, 40 (9), 268-269.
3. Hultin, M.; Lagerqvist, A., An Infra-Red Band-System of Calcium Oxide. *Nature* **1950**, 166 (4213), 190-191.
4. Harrison, J. F.; Field, R. W.; Jarrold, C. C., Comparison of CaF, ZnF, CaO, and ZnO: Their Anions and Cations in Their Ground and Low-Lying Excited States. *ACS Symposium Series* **2002**, 828, 238-259.
5. Baldwin, D. P.; Norman, J. B.; Soltz, R. A.; Sur, A.; Field, R. W., The $e^3\Sigma^- - a^3\Pi(0, 0)$ and $E^1\Sigma^- - A^1\Pi(0, 0)$, (1, 1), and (2, 2) bands of CaO: Multistate deperturbation of the $e^3\Sigma^- (v = 0) \sim c^3\Sigma^+ (v = 1) \sim E^1\Sigma^- (v = 0)$ system. *Journal of Molecular Spectroscopy* **1990**, 139 (1), 39-67.
6. Baldwin, D. P.; Field, R. W., Dispersed laser fluorescence spectroscopy of the perturbation facilitated $B^1\Pi - b^3\Sigma^+(1, 1)$ band of CaO. *Journal of Molecular Spectroscopy* **1990**, 139 (1), 77-83.
7. Baldwin, D. P.; Field, R. W., The $F^1\Pi - A^1\Pi(0, 0)$ and $B^1\Pi - A^1\Pi(1, 0)$ Green-Band transitions of CaO. *Journal of Molecular Spectroscopy* **1990**, 139 (1), 68-76.
8. Norman, J. B.; Cross, K. J.; Schweda, H. S.; Polak, M.; Field, R. W., The CaO $c^3\Sigma^+ - a^3\Pi_i(0,0)$ band. *Molecular Physics* **1988**, 66 (1), 235-268.
9. Baldwin, D. P.; Field, R. W., The $C^1\Sigma^+ - A^1\Pi(0, 0)$ and (1, 1) bands of CaO. *Journal of Molecular Spectroscopy* **1989**, 133 (1), 90-95.

10. Marks, R. F.; Schweda, H. S.; Gottscho, R. A.; Field, R. W., The orange arc bands of CaO. Analysis of a $D, d^{1,3}\Delta-a^3\Pi$ system. *The Journal of Chemical Physics* **1982**, *76* (10), 4689-4691.
11. Marks, R. F.; Gottscho, R. A.; Field, R. W., The CaO $D, d^{1,3}\Delta-a^3\Pi$ System: Sub-Doppler Spectrum, Rotational Analysis, and Deperturbation. *Physica Scripta* **1982**, *25*, 312-328.
12. Field, R. W.; Capelle, G. A.; Jones, C. R., The $A^1\Pi-X^1\Sigma$ system of CaO. *Journal of Molecular Spectroscopy* **1975**, *54* (1), 156-159.
13. Field, R. W., Assignment of the lowest $^3\Pi$ and $^1\Pi$ states of CaO, SrO, and BaO. *The Journal of Chemical Physics* **1974**, *60* (6), 2400-2413.
14. Baldwin, D. P.; Hill, E. J.; Field, R. W., Electron affinity of O^- and diabatic CaO(g) integer charge potential curves. *Journal of the American Chemical Society* **1990**, *112* (25), 9156-9161.
15. Rice, S. F.; Martin, H.; Field, R. W., The electronic structure of the calcium monohalides. A ligand field approach. *The Journal of Chemical Physics* **1985**, *82* (11), 5023-5034.
16. Allison, J. N.; Cave, R. J.; Goddard, W. A., Alkali oxides. Analysis of bonding and explanation of the reversal in ordering of the $^2\Pi$ and $^2\Sigma$ states. *The Journal of Physical Chemistry* **1984**, *88* (6), 1262-1268.
17. Bauschlicher, C. W.; Yarkony, D. R., Electronic structure of CaO. I. *The Journal of Chemical Physics* **1978**, *68* (9), 3990-3997.
18. Diffenderfer, R. N.; Yarkony, D. R., The electronic structure of CaO. II. An MCSCF/CI treatment of the low-lying $^1\Sigma^+$ and $^1\Pi$ states. *The Journal of Chemical Physics* **1982**, *77* (11), 5573-5580.

19. Khalil, H.; Le Quéré, F.; Brites, V.; Léonard, C., Theoretical Study of the Rovibronic States of CaO. *Journal of Molecular Spectroscopy* **2012**, *271* (1), 1-9.
20. Khalil, H.; Brites, V.; Quéré, F. L.; Léonard, C., Ab initio study of the low-lying electronic states of the CaO molecule. *Chemical Physics* **2011**, *386* (1-3), 50-55.
21. Cheng, J.; Chen, H.; Zhu, X.; Cheng, X., Theoretical study of the ro-vibrational spectrum of CaO molecule in its two $X^1\Sigma^+$ and $A^1\Sigma^+$ states. *Journal of Molecular Structure* **2015**, *1084*, 122-127.
22. Yurchenko, S. N.; Blissett, A.; Asari, U.; Vasilios, M.; Hill, C.; Tennyson, J., ExoMol molecular line lists – XIII. The spectrum of CaO. *Monthly Notices of the Royal Astronomical Society* **2016**, *456* (4), 4524-4532.
23. Tennyson, J.; Yurchenko, S. N., ExoMol: molecular line lists for exoplanet and other atmospheres. *Monthly Notices of the Royal Astronomical Society* **2012**, *425* (1), 21-33.
24. Berezhnoy, A. A.; Borovička, J.; Santos, J.; Rivas-Silva, J. F.; Sandoval, L.; Stolyarov, A. V.; Palma, A., The CaO orange system in meteor spectra. *Planetary and Space Science* **2018**, *151*, 27-32.
25. Focsa, C.; Poclet, A.; Pinchemel, B.; Le Roy, R. J.; Bernath, P. F., Fourier Transform Spectroscopy of the $A^1\Pi-X^1\Sigma^+$ System of CaO. *Journal of Molecular Spectroscopy* **2000**, *203* (2), 330-338.
26. Stewart, J. T.; Sullivan, M. N.; Heaven, M. C., Near UV bands of jet-cooled CaO. *Journal of Molecular Spectroscopy* **2016**, *322*, 18-21.
27. Field, R. W., Discussion of CaO perturbations. 2016.

28. Western, C. M., PGOPHER: A program for simulating rotational, vibrational and electronic spectra. *Journal of Quantitative Spectroscopy and Radiative Transfer* **2017**, *186*, 221-242.
29. Leroy, R. J., LEVEL: A computer program for solving the radial Schrodinger equation for bound and quasibound levels. *Journal of Quantitative Spectroscopy and Radiative Transfer* **2017**, *186*, 167-178.

Chapter 5

Characterization of the Low-Lying States

of NdO and SmO and the Search for

NdO^+ and SmO^+

5.1 Introduction

5.1.1 The Chemi-ionization of Lanthanides

Recently, there has been interest in artificially increasing the atmospheric electron density for communication applications¹. The natural electron density in the atmosphere is largely produced from the ionization of chemical species by solar UV radiation. As both the number density of neutral chemical species and the solar UV flux are dependent on the atmospheric altitude and the time of day, the natural electron density fluctuates greatly. This fluctuation creates an issue for radio wave communications, as it causes rapid fluctuations known as scintillations² in both the phase and amplitude of the radio waves. Scintillations³ can result in reduced position accuracy and in extreme cases failure for radio wave receivers to lock onto signals. One proposed solution to remediate this issue is to artificially increase the electron density such that the total density is much greater than the natural fluctuations at altitude ranges of greater than 70 km. This would in effect establish a new electron density baseline without fluctuations, ensuring the uniform propagation of radio waves.

Currently, the chemi-ionization of lanthanide metals is being proposed as a chemical method to increase the atmospheric electron density. In this process, atomic lanthanide metals M react with readily abundant atmospheric atomic oxygen to produce the molecular oxide cation MO^+ , releasing a lone electron.



The thermodynamic pathway for the chemi-ionization process is shown in Figure 5.1, from which it can be seen that the heat of the reaction ΔH_r is equal to the difference of the dissociation and ionization energies of the neutral lanthanide oxide LnO . For this to be a thermodynamically favorable process, ΔH_r should be negative, indicating an exothermic reaction.

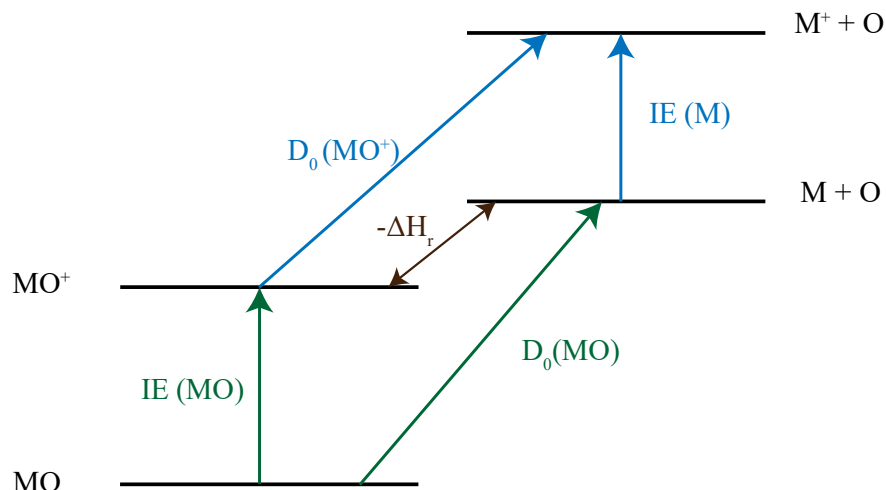


Figure 5.1. Thermodynamic pathway for the chemi-ionization of lanthanide M .

Neodymium (Nd) and samarium (Sm) are currently the two lanthanide candidates for the chemi-ionization process. Laboratory determinations of the bond dissociation and ionization energies of neutral lanthanide oxides found that this reaction is highly exothermic^{4,5} ($-\Delta H_r = 1.76$ eV) for Nd while being almost thermodynamically neutral⁶ ($-\Delta H_r = -0.0044$ eV) for Sm. Although it would not be thermodynamically favorable to employ Sm for the chemi-ionization process, Sm remains a candidate due to its relatively low vaporization temperature.

The United States Air Force (USAF) has conducted rocket launches^{7,8}, where 5 kg of the desired lanthanide metal was vaporized and released by thermite explosions into the atmosphere at altitudes of 170 and 180 km, resulting in the production of a “space cloud”. In the case of Sm, a blue-white quasi spherical cloud was observed⁹ by eye which then evolved into a partially reddened cloud after a time duration of one minute. To kinetically and spectroscopically characterize the space cloud, a spectrograph coupled with an electron-multiplying CCD imager was used to observe the cloud spectral emissions as a function of wavelength and time. The spectral analysis revealed two major regions of transitions: one from 400-580 nm with linewidths typical of atomic transitions and another from 600-700 nm with broader features. It was therefore

inferred that the blue character of the cloud was produced by atomic species while molecular species were responsible for the reddening of the cloud. One issue that arose in the cloud analysis was that the total electron density observed was orders of magnitude below what was expected⁶. Kinetic models fit to the observed electron density indicated that the Sm vaporization efficiency was less than 5%. The models also predicted that there should be a substantial SmO⁺ population but this was unverifiable by the spectroscopic data. It remains unclear as to whether the molecular species responsible for the red emissions was the neutral SmO or its cation counterpart due to a lack of spectroscopic characterization of both these molecules.

The space cloud produced by the Nd launch was much less characterized. Based on the emission spectroscopy and the drift of the cloud, it was assumed that the primary product in the cloud was NdO. This result was surprising since, as the chemi-ionization of Nd is highly exothermic, it is expected that NdO⁺ should be readily produced. To investigate the supposed lack of NdO⁺ production, Ard *et al.*¹⁰ investigated the chemi-ionization reactions of Nd and Sm in a flow-tube apparatus. They found that the chemi-ionization rate constant for Nd was on the order of $10^{-10} \text{ cm}^3 \text{ s}^{-1}$ and was consistent with the hard-sphere collision frequency, indicating that the Nd should chemi-ionize on all or nearly all collisions. To truly confirm whether NdO⁺ is being produced in the space cloud, spectroscopic characterization of both NdO and NdO⁺ is needed.

The primary goal of this work is to characterize the electronic structure of NdO, SmO, and their respective cations. Providing spectroscopic data on these molecules will allow the USAF to confirm or deny whether the chemi-ionization process is occurring in the rocket launch space clouds. The following sections will describe previous efforts to spectroscopically characterize the electronic structure of NdO/NdO⁺ and SmO/SmO⁺.

5.1.2 Previous Studies of NdO and NdO⁺

The electronic structure of NdO has been experimentally characterized primarily through absorption and laser-induced fluorescence spectroscopy. Kaledin *et al.*¹¹ generated gas-phase NdO by heating N₂O₃ in a furnace to high temperatures of 2000-2200° C. Absorption and emission spectra were recorded from 500 nm to 1.1 μm. Around 400 bands were observed and 65 were categorized into transitions originating from ten different electronic upper states. Shenyavskaya *et al.*¹² expanded Kaledin's analysis of NdO by using near-infrared Fourier transform spectroscopy to obtain rotationally well-resolved emission spectra from 790 nm to 1.33 μm. Rotational constants for bands previously observed by Kaledin were reevaluated and term energies for new transitions were determined. Four low-lying excited states were observed through transitions with common upper states and vibrational intervals were determined for the ground electronic state X4, as well as the (1)3 state. This work clearly established the ground state as an $\Omega = 4$ state.

The primary characterization of the low-lying states of NdO comes from Linton and coworkers^{13, 14}. In these works, low-lying states were characterized through laser-induced fluorescence by exciting single rotation lines of eight strong emission bands with either an argon ion or cw ring dye laser. The resulting emissions were recorded with a high-resolution Fourier transform spectrometer. Emissions to the ground X4 and nine low-lying states were observed with four low-lying states being observed for the first time. Term energies, rotational constants, and, in some cases, vibrational intervals were determined for these states. Finally, magnetic *g*-factors and electric dipole moments¹⁵ for the ground X4 and [16.7]3 state have been determined through Stark and Zeeman splitting measurements. Recently, Babin *et al.*¹⁶ employed slow photoelectron velocity map-imaging spectroscopy (SEVI) to characterize the low-lying states of

NdO and NdO⁻ by producing cryo-cooled NdO⁻ molecules which then underwent photo detachment. Detached electrons were focused onto microchannel plates coupled to a phosphor screen and a CCD camera was used to capture electron images. The electron binding energies (eBE) were determined by subtracting the electron kinetic energy from the images from the photo detachment energy. The electron affinity of NdO was determined to be 1.0091(7) eV and transitions to vibrations states of $\nu = 0-2$ of the X4, (1)5, and (2)4 electronic states of NdO were observed.

The electronic structure of NdO can be well described employing a ligand-field model (LFT). As mentioned in Chapter 2, LFT is an ionic bonding model which describes the molecular energies of lanthanide- and actinide-containing molecules in terms of an ionic metal center, whose atomic energies are perturbed by the field of the ligand. Justification for this model for lanthanides arises from the compact nature of the $4f$ orbitals, resulting in an electron localization on the metal center. It has been established^{11, 12, 15, 17} that the ground X4 state of NdO arises from a Nd²⁺($4f^3 6s$)O²⁻($2p^6$) electronic configuration. The electronic states can be described in terms of a $j-j$ spin-orbit coupling scheme. The lowest energy state arising from the $4f^3$ core will have a total angular momentum of $J_c = 4.5$. This angular momentum will then couple with the $6s$ spin angular momentum of $s = 1/2$ to produce values of $J_a = 4$ and 5 . The O²⁻ ligand field will then split the values of J_a into their unsigned projections Ω on the internuclear axis with Ω varying from 0 to J_a in descending order. This results in an electronic ground state of $\Omega = 4$ which has been experimentally confirmed^{11, 12, 15, 17}. It quickly becomes evident that the presence of multiple f electrons results in a high density of low-lying electronic states, as the f^3s configuration alone¹³ gives rise to 56 electronic states under 1 eV. Due to this high-density of states, electronic states are denoted as $(i)\Omega$, where the index i refers to the state with the specified

Ω value in ascending order. For example, the (2)4 electronic state is the second lowest state with $\Omega = 4$. For states higher in energy that have not been well characterized, the notation $[10^{-3} T_0]\Omega$ is employed, where T_0 is the term energy in cm^{-1} . As another example, the [16.7]3 state well characterized by Kaledin *et al.*¹¹ and Linton *et al.*¹³, is an $\Omega = 3$ state with a term energy of 16740 cm^{-1} .

In terms of previous computational efforts, Carrette *et al.*¹⁷ as well Kaledin¹⁸ have characterized the electronic structure of NdO using a LFT model. Carrette *et al.* determined the energies of low-lying states for lanthanide oxides arising from lanthanide $4f^N$, $4f^{N-1}5d$, $4f^{N-1}6s$, and $4f^{N-1}6p$ electronic configurations, establishing that the $4f^{N-1}6s$ configuration was responsible for the electronic ground states for the lanthanide oxides, except EuO and YbO. Kaledin expanded on Carrette's work by calculating the term energies and leading electron configurations of electronic states in NdO up to 3 eV, finding that the LFT term energies agreed well with experimental data. Finally, Allouche *et al.*¹⁹ conducted *ab initio* calculations, employing complete active-space self-consistent field multi-reference configuration (CASSCF/MRCI) methods to determine the term energies as well as molecular constants for 54 electronic states under 1 eV. They found that for nine electronic states, the calculated molecular constants agreed well with experimental data.

The characterization of the electronic structure of NdO^+ has been much less extensive. VanGundy *et al.*⁵ generated NdO through laser ablation and supersonic expansion techniques and two-color photoionization spectroscopy was employed to obtain the ionization energy NdO and vibrationally characterize low-lying states of NdO^+ . Photoionization efficiency (PIE) spectroscopy was employed to obtain the ionization energy of NdO, which was then refined by

pulsed-field ionization zero electron kinetic energy (PFI-ZEKE) spectroscopy measurements to the current value of 5.5083(2) eV.

Electronic structure calculations^{5, 20} have predicted a ground state electronic configuration of $\text{Nd}^{3+}(4f^3)\text{O}^{2-}(2p^6)$ with the lowest angular momentum value of $J_a = 4.5$, resulting in Ω states from $\Omega = 4.5-0.5$. Krauss *et al.*²⁰ predicted that the energy spread of the $\text{Nd}^{3+}(4f^3, J_a = 4.5)\text{O}^{2-}$ states should be 904 cm^{-1} , much less than the free ion ${}^4\text{I}_{5.5}-{}^4\text{I}_{4.5}$ atomic spin-orbit splitting of 1987 cm^{-1} , indicating that the ligand field splitting is much smaller than the atomic ion spin-orbit coupling. VanGundy *et al.* investigated the spin-orbit splitting of NdO^+ by employing PFI-ZEKE spectroscopy to observe the vibrational energies of the NdO^+ ground X4.5 state from $v^+ = 0-5$ as well as several vibration states of seven low-lying excited states. Vibrational constants of $\omega_e = 892.4(15)$ and $\omega_{exe} = 1.3(2) \text{ cm}^{-1}$ were determined for the ground X4.5 state and also for five of the seven observed electronic states. It was concluded that since the electronic states all had similar ω_e values, they all originated from the $\text{Nd}^{3+}(4f^3)\text{O}^{2-}(2p^6)$ configuration. The energy difference between the X4.5 and the (1)5.5 states was found to be 1840 cm^{-1} , which is quite similar to the atomic ${}^4\text{I}_{5.5}-{}^4\text{I}_{4.5}$ spin orbit split of 1987 cm^{-1} , indicating spin-orbit conservation.

To date, there has been no characterization of NdO^+ at molecular energies above 8000 cm^{-1} . Observation of both NdO and NdO^+ transitions in the visible spectral range is needed to confirm the production of molecular ions in the USAF space cloud. Further characterization of NdO will also allow comparisons to LFT calculations and provide benchmarks for computational model improvements.

5.1.3 Previous Studies of SmO and SmO^+

The electronic structure of SmO has been primarily characterized through laser-induced fluorescence and dispersed fluorescence spectroscopic techniques. Initial spectroscopic

measurements were performed by Hannigan²¹, in which SmO was produced by vaporizing Sm in an oven at high temperatures (1000 °C) and crossing the vaporized Sm beam with SO₂.

Fluorescence was induced with a N₂ pumped tunable dye laser and was detected at excitation wavelengths of 571-664 nm. Molecular bands from 647-654 nm were observed but were extremely broadened due to the high-temperature production conditions. Fluorescence lifetimes were recorded but the only rotational information obtainable was whether the rotational bandheads were blue- or red-degraded.

After Hannigan, the primary spectroscopic characterization of SmO was performed by Linton and co-workers²²⁻²⁵. In these studies, SmO was generated in a Broida oven by reacting entrained samarium vapor in argon with oxygen. Fluorescence was induced in the SmO flame by a ring dye laser and detected through a monochromator. Dispersed fluorescence spectra were recorded by exciting the Q branch of each band and dispersing the fluorescence with a monochromator. In the earliest study, emissions to the electronic ground state as well as ten low-lying excited states were observed²², with electronic energies agreeing well with ligand field theory calculations¹⁷. The ground electronic state was assigned as an $\Omega = 0^-$ state and the equilibrium rotational constant B_e as well as the vibration interval $\Delta G_{1/2}$ were determined for the ground $X0^-$ state and a couple of low-lying excited states. High-resolution studies^{23, 24} expanded the number of observed transitions, resolving the isotopic structure of the bands. Term energies, rotational and A -doubling constants for the ground $X0^-$ state, twelve low-lying states, and eight upper states were determined for seven isotopes of samarium. To further characterize the ground $X0^-$ state, the [16.6]1- $X0^-$ 0-0 transition was used to determine²⁵ the permanent dipole moments of the $X0^-$ and [16.6]1 states in both ¹⁵²SmO and ¹⁵⁴SmO. In this study, SmO was produced via laser ablation and supersonic expansion techniques and the Stark shifts of the R(0) and R(1) lines

were measured in electric fields up to 7.9 kV/cm. Ground state dipole moments of 3.517(20) and 3.451(28) D were determined for the ^{152}SmO and ^{154}SmO isotopologues.

In addition to the studies of Linton and coworkers, properties of SmO such as the electron affinity and ionization energy have been investigated in relation to the chemi-ionization of lanthanide metals. Weichmen *et al.*²⁶ employed slow photoelectron velocity map imaging spectroscopy to determine an electronic affinity of SmO of 1.0581(11) eV. Using similar techniques to the study by Babin *et al.*¹⁶, transitions between the SmO⁻ anion and neutral SmO were observed allowing term energies of the ground X0⁻ and several low-lying states to be determined with the term energies in good agreement with previous works. Cox *et al.*⁶ employed photoionization efficiency (PIE) and pulsed-field ionization zero electron kinetic energy (PFI-ZEKE) spectroscopy methods to determine the ionization energy of SmO. Creating SmO through laser ablation and supersonic expansion techniques, SmO was excited with a fixed energy photon via the [16.6]1-X0⁻ origin band after which a tunable photon was used to ionize the molecule. The ionization energy determinations from both the PIE and PFI-ZEKE measurements were in an agreement with each other and a value of 5.7427(6) eV was reported.

The electronic structure of SmO can be predicted by a ligand field theory model. The ground state of SmO will arise from the $\text{Sm}^{2+}(4f^56s)\text{O}^{2-}(2p^6)$ electronic configuration. The lowest energy state from the f^5 core will have an angular momentum of $J_c = 2.5$, which will then couple to the spin of the s electron to produce J_a values of 2 and 3, with $J_a = 2$ lying lower in energy. The O^{2-} ligand field will then split the J_a values into Ω projections from $\Omega = 0$ - J_a in ascending order. This results in a ground state Ω value of 0. The symmetry of the $\Omega = 0$ state can be determined²⁷ from the following sum

$$J_1 + J_2 + \sum l_1 + \sum l_2 \quad (5.2)$$

where J_i and l_i are the total angular momentum and orbital angular momentum of each electron in the $J_a = 2$ state. The symmetry of the ground state angular momentum will be reflective of the odd or even character of the sum in (5.2). For the $J_a = 2$ state in SmO, the values of J and Σl for the $\text{Sm}^{2+}(4f^5 6s)$ configuration will be 2 and 15 and the values of J and Σl for the closed shell O^{2-} configuration will both be zero. This gives a total sum of 17 which is odd, resulting in a $\Omega = 0^-$ ground state for SmO. This has been confirmed by experimental studies²²⁻²⁵. As with NdO, the electronic structure of SmO is expected to be quite complicated due to the high density of states, as just the $f^5 s$ configuration alone gives rise to 72 electronic states. As with other lanthanide oxides, due to the density of states, states are either labeled as $[10^{-3} T_0]\Omega$ or $(i)\Omega$, where T_0 is the term energy in wavenumbers and i is an index referring to an energy state with the specified Ω value in ascending order.

While there have been some computational efforts to describe the electronic structure of SmO, they are less numerous than those for NdO, due to computational difficulty scaling with the number of $4f$ electrons and relativistic effects. Field²⁸ used a ligand field treatment to calculate the vibrational frequencies and omega values for the ground electronic states of lanthanide oxides but erroneously predicted a value of $\Omega = 2$ for the ground state of SmO. Dulick *et al.*²⁹ calculated lanthanide oxide electronic states under $10,000 \text{ cm}^{-1}$ arising from a $4f^N 6s$ lanthanide configuration and established an $\Omega = 0^-$ ground state for SmO. Carette¹⁷ *et al.* expanded the ligand field analysis and determined the energies of low-lying states for lanthanide oxides arising from lanthanide $4f^N$, $4f^{N-1}5d$, $4f^{N-1}6s$, and $4f^{N-1}6p$ electronic configurations, again confirming the $\Omega = 0^-$ character of the SmO electronic ground state. More recently, Paulovic *et al.*³⁰, in order to propose a likely mechanism for the chemi-ionization of Sm, calculated potential energy curves of states of SmO arising from septet spin states using multiconfigurational second

order perturbation theory (CASPT2). Molecular constants for the ${}^7\Delta$ ground state were found to agree well with experimental values²². However, Paulovic *et al.* found that ground spin-orbit state of SmO was doubly degenerate, contradicting previous $\Omega = 0$ assignments. Definitive assignments of Ω values were not able to be made due to very small separations between the spin-orbit states that were beyond the capabilities of the calculations. Weichman *et al.*²⁶ also performed CASPT2 calculations on SmO and SmO⁻ to complement their cryo-SEVI experimental data. They found that their computational results agreed with the ground and low-lying state energies from the SEVI results.

Both experimental and computational studies on the characterization of the electronic structure of the SmO⁺ are few to non-existent. The bond dissociation energy D_0 of SmO⁺ was determined by Cox *et al.*⁶ using a guided ion beam tandem mass spectrometer (GIBMS). In these experiments, Sm⁺ and SmO⁺ ions were created in a discharge flow tube^{31,32} and directed into a static gas cell, where they were reacted with an oxygen-containing gas. After collision, the gas products were focused through a mass filter and detected. Reaction cross-sections were calculated from product ion intensities relative to reactant ion intensities. The collision cross section as a function of the ion kinetic energy was fit to a model from which the bond energy was determined. For SmO⁺, a bond energy of 5.72(7) eV was obtained.

According to ligand field theory, the ground state of SmO⁺ should arise from a Sm^{3+(4f⁵)} O^{2-(2p⁶)} electronic configuration and should have a Russel-Sanders notation of ${}^6\Gamma$. Paulovic *et al.*³⁰ have used CASPT2 theory to calculate the potential energy curve for the ground ${}^6\Gamma$ state, as well as molecular parameters of $r_e = 1.7414 \text{ \AA}$, $D_0 = 5.74 \text{ eV}$, and $\omega_e = 781 \text{ cm}^{-1}$. The dissociation energy D_0 calculated agrees well with the experimental GIBMS results⁶.

Unfortunately, as there is no spectroscopic data available, the calculated equilibrium bond length and vibrational interval of the SmO^+ ground state cannot be compared to literature values.

To confirm the production of SmO^+ in the AF space clouds, spectroscopic characterization of both SmO and SmO^+ is needed. Little characterization of SmO at wavelengths below 640 nm exists and there is no spectroscopic characterization of SmO^+ in the visible region.

5.2 Preliminary NdO Results

Rotationally-resolved LIF spectra of NdO were obtained in the wavelength ranges of 480-525 nm and 550-665 nm. Figure 5.2 shows the rotational structure of a band centered at 16167 cm^{-1} assigned as the $[16.17]4-X4 v'' = 0$ transition with a rotational temperature of 8K. Typically, rotational temperatures of 8-20K were observed for the jet-cooled NdO.

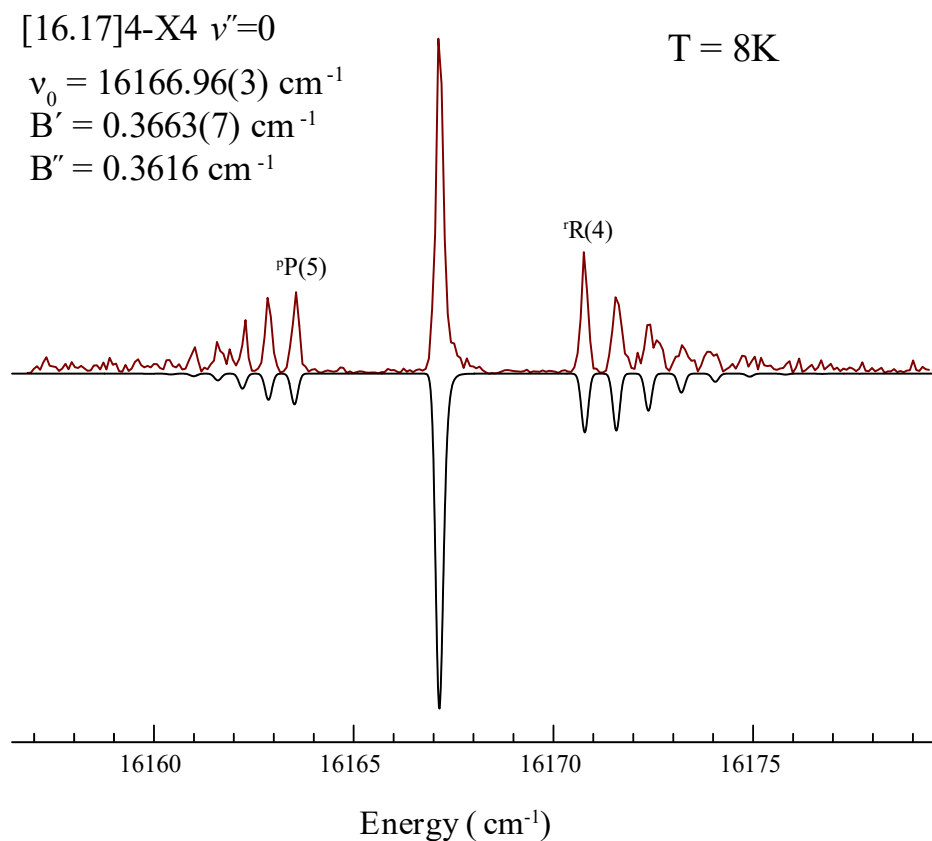


Figure 5.2. Rotationally-resolved LIF spectrum of the NdO $[16.17]4-X4 v'' = 0$ transition.

In Figure 5.2, the downward trace is a theoretical simulation generated by PGOHPER³³. Upper and lower states were treated as Hund's case (c) and rotational energies were fitted to

$$E_v(J) = B_v[J(J + 1) - \Omega^2] \quad (5.3)$$

where Ω is the total angular momentum projection on the internuclear axis. In Figure 5.2, large gaps between the Q and the P/R branches can be observed, indicative of upper and lower states with high Ω values. It was found in the fitting process that many observed bands did not originate from the X4 $v'' = 0$ ground state but from low-lying excited states, a result of possible inefficient cooling of electronic and vibrational energy levels. Because of the high-density of these low-lying excited states, fitting the rotationally resolved excitation spectra alone can be a challenge if the lower energy state is not known. In this work, transitions were assigned by first determining the $\Delta\Omega$ value using both the rotational branches' relative intensities and the first P and R branch line. Typically, the most intense rotational branch is indicative of the $\Delta\Omega$ value. For example, in $\Delta\Omega = 0$ transitions, the Q branch has a much higher intensity than the P/R branches whereas in $\Delta\Omega = \pm 1$ transitions, either the R or P branch has the highest intensity. Using Figure 5.2. as an example, it can therefore be inferred that the transition centered at $16,167 \text{ cm}^{-1}$ is a $\Delta\Omega = 0$ transition due to the high intensity of the Q-branch. This, however, is not a fool-proof method as signal fluctuations produced by laser ablating different surfaces of the rod can alter the relative intensities of branch lines. Therefore, in addition to the relative intensities of the rotational branches, the gaps between the Q branch and the P/R branches were also used to determine the $\Delta\Omega$ value of the transition. For a given Ω , the rotational quantum number J must be $J \geq \Omega$. This results in the absence of low J transitions in states with $\Omega > 0$. In Figure 5.2. it can be noted that the first R and P lines are R(4) and P(5) indicating a 4-4 $\Omega' - \Omega''$ transition.

After the $\Delta\Omega$ value for a branch was determined, the dispersed fluorescence spectrum for that band was then used to determine the vibronic identity of the lower state. Dispersed fluorescence spectra were acquired by exciting the most intense rotational feature of the transition and then recorded the emission wavelengths through a monochromator. Figure 5.3 shows the DLIF spectrum for the band at $16,167\text{ cm}^{-1}$ using an energy scale relative to the excitation energy. Emissions have been assigned with their vibronic states, using energy values from Linton *et al.*¹³ as a reference.

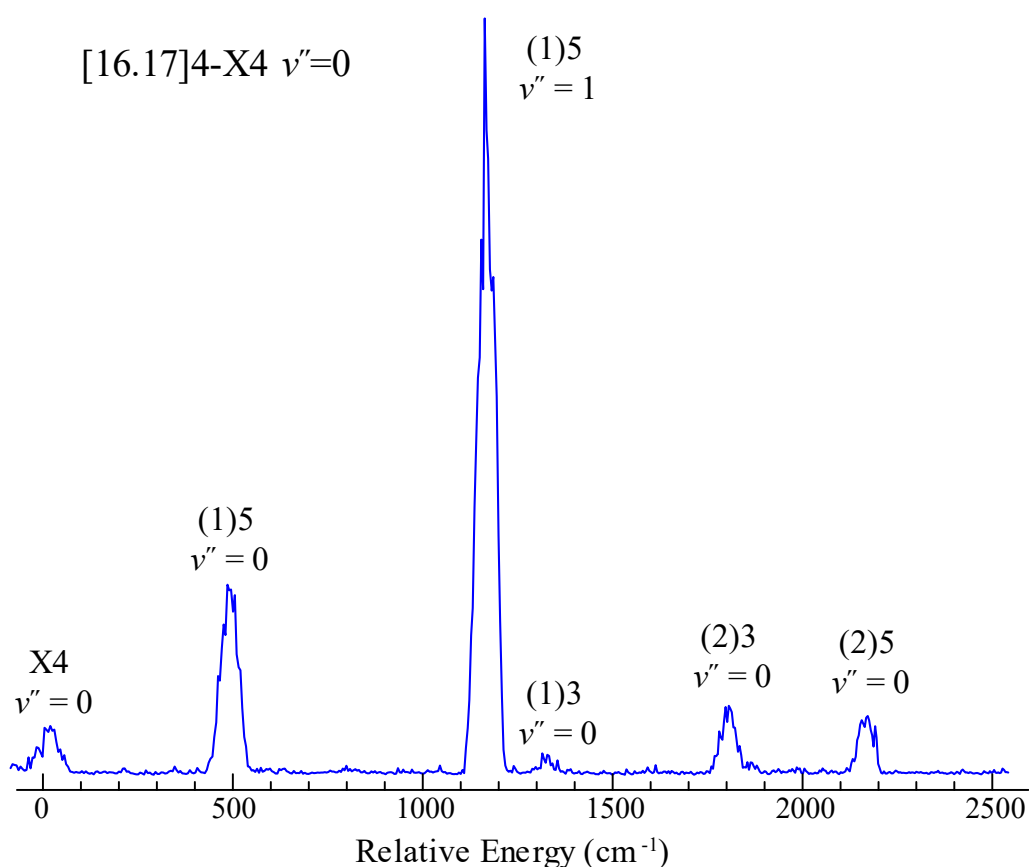


Figure 5.3. Dispersed fluorescence spectrum induced by excitation of the NdO [16.17]4-X4 $v'' = 0$ transition. Emissions are assigned with the vibronic identities.

It can be seen from Figure 5.3. that emissions with Ω values of 3, 4, and 5 are observed, indicative of only a $\Omega' = 4$ state. As the $\Delta\Omega$ value from the LIF spectrum was determined to be a

value of 0, the DLIF spectrum assigns this transition as a 4-4 Ω' - Ω'' transition. Furthermore, it can be seen from Figure 5.3. that there are no emissions at energies below that of the excitation energy, further indicating that this transition originates on the ground vibronic X4 $v'' = 0$ state and resulting in the assignment of [16.17]4-X4 $v'' = 0$.

Once the lower state identity is confirmed, lower state molecular constant values from Linton *et al.*¹³ are fixed in the theoretical simulation and upper state parameters are determined by least squares fitting. The results for 15 rotationally-resolved bands are shown in Table 5.1. Three bands centered at 15152 cm^{-1} , 15925 cm^{-1} , and 16737 cm^{-1} were previously characterized by Kaledin *et al.*¹¹ and denoted by their upper state notation of [VIII] and [X].

Table 5.1. Molecular constants obtained from fitting results of rotationally-resolved NdO LIF bands.

Transition	ν_0 (cm^{-1})	B' (cm^{-1})	B'' (cm^{-1})	Avg Residual (cm^{-1})	τ (ns)
[VIII]5-X4 0-0	15152.82(2)	0.3581(1)	0.3616	0.065	59(3)
[VIII]5-X4 1-0	15924.77(2)	0.3549(4)	0.3616	0.074	55(8)
[17.22]2-(1)3 $v'' = 0$	16068.56(2)	0.3744(2)	0.3520	0.027	88(6)
[16.17]4-X4 $v'' = 0$	16166.96(3)	0.3663(7)	0.3616	0.033	34(2)
[18.66]5-(2)4 $v'' = 1$	16245.53(2)	0.3739(1)	0.3496	0.047	45(1)
[X]3-X4 0-0	16737.50(2)	0.3401(1)	0.3616	0.065	32(1)
[18.07]4-(1)5 ($n+1$)-1	17541.54(1)	0.3526(2)	0.3606	0.020	43(5)
[18.07]4-(1)5 $n-0$	17601.13(1)	0.35448(9)	0.3621	0.048	25.4(1)
[18.08]4-X4 $v'' = 0$	18075.48(2)	0.3544(2)	0.3616	0.036	33.6(1)
[18.2]3-X4 $v'' = 0$	18174.72(1)	0.3781(2)	0.3616	0.028	151(22)
[19.29]5-X4 $v'' = 0$	19287.92(5)	0.3758(6)	0.3616	0.084	50(2)
[22.03]3-X4 $v'' = 2$	20379.03(2)	0.35268(7)	0.3588	0.046	46(1)
[22.44]4-X4 $v'' = 2$	20782.55(3)	0.3365(2)	0.3588	0.088	78(2)
[22.44]4-X4 $v'' = 2$	20783.10(2)	0.3393(5)	0.3588	0.023	26(2)
[22.01]3-(1)3 $v'' = 0$	20852.37(4)	0.3370(5)	0.352	0.069	115(3)

Isotopic splitting of rotational lines was partially resolved in one intense band centered at 19719 cm^{-1} , shown in Figure 5.4.

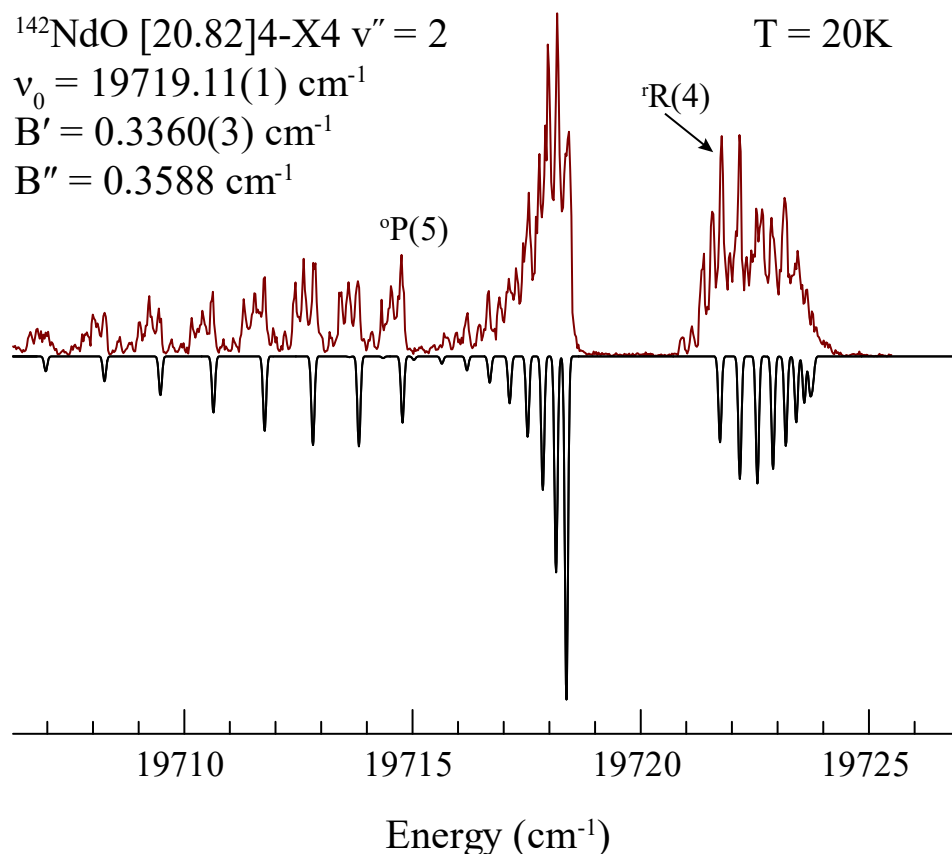


Figure 5.4. Rotationally fit of the ^{142}NdO isotope in the [20.82]4-X4 $v'' = 2$ transition.

The isotopic splitting is most clearly seen in the P branch, where each rotational feature splits into three distinct lines. The four most prominent isotopologues of NdO are the ^{142}NdO , ^{144}NdO , ^{146}NdO , and ^{143}NdO isotopes, with relative abundances of 0.272, 0.234, 0.172, and 0.122. Based on the natural abundances, the rotational line splitting in Figure 5.4 was assigned to the ^{142}NdO , ^{144}NdO , and ^{146}NdO isotopologues. The value for the X4 $v'' = 2$ state was taken from Linton *et al.*¹³ and was fixed in the rotational fits. The resulting molecular parameters for the isotopologues are listed in Table 5.2.

Table 5.2. Fitting results for the isotopically resolved rotational fit of the NdO [20.82]4-X4 $\nu'' = 2$ transition.

Isotopologue	ν_0 (cm ⁻¹)	B' (cm ⁻¹)	B'' (cm ⁻¹)	Avg Residual (cm ⁻¹)	τ (ns)
¹⁴² NdO	19719.11(1)	0.3360(3)	0.3588	0.0246	56(2)
¹⁴⁴ NdO	19718.91(1)	0.3356(3)		0.0267	
¹⁴⁶ NdO	19718.73(2)	0.3342(4)		0.0326	

As mentioned previously, dispersed fluorescence for the NdO bands were obtained by parking the dye laser on the most intense rotational feature and recording emissions from 400-900 nm. DLIF spectra were collected for a two-fold purpose: for assisting in band identification and for characterizing the vibronic structure of low-lying excited states. Figures 5.5 and 5.6 show the dispersed fluorescence spectra for the excitation bands listed in Table 5.1 and 5.2.

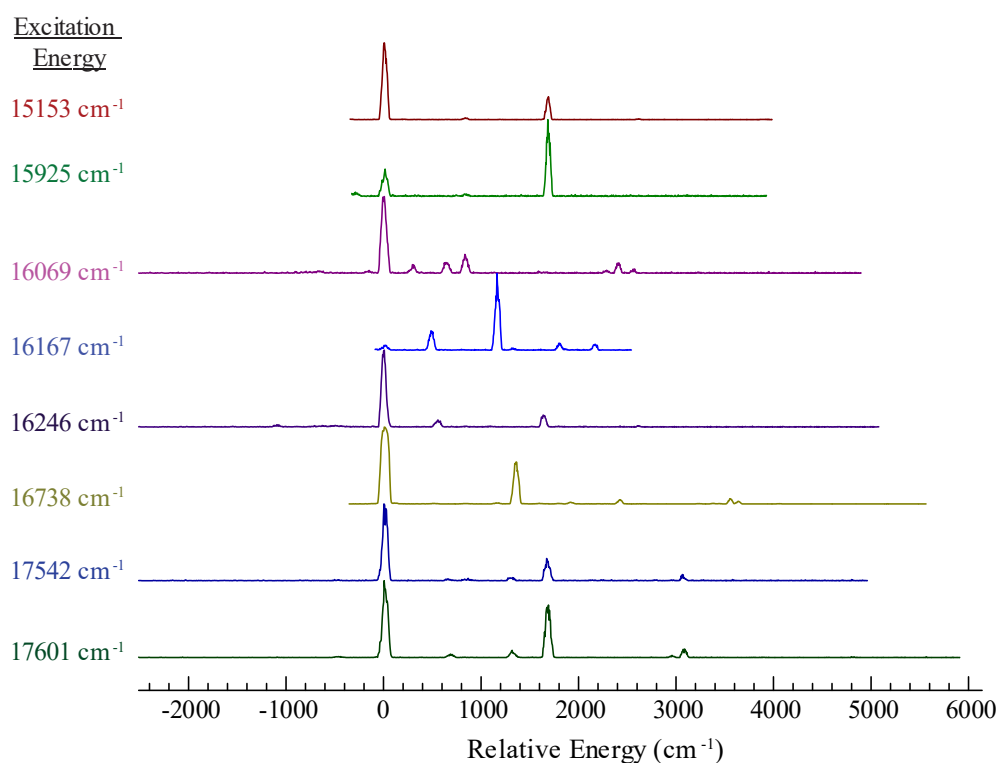


Figure 5.5. Dispersed fluorescence spectra of NdO bands at excitation energies from 15,153 cm⁻¹ to 17,601 cm⁻¹.

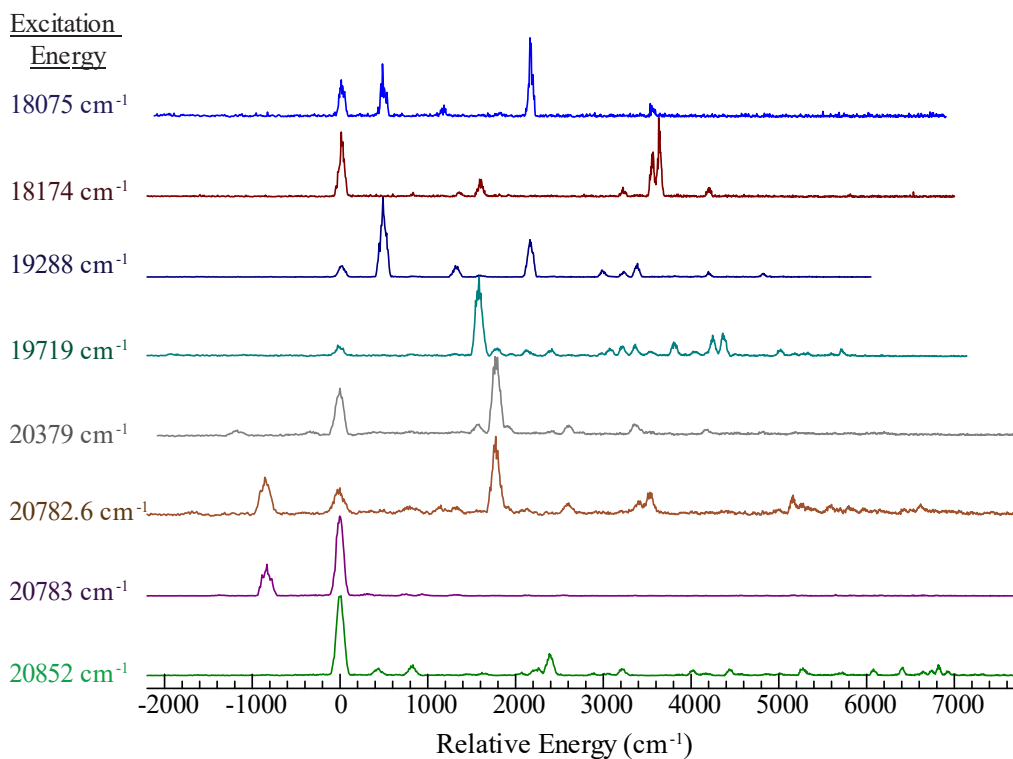


Figure 5.6. Dispersed fluorescence spectra of NdO bands at excitation energies from 18,075 cm^{-1} to 20,852 cm^{-1} .

In the DLIF spectra of the 16 SmO bands, emissions down to the X4, (1)5, (1)2, (2)2, (1)3, (2)4, (2)3, and (2)5 states were observed. Vibrational progressions were observed in all the states except the (1)2 state, in which just the $\nu = 0$ state was observed. For the (1)5 state, the $\nu = 0$ and 1 states were observed, allowing a $\Delta G_{1/2}$ determination of 831 cm^{-1} . In the other states, vibrational levels up to $\nu = 5$ were observed, allowing determining of ω_e for these electronic states. Figure 5.7 shows a plot of all the observed ground and low-lying vibronic levels as a function of $\nu + 0.5$.

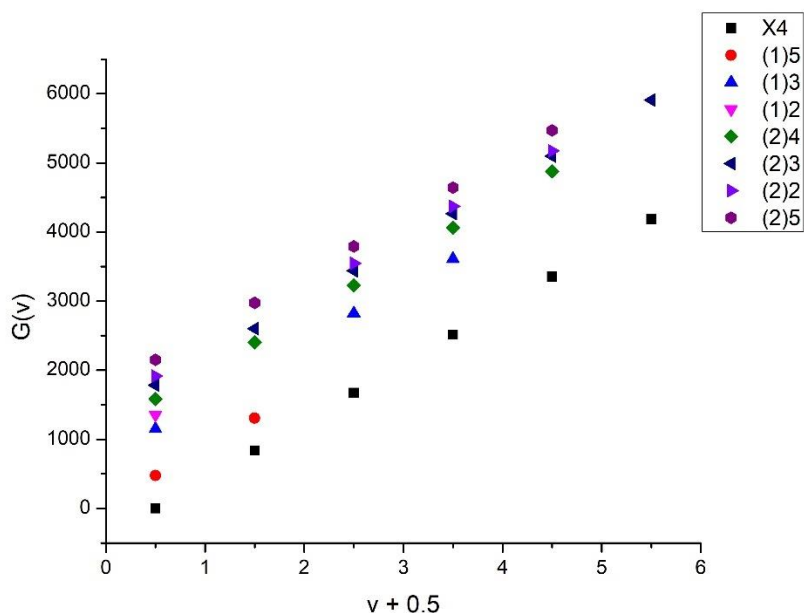


Figure 5.7. NdO vibronic energies of the electronic ground and low-lying states determined from the DLIF spectra, plotted as a function of $\nu + 0.5$.

Vibrational energies were then fit to the simple Morse expression in Equation 3.4 and ω_e was determined from the fits. An attempt was made to include the anharmonicity parameter $\omega_e x_e$ in the fits by fitting the vibrational parameters to a quadratic function in $\nu + 0.5$ but this resulting in $\omega_e x_e$ values with errors comparable in magnitude to the values themselves. Therefore, the final fitting results, which are listed in Table 5.3 only include the ω_e parameter.

Table 5.3. Vibrational parameter ω_e for the electronic ground X4 and low-lying states of NdO determined from dispersed fluorescence spectra.

(M) Ω	ω_e (cm ⁻¹)	ν states used in fit
X4	838(1)	0-5
(1)3	822(8)	0-3 ^b
(2)4	825(2)	0-4
(2)3	827(2)	0-5
(2)2	815(2)	0, 2-4
(2)5	831(3)	0-4

It should be noted that while the $(1)3 \nu = 1$ state was not observed in any of the DLIF spectra, the value of 1980.3 cm^{-1} from Linton *et al.*¹³ was included to improve the fit.

Lifetimes of the upper states of the observed transitions were determined by recording the fluorescence lifetime of the transition. All decay curves exhibited single-exponential behavior and the lifetime was determined by fitting to a single exponential decay. The resulting lifetimes for the transitions are listed in Tables 5.1 and 5.2. Measurements of the fluorescence decay were taken in triplicate and the errors reported in Tables 5.1 and 5.2 are the standard deviations of the three lifetime measurements.

5.3 NdO⁺ Results

5.3.1. Search for NdO⁺ LIF

An ArF (193 nm, 450 mJ) excimer laser was used to photoionize NdO at a time interval of $1.5 \mu\text{s}$ before the probe dye laser. Initially, the search for NdO⁺ LIF bands was conducted in the same spectral ranges in which NdO transitions were observed. Two spectral regions of 595-600 nm and 600-602 nm, in which Kaledin¹¹ observed strong NdO transitions, were employed for initial searches but no excimer-dependent transitions were observed. It was then speculated that upon ionization, the ground state electronic configuration of $\text{Nd}^{3+}(4f^3)\text{O}^{2-}$ restricts electronic orbital transitions of $f \leftrightarrow f$ and $f \leftrightarrow d$ types. Typically, $f \leftrightarrow f$ transitions for lanthanides are rather weak and are located in the infrared region, which is out of the spectral scope of this project. The stronger $f \leftrightarrow d$ transitions, however, are theorized to occur in the UV spectral range. It was also considered that green emissions were observed in the Nd space clouds. The NdO⁺ investigation spectra range was therefore shifted to blue and green wavelengths. To avoid fluorescence from the neutral NdO, dispersed fluorescence spectra were taken, recording only emissions at the X4.5

vibrational interval energy⁵ of 895 cm⁻¹. DLIF spectra were taken at excitation wavelengths of 470-510 nm but no fluorescence attributable to NdO⁺ was observed.

5.3.2. Emission Spectra of Nd-based Gas Expansions

It is currently believed that in the space cloud experiments, the cloud emission profile was caused by UV-VIS solar excitation to high Nd or NdO electronic states, followed by visible emissions to lower states. In the Nd launches, emissions primarily in the green spectral region were observed. To reproduce the space cloud results in the laboratory, Nd-containing supersonic expansions were excited with 193 nm photons from the ArF excimer and the resulting dispersed fluorescence was recorded from 400-900 nm. To determine which visible emissions were atomic or molecular, dispersed spectra were recorded using either a pure He or 1% N₂O/He backing gas in the supersonic expansion. Emission spectra with the ArF laser focused and unfocused were also taken to identify if emissions originated from cooled species with little translational temperature early in the expansion stages or if the emission originated from hot, collisionally excited molecules, indicative of later stages in the evolution of the expansion. Emissions that appear only in DLIF spectra with the ArF laser unfocused can be assigned to later stages of plume evolution as the ArF laser is capable of exciting a greater spatial area of the gas expansion. Emissions in spectra with a focused ArF beam can be assigned to early stages of the expansion as in this case, only the expansion at a distance of 5 mm from the expansion orifice is excited. Figure 5.8 shows the emission spectra from the 193 nm excitation.

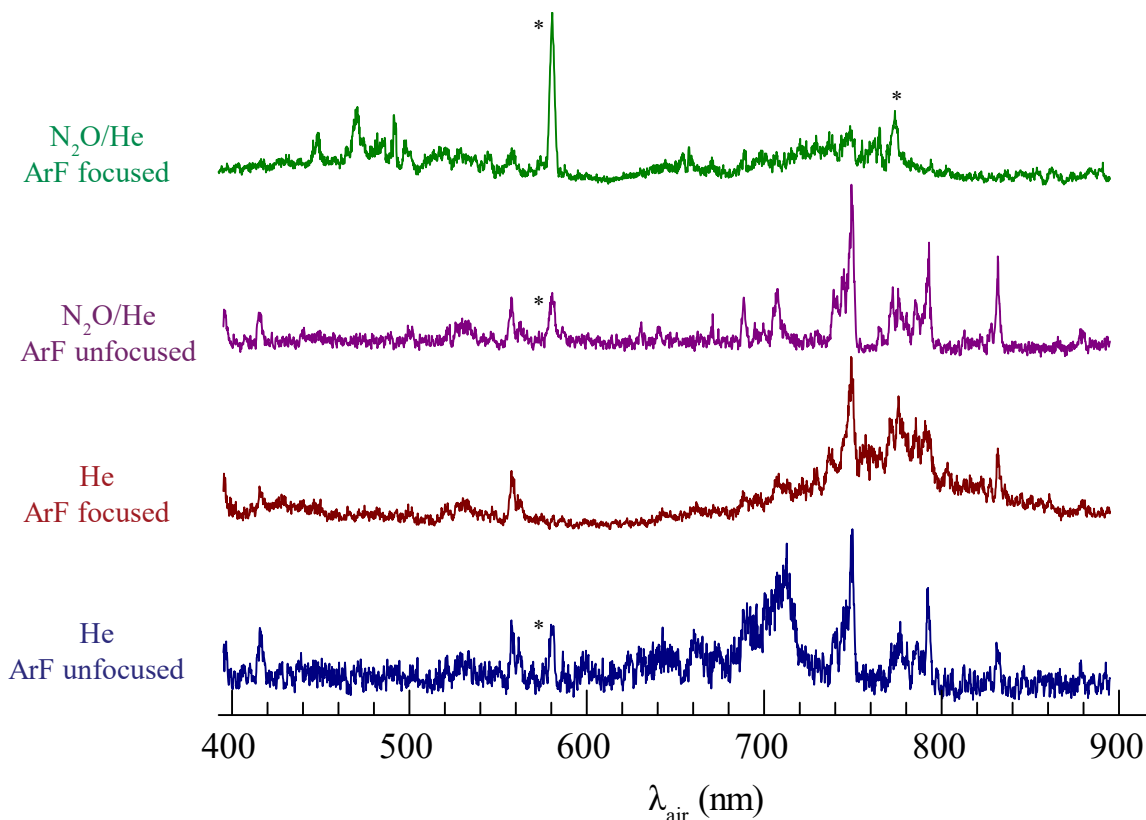


Figure 5.8. Emission spectra from Nd-containing gas expansions excited at a 193 nm ArF excitation wavelength.

Emissions marked with asterisks are the ArF light detected at higher-orders on the diffraction grating of the monochromator.

5.4 NdO and NdO⁺ Discussion

In the vibronic assignments of the NdO LIF spectra, it was found that while some of the transitions originated from vibrational zero-point levels, many of the higher energy transitions originated from vibronically excited energy levels. Vibronic levels up to 2412 cm^{-1} above the zero-point energy in the X5, (1)5, (2)4, and (1)3 electronic states were observed as transitions to lower states. In the LIF results, two sequence bands at 17541 cm^{-1} and 176013 cm^{-1} were assigned as the [18.07]4-(1)5 $n=0$ and [18.07]4-(1)5 $(n+1)=1$ transitions. An upper state vibrational interval of $\Delta G_{(n+1)-n} = 769.9\text{ cm}^{-1}$ was determined. However, the fluorescence

lifetimes values of 43(5) and 23.4(1) for the $(n+1)-1$ and $n-0$ transitions did not agree with each other, indicating the presence of a perturbation on the n level. One high-intensity band was used to obtain isotopically-resolved rotational parameters for the [20.82]4 state. Because no literature values were available for NdO isotopologues in the X4 $\nu = 2$ state, the lower state rotational constant was fixed to 0.3588 cm^{-1} and upper state rotational parameters were determined for the ^{142}NdO , ^{144}NdO , and ^{146}NdO isotopologues, presenting isotopically-resolved rotational parameters of NdO for the first time in literature. Fluorescence lifetimes were determined for all the observed LIF bands in this work, displaying a wide range of values from 25-115 ns. It was found that for most unperturbed bands, lifetimes on the order of 50 ns were observed.

In the DLIF spectra for the LIF bands of NdO, it was found that lower-energy states exhibited simpler emission spectra than their higher energy LIF band counterparts. This was somewhat expected, as due to the high density of states, the number of available emissions states would increase with increasing excitation energy. Emission spectra for the higher-energy excitations were very dense and values for the $\nu = 0$ energies and $\Delta G_{1/2}$ vibrational spacings from Linton *et al.*¹³ were used to assign transitions to vibrationally-excited energy levels of known low-lying electronic states. Observation of emissions down to excited vibrational levels (up to $\nu = 5$) of the ground X4 state has allowed a determination of the X4 ω_e constant of $838(1)\text{cm}^{-1}$. This value is consistent with X4 $\Delta G_{1/2}$ vibrational spacing values both in experimental literature^{13, 14, 16} and predicted by ligand field theory¹⁸. The DLIF spectra also exhibit emissions to vibrationally excited levels of many low-lying electronic states, which are listed in Table 5.3. The $\nu = 0$ state values determined from the DLIF spectra for these electronic states agree well with the experimental values from Linton *et al.*¹³ and ligand field predictions^{18, 19}. For the first time, ω_e values for these electronic states have been determined. It can be seen from Figure 5.7

that vibrational spacings of the ground X4 and low-lying electronic states are very similar, and these states all exhibit similar ω_e values. This is indicative of these electronic states arising from the same electronic configuration. Ligand field theory calculations have suggested that the observed low-lying electronic states in this work all arise from the ground $\text{Nd}^{2+}(4f^36s)\text{O}^{2-}(2p^6)$ configuration. This notion is supported by this work, both from the values of electronic state origins and the similar magnitude of their vibrational spacings.

Despite attempts, no LIF signal able to be correlated to NdO^+ was observed.

Photoionization with an ArF excimer laser was initially chosen due to the excimer photon having a sufficient energy (6.42 eV) to ionize NdO (5.51 eV). The beam energy per unit area was 14.3 J/cm² and it was estimated that an energy per unit area of 3.2 J/cm² was sufficient to ionize NdO. Unlike with Sm, the dissociation energy of NdO is higher than the pulse energy from the ArF excimer, NdO can only undergo ionization upon interaction with the 193 nm photon. Depletion curves of Nd and NdO would be useful in determining if ionization of NdO is actually occurring in the chamber. By exciting Nd I lines that originate in the atomic $J'' = 4$ ground state in the presence and absence of the ionization beam, the percentage of atomic Nd being depleted by the ArF beam can be determined. Inconveniently, strong Nd I lines originating from the ground state and known NdO bands originating from the ground X4 state do not lie in the same spectral region. It is therefore recommended that intense NdO [16.17]4-X4 $\nu'' = 0$ band and the Nd I line at 492.453 nm be used for depletion measurements. There is also a possibility that NdO was ionizing but then recombining with an electron on a shorter time scale than the time delay between the ArF and probing dye laser pulses. However, kinetics studies⁶ have determined that this recombination event is not favorable and highly unlikely.

There seems to be two likely explanations for the lack of NdO^+ production. First, the ionization cross section at 193 nm might be too low. The cross section of photo-ionization is dependent on the energy of ionization photon. The closer the photon energy to the ionization threshold, the higher the cross section. The ArF photon has an energy 0.91 eV greater than the ionization potential of NdO. It may be that the excess energy of the ArF pulse is limiting the ionization of NdO. One other possible explanation for the lack of observation of NdO^+ bands may be in an incorrect spectral range. As previously mentioned, when NdO ionizes, the Nd atom loses the 6s electron, obtaining a $\text{Nd}^{3+}(4f^3)\text{O}^{2-}$ configuration. This limits transitions to weak $f \leftrightarrow f$ transitions or stronger $f \leftrightarrow d$ transition typically located in the UV spectral region for lanthanides. Searches for NdO^+ LIF spectra were taken from 470-510 nm but no molecular signals were found. Future work should attempt at looking for NdO^+ transitions more into the UV.

In the laboratory, the space cloud experiments were replicated by exciting the supersonic expansion with the ArF pulse and then recording the dispersed fluorescence. Sharp, atomic features can be seen in the emission spectra centered at 750 nm. In the He-based expansions, when the ArF laser is focused, an underlying broad emission occurs also centered at 750 nm. In the expansions with N_2O , emissions appear in the 450-550 nm range, as well as the 700-800 nm range. Neither of these emissions correspond to known NdO emissions. Unfortunately, regions past 680 nm are inaccessible with the XeCl-pumped dye laser so the 700-800 nm emissions are not able to be characterized. LIF survey scans from 470-510 nm were conducted in hopes of finding NdO^+ bands, but no molecular bands were observed. It might be useful though to continue the search past either more in the green spectral region or down towards 440 nm where the emission is the strongest. Future work should pursue this avenue.

5.5 SmO Results

5.5.1. Low-Resolution LIF and DLIF Results

Rotationally-resolved laser-induced fluorescence spectra of SmO were obtained in the spectral range of 647-680 nm. Figure 5.9 shows the rotational structure of a band centered at $15,350 \text{ cm}^{-1}$ assigned as the $[15.35]1-XO^-(v=0)$ transition with a rotational temperature of 50K. Typically, rotational temperatures observed in the SmO spectra ranged from 10-50K.

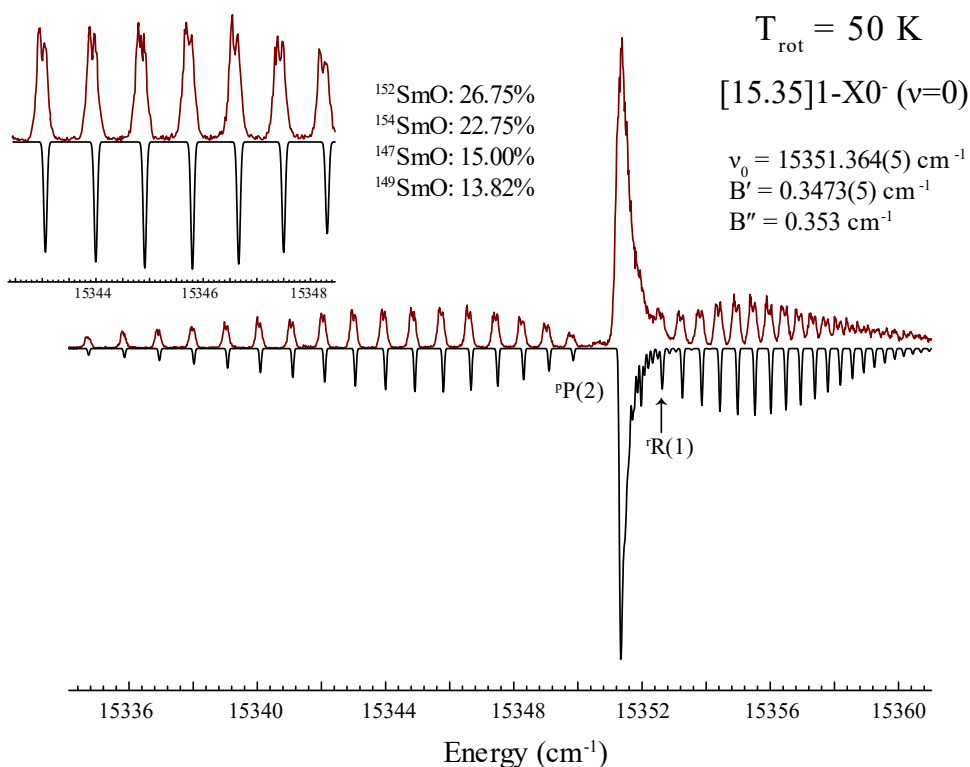


Figure 5.9. Rotationally-resolved LIF spectrum of the SmO $[15.35]1-XO^-(v=0)$ transition. The insert shows the isotopic splitting of the rotational lines as well the natural abundance for the four prominent SmO isotopes.

In Figure 5.9, the downward trace is a theoretical simulation generated by PGOHPER³³. Upper and lower states were treated as Hund's case (c) and rotational energies were fitted to

$$F_v(J) = B_v[J(J+1) - \Omega^2] + \frac{1}{2}q[J(J+1)] \quad (5.4)$$

where Ω is the total angular momentum projection on the internuclear axis and q is a Ω -doubling constant introduced for states with $|\Omega| > 0$. As can be seen from Figure 5.9, isotopic splitting of the rotational lines was partially resolved, with each rotational line being split into two features. These two features were assigned as ^{152}SmO and ^{154}SmO lines, as the ^{152}Sm and ^{154}Sm isotopes have the greatest natural abundancies of 26.75% and 22.75%. The theoretical fit generated in Figure 5.9 is for the more intense ^{152}SmO isotopologue. Seven SmO transitions were observed in the spectral region but only four of these were able to be rotationally fit. For each band, separate rotational fits were performed for the ^{152}SmO and ^{154}SmO isotopologues. Molecular constants obtained from the fits are shown in Table 5.4. Rotational constants for the $(1)1 \nu = 0$ and $X0^- \nu = 0, 1$ levels were held constant in the fitting process using values taken from Bujin *et al.*²⁴.

Table 5.4. Molecular constants determined from rotational fits of SmO bands.

Isotope	$[T_0] \Omega'-(M'')\Omega''$	ν_0 (cm ⁻¹)	q (cm ⁻¹)	B' (cm ⁻¹)	B'' (cm ⁻¹)	Avg Res (cm ⁻¹)
^{152}SmO	[15.43]0 ⁻ -(1)1 ($\nu = 0$)	15277.64(1)	0.0106(1)	0.3660(5)	0.357	0.042
^{154}SmO	[15.43]0 ⁻ -(1)1 ($\nu = 0$)	15277.48(1)	0.0104(1)	0.3650(5)	0.357	0.035
^{152}SmO	[15.35]1-X0 ⁻ 1-1	15301.03(1)	0.0182(3)	0.3471(5)	0.352	0.023
^{154}SmO	[15.35]1-X0 ⁻ 1-1	15301.01(1)	0.0177(3)	0.3453(1)	0.351	0.014
^{152}SmO	[15.35]1-X0 ⁻ 0-0	15351.364(5)	0.0153(1)	0.3473(5)	0.353	0.022
^{154}SmO	[15.35]1-X0 ⁻ 0-0	15351.229(5)	0.01567(7)	0.3471(5)	0.353	0.014
^{152}SmO	[17.21]2-(1)1($\nu = 2$)	15417.98(2)	---	0.3562(5)	0.355(1)	0.017
^{154}SmO	[17.21]2-(1)1($\nu = 2$)	15417.958(7)	---	0.3543(4)	0.3559(3)	0.015

Figure 5.10 shows the dispersed fluorescence spectra for the observed SmO excitation bands. The spectra are in terms of the relative energy difference from the resonant transition and laser scatter has been subtracted from the laser resonant transitions. Vibronic features with

negative relative energies correspond to emissions with greater energy than the excitation energy.

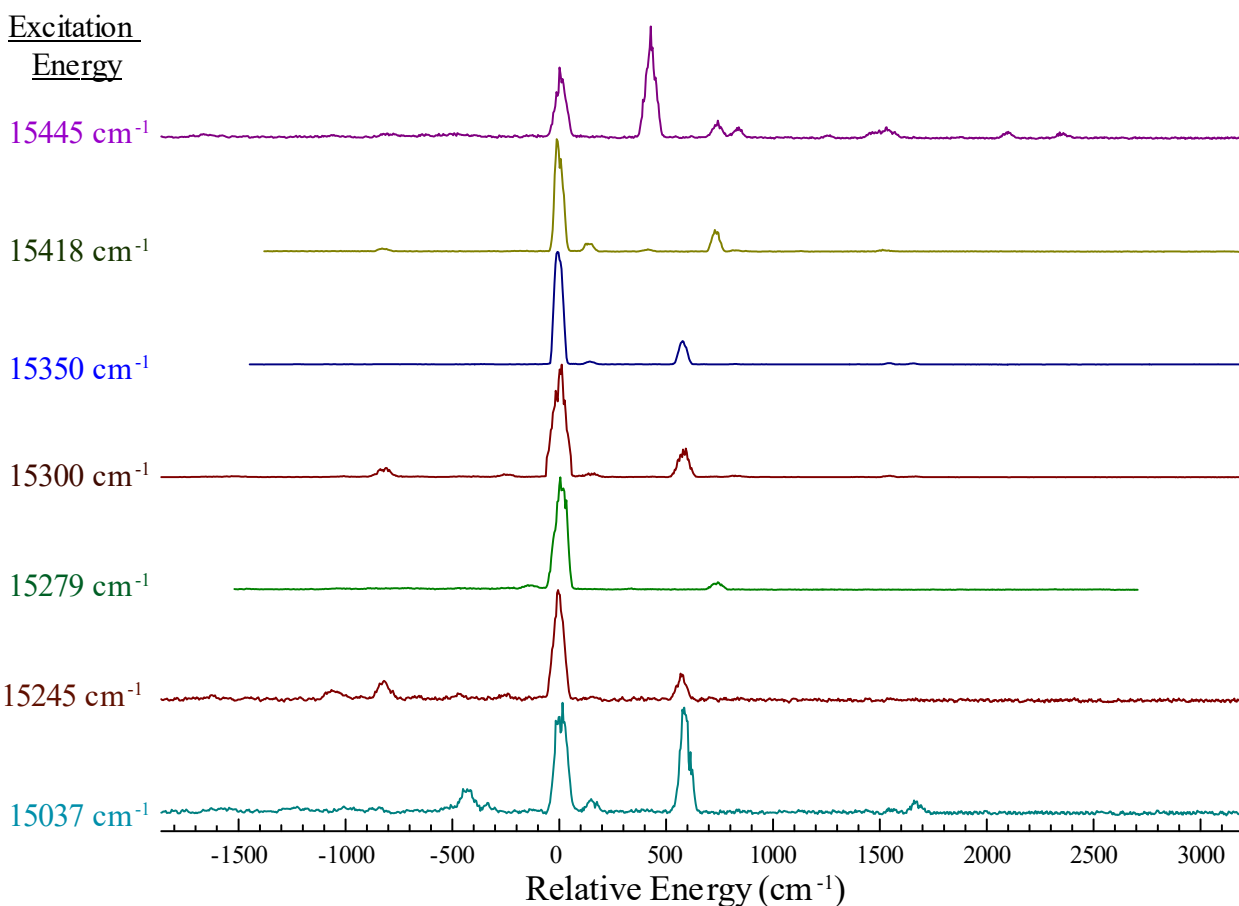


Figure 5.10. Dispersed fluorescence spectra of seven observed SmO bands.

Figure 5.11 shows the DLIF spectrum of the $[15.35]1-X0^- 0-0$ excitation with emissions labeled with the corresponding low-lying excited state. In this spectrum, vibronic emissions down to the ground vibrational level of the electronic ground $X0^-$ state or low-lying electronic states are observed. A transition to the first vibrationally excited level of the $X0^-$ state was observed around 820 cm^{-1} .

It can also be inferred that these states behave well within a Hund's case (c) coupling scheme, as the emissions observed rigidly followed the $\Delta\Omega=0,\pm 1$ selection rule.

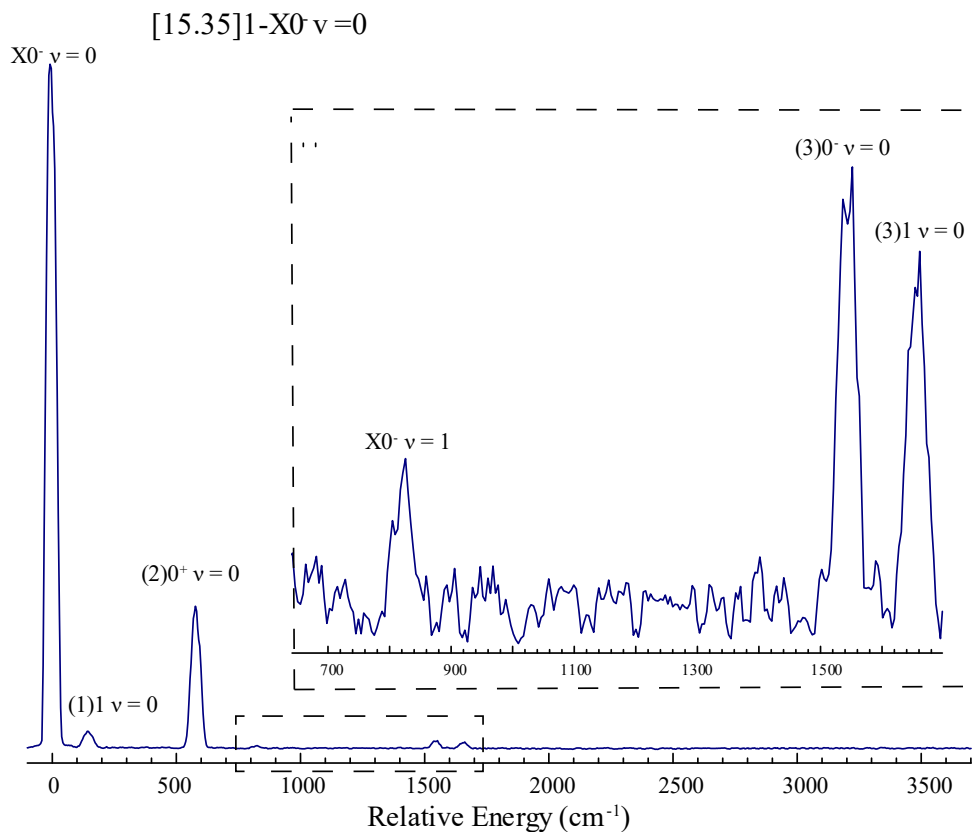


Figure 5.11. DLIF spectrum of the SmO [15.35]1-X0⁻ 0-0 excitation.

Throughout the seven collected DLIF spectra, transitions to vibrationally-excited low-lying electronic states were observed, allowing vibrational characterization of these states. Vibrational energies $G(\nu)$ were plotted as a function of $\nu + 0.5$, which is shown in Figure 5.12.

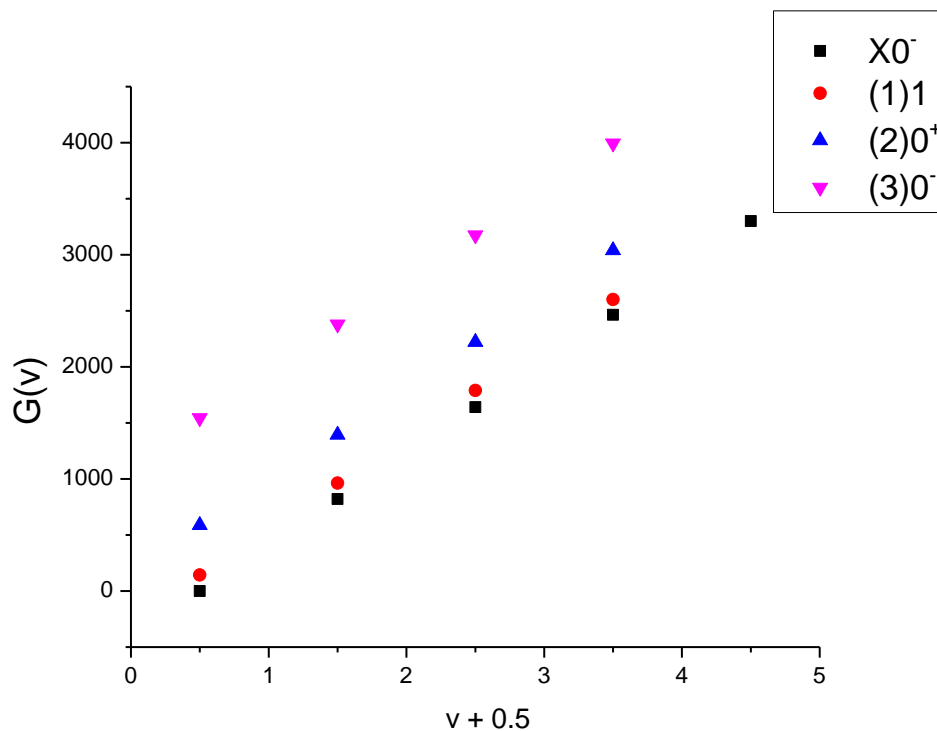


Figure 5.12. Vibronic energies of the electronic ground and low-lying states determined from the DLIF spectra plotted as a function of $v + 0.5$.

Vibrational energies were then fit to the simple Morse energy level expression (Equation 3.4.), allowing determination of the vibrational constant ω_e . Due to the low resolution of the spectra, the anharmonicity constants could not be determined with statistical significance. The fitting results are shown in Table 5.5.

Table 5.5. Vibrational parameter ω_e for the electronic ground $X0^-$ and low-lying states determined from dispersed spectra.

(M) Ω	ω_e (cm $^{-1}$)	v levels in fit
$X0^-$	824(2)	0-4
(1)1	820(2)	0-3
(2)0 $^+$	819(3)	0-3
(3)0 $^-$	815(5)	0-3

5.5.2. Fluorescence Lifetime and Einstein coefficients A_{ij} Determination

Fluorescence decay curves were recorded for the excited states in Table 5.4 and are listed in Table 5.6. Decay curves were taken by setting the dye laser to excite the most intense rotational feature of a band, which was typically a bandhead or low- J rotational line. The decay curves exhibited single-exponential behavior and fitted lifetimes are reported in Table 5.6

Table 5.6. Measured fluorescence lifetimes of SmO transitions.

$[T_0] \Omega'$	τ (ns)
[15.03]	227(8)
[15.25]	73(9)
[15.43]0 ⁺	67(2)
[15.35]1, $v'=1$	66(5)
[15.35]1, $v'=0$	61(5)
[17.21]2	47(1)
[15.45]	117(4)

To determine the Einstein coefficients A_{ij} for an upper state in Table 5.3, the total decay rate of the upper state was determined by taking the inverse of the fluorescence lifetime. The total decay rate was then partitioned between the emissions in the dispersed fluorescence spectra according to their scatter-subtracted relative intensities. As an example, Table 5.7 shows the Einstein coefficients for emissions from the [15.35]1, $v'=0$ state.

Table 5.7. Determined Einstein coefficients A_{ij} for emissions observed in the [15.35]1-X0⁻ 0-0 DLIF spectrum.

Emission to (M) Ωv	A_{ij} (s^{-1}) x 10^{-6}
X0 ⁻ $v=0$	7.56
(1)1 $v=0$	1.53
(2)0 ⁺ $v=0$	3.25
X0 ⁻ $v=1$	1.33
(3)0 ⁻ $v=0$	1.40
(3)1 $v=0$	1.38

Einstein coefficients for the remaining observed vibronic states can be found in Section 5.8.

Some emissions could not be assigned to known vibronic states, so these emissions are simply listed with their relative energy value from the pump energy.

5.5.3 Hyperfine Structure of the [15.35]1 State

Using the high-resolution LIF techniques outlined in Section 2.2.2, the hyperfine structure of the [15.35]1 state was obtained by probing the [15.35]1-X0⁻ 0-0 band at 15350 cm⁻¹. Figure 5.13 shows the hyperfine structure of the R(4) line of the [15.35]1-X0⁻ 0-0 band for the ¹⁴⁹SmO, ¹⁴⁸SmO, and ¹⁴⁷SmO isotopologues with a downward theoretical fit generated by PGOPHER for the odd isotopologues.

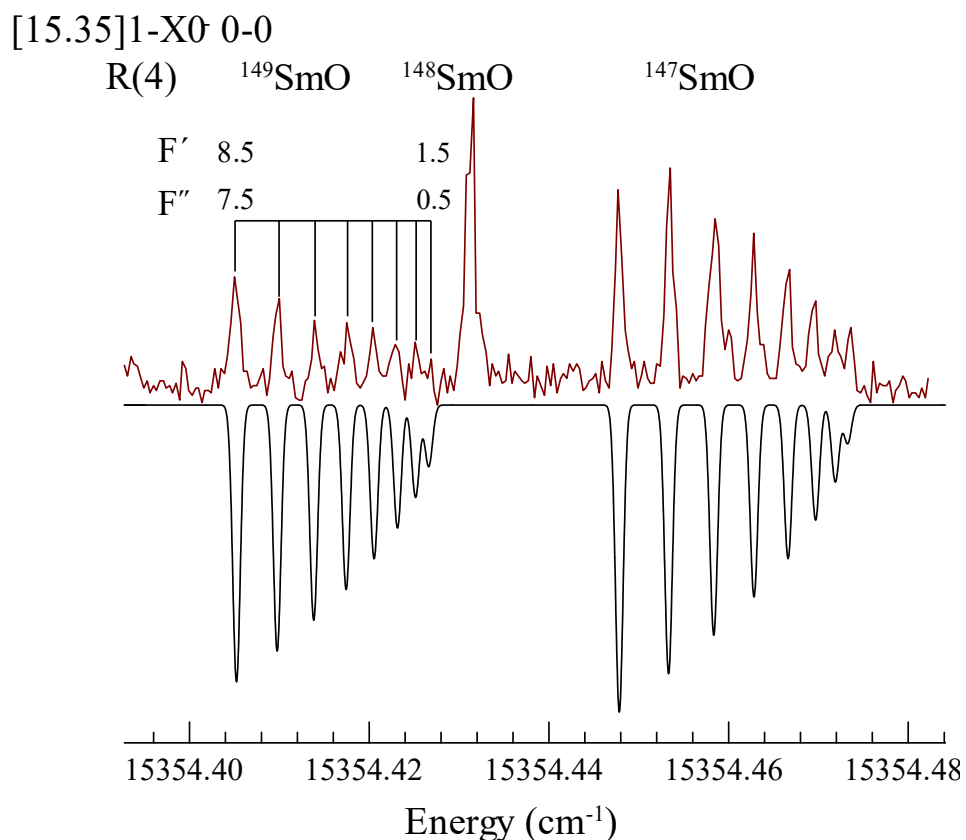


Figure 5.13. Hyperfine structure of the [15.35]1-X0⁻ 0-0 R(4) line of the ¹⁴⁹SmO, ¹⁴⁸SmO, and ¹⁴⁷SmO isotopologues.

In nuclear hyperfine structure, the nuclear spin I couples with the electronic angular momentum J to produce the total angular momentum F , where F takes the values

$$F = (I + J), (I + J - 1), \dots |I - J| \quad (5.5)$$

With large J values, F spans $2I + 1$ components for isotopes with non-zero nuclear spin. Since the ground XO^+ possess no electronic angular momentum, all hyperfine levels will be degenerate. The [15.35]1 state however will split into $2I + 1$ components when $J \geq I$ for isotopologues with nuclear spin. In SmO, all the even isotopologues possess zero nuclear spin. They therefore will exhibit no hyperfine structure. The ^{149}SmO and ^{147}SmO isotopologues, however, possess nuclear spins of $I = 7/2$ and will therefore split in eight components for $J > 7/2$. This is evident in Figure 5.13, where one can see that the ^{149}SmO and ^{147}SmO isotopologues split into seven features while the line for the ^{148}SmO isotopologue remains unsplit.

Using PGOPHER, in addition to the rotational energy expression in Equation 5.4, the hyperfine transitions were fit to the following hyperfine Hamiltonian³⁴

$$\hat{H}_{hf} = a\hat{I} \cdot \hat{L} + b\hat{I} \cdot \hat{S} + \frac{1}{3}c(3\hat{I}_z\hat{S}_z - \hat{I} \cdot \hat{S}) + \frac{eQq_0}{4I(2I-1)}(3\hat{I}_z^2 - \hat{I}^2) \quad (5.6)$$

where \hat{I} is the nuclear spin of the Sm atom, \hat{S} is the electronic spin angular momentum and \hat{I}_z and \hat{S}_z are their z-axis projections. In Equation 5.5, the $a\hat{I} \cdot \hat{L}$ term represents the nuclear spin – electron orbital angular momentum interaction, $b\hat{I} \cdot \hat{S}$ represents the Fermi contact interaction, and the c term represents the dipolar electron spin – nuclear spin interaction. The final term in Equation 5.5 is the nuclear quadrupole Hamiltonian, where eQq_0 is the nuclear quadrupole coupling constant.

In the fitting process, the rotational constant B_v and Λ -doubling parameter q were fixed to values from Table 5.4. The band origin ν_0 along with the nuclear spin-orbit interaction parameter a and nuclear quadrupole coupling parameter eQq_0 were fitted to the experimental spectrum of

the odd isotopologues. Table 5.8 shows the fitting results for the [15.35]1-X0⁻ 0-0 R(2-5) lines for the ¹⁴⁹SmO and ¹⁴⁷SmO isotopologues. It should be noted that while the band center is listed in units of wavenumbers, the other parameters are displayed with MHz units.

Table 5.8. Hyperfine fitting results for the [15.35]1-X0⁻ 0-0 R lines.

Transition	Line	Isotope	ν_0 (cm ⁻¹)	a (MHz)	eQq ₀ (MHz)	Avg Res (MHz)
[15.35]1-X0 ⁻ 0-0	R(2)	147	15351.404327(3)	-366(1)	---	2.28
		149	15351.3613(1)	-306(4)	---	8.29
	R(3)	147	15351.40643(4)	-463(2)	---	2.67
		149	15351.36224(6)	-388(4)	---	4.36
	R(4)	147	15351.41090(2)	-593(1)	-28(6)	1.38
		149	15351.36622(7)	-492(4)	-82(20)	4.69
	R(5)	147	15351.41041(5)	-727(4)	-29(16)	3.59
		149	15351.36478(7)	-618(5)	---	5.63

For some fits, the standard deviation of the eQq₀ parameter produced by the theoretical fit was larger than its value so it was not included in the final version of the fit.

5.6 Preliminary SmO⁺ Results

5.6.1 Sm and SmO Depletion

An ArF (193 nm, 14.3 J/cm²) excimer laser was used to photoionize SmO at a time interval of 1.5 μ s before the probe dye laser. Initially, LIF spectral ranges in which SmO transitions were observed were chosen to search for SmO⁺ LIF transitions. Two spectral regions of 550-570 nm and 625-650 nm, in which SmO transitions are plentiful, were employed for initial searches but no excimer-dependent transitions were observed. It was then considered that upon ionization, the ground state electronic configuration of Sm³⁺(4f⁵)O²⁻ restricts electronic orbital transitions of $f \leftrightarrow f$ and $f \leftrightarrow d$ types. Typically, $f \leftrightarrow f$ transitions for lanthanides are rather weak and are located in the infrared region, which is out of the spectral scope of this project. The stronger $f \leftrightarrow d$ transitions, however, are theorized to occur in the UV spectral range.

Consequently, the spectral range used to search for SmO^+ transitions was shifted to blue and UV wavelengths. Searches for LIF spectra were made for the wavelength ranges 365-376 nm and 420-450 nm, but no molecular ion signals were found. The two spectral regions had high densities of atomic transitions but no features that exhibited typical molecular band structures were observed in either region.

To determine whether SmO^+ was being produced, depletion measurements of both atomic samarium and SmO were conducted. In these experiments, the dye laser was set to excite fluorescence from a Sm or SmO transition, and traces of the fluorescence decays were recorded in the absence and presence of the ArF ionization laser beam (for example, see Fig. 5.14). The time delay between the ArF and dye laser pulses was varied to produce the greatest depletion of Sm or SmO . Atomic Sm transitions at 17,775 and 17,788 cm^{-1} were chosen for depletion measurements, as they were located in the prevalent SmO spectral region, and they originated from either the atomic ground or the first excited state. An optimal time delay for the atomic Sm depletion was found to be 750 ns and, at this time delay, the fluorescence at 17,775 and 17,788 cm^{-1} was found to be depleted by 22.2% and 17.6%, respectively. The traces of the 17,788 cm^{-1} fluorescence in the absence and presence of the ionization laser are shown in Figure 5.14.

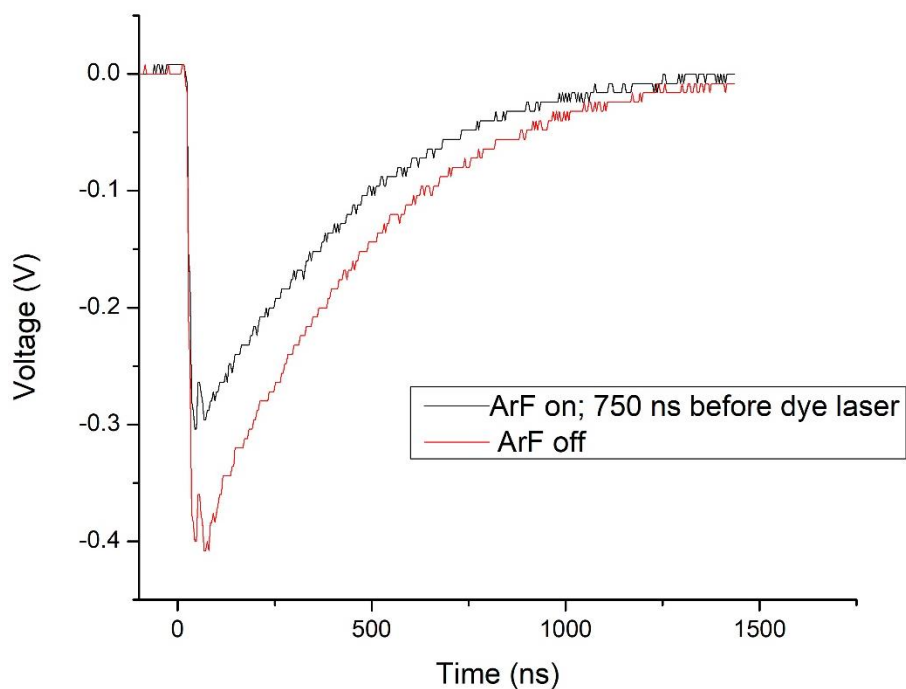


Figure 5.14. Sm fluorescence at $17,778\text{ cm}^{-1}$ depletion measurements.

For SmO, the $[15.35]1-X0^{\cdot} 0-0$ band was chosen for depletion measurements as the lower state is the zero-point energy of SmO. At an optimal time delay between the ArF and dye laser pulses of 600 ns, SmO fluorescence curves were recorded in the absence and presence of the ArF laser and are shown in Figure 5.15. A total SmO depletion of 12.7% was observed.

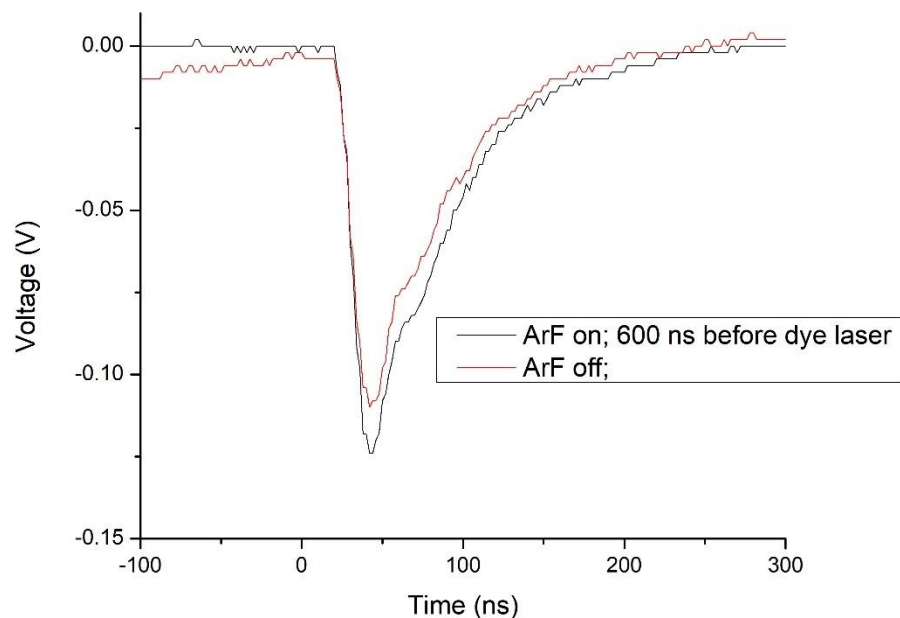


Figure 5.15. SmO [15.35]-X0⁻0-0 fluorescence depletion measurements.

5.6.2. Emission Spectra of UV-Excited Sm-based Gas Expansions

It is currently believed that in the space cloud experiments, the cloud emission profile was caused by solar excitation to Sm or SmO electronically electronic states, followed by visible emissions to lower states. To reproduce the space cloud results in the laboratory, Sm-based supersonic expansions were excited with 193 nm photons from the ArF excimer and the resulting dispersed fluorescence was recorded from 400-900 nm. To determine which visible emissions were atomic or molecular, dispersed spectra were recorded using either a pure He or 1% N₂O/He backing gas in the supersonic expansion. Emission spectra with the ArF laser focused and unfocused were also taken to identify if emissions originated from cooled species with little translational temperature early in the expansion stages or if the emission corresponds to collisional electronic relaxation, which would be indicative of molecules in later stages in the evolution of the expansion. Figure 5.16 shows the emission spectra from the 193 nm excitation.

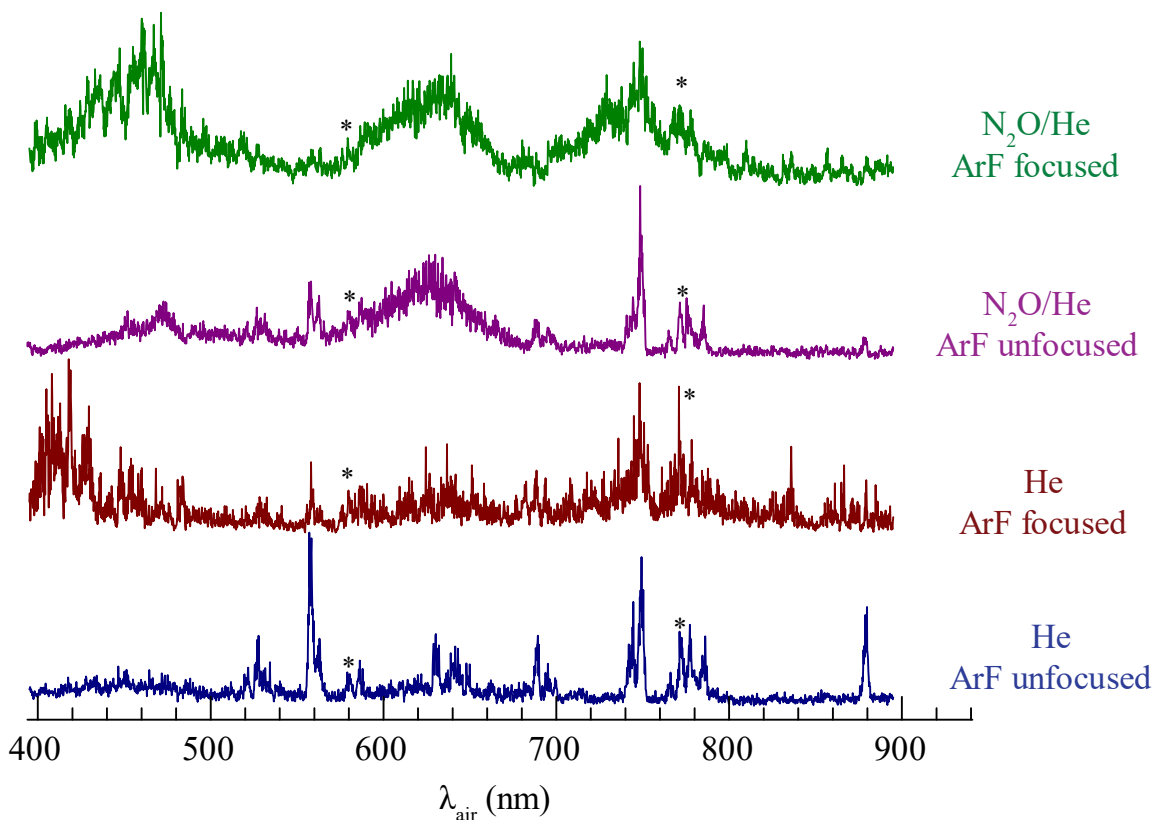


Figure 5.16. Emission spectra from Sm-based gas expansions excited at a 193 nm ArF excitation wavelength.

It should be noted that emissions at 579 and 772 nm marked with asterisks in Figure 5.16 are resonant ArF pulses detected at higher diffraction orders of the monochromator grating.

5.7 SmO and SmO⁺ Discussion

In the Sm space cloud experiments, high intensity broad emission features from 611-661 nm were observed and attributed to molecular emissions. In this work, SmO transitions have been observed in the same spectral region, suggesting that the red emission features in the space cloud can be assigned as SmO transitions. In the LIF experiments, strong, intense SmO transitions originating from the ground X⁰⁻ electronic state and the (1)1 first low-lying excited state were observed from 647-680 nm. Out of the four rotationally analyzed bands, two bands belonged to a $\Delta v = 0$ sequence [15.35]1 and X⁰⁻ states, as suggested by the rotational fits, the

DLIF spectra, and similar lifetimes. These sequences bands have allowed for a determination of the $[15.35]1 \Delta G_{1/2}$ vibrational spacing, with values of 772.0 cm^{-1} and 771.6 cm^{-1} for the ^{152}SmO and ^{154}SmO isotopologues, respectively. For the first time, a vibrationally excited state of the electronic (1)1 state has been rotationally analyzed for the two major isotopologues of SmO.

In the dispersed fluorescence spectra, vibrational progressions of multiple electronic states were observed, exhibiting a linear dependency on $\nu + 0.5$ (within the experimental error limits). Observation of emissions down to excited vibrational levels (up to $\nu = 4$) of the ground $X0^-$ has allowed a determination of the $X0^- \omega_e$ constant of $824(2) \text{ cm}^{-1}$. This value is consistent with $X0^- \Delta G_{1/2}$ vibrational spacing values both in experimental literature²²⁻²⁶ and predicted by ligand field theory²². The DLIF spectra also exhibit emissions to vibrationally excited levels of the (1)1, (2)0⁺ and (3)0⁻ low-lying states. The $\nu = 0$ state energies determined from the DLIF spectra for these electronic states agree well with the experimental values from Bujin *et al.*²⁴ and ligand field predictions^{17, 29}. For the first time, ω_e values for the (1), (2)0⁺, and (3)0⁻ states have been determined. It can be seen from Figure 5.12 that vibrational spacings of the ground $X0^-$ and low-lying states are very similar, and these states all exhibit similar ω_e values. This is indicative of these electronic states arising from the same electronic configuration. Ligand field theory calculations have suggested that the $X0^-$, (1)1, (2)0⁺, and (3)0⁻ states all arise from the ground $\text{Sm}^{2+}(4f^5 6s)O^{2-}(2p^6)$ configuration. This notion is supported by this work, both from the values of electronic state origins and the similar magnitude of their vibrational spacings.

In this work, the fluorescence lifetime of seven SmO transitions were determined and exhibited single-exponential behavior. It should be noted that while Hannigan²¹ also observed LIF transitions attributed to SmO from 647-655 nm, the lifetimes she observed exhibited double-exponential decay behavior. The discrepancy between the single-exponential lifetime behavior of

this work and the double-exponential lifetime behavior observed by Hannigan can mostly likely be attributed to the method of SmO production. Hannigan produced SmO under thermally hot conditions, which involved heating Sm metal in an oven up to 1000°C, after which the Sm metal beam was collided with a SO₂ molecular beam to form SmO. This process resulted in hot, collisionally excited SmO. In contrast to Hannigan's production method, this work employed supersonic expansion techniques, producing SmO under collision-free conditions, resulting in cooled internal degrees of freedom. Bi-exponential fluorescence decays are typically observed when after excitation the molecule is collisionally transferred to a lower energy state, from which the molecule relaxes to a final lower state. Because Hannigan produced SmO under hot collisional conditions, it is very plausible that the bi-exponential decay curves she observed were due to collisional relaxation. Since this current work produced SmO under collision free environments, single-exponential decay behavior is expected.

Einstein coefficients have been determined for emissions observed in eight different SmO transition using the fluorescence lifetimes and emission intensities from the dispersed fluorescence spectra. Typically, the calculated Einstein coefficients were on the order of 10⁴-10⁶ s⁻¹. To properly model the Sm space cloud releases, the Einstein coefficients for SmO as well as the solar pumping rate are needed. For the first time, SmO Einstein coefficients are reported and provide the opportunity to successfully model the space cloud launches.

Using high-resolution laser induced fluorescence, the hyperfine structure of the [15.35]1 state was obtained using several rotational lines in the R branch of the [15.35]1-X⁰ 0-0 transition. It was found that the magnitude of both the nuclear spin-orbit interaction parameter a and the nuclear quadrupole coupling parameter eQq_0 were both negative. The negative a value is apparent from the hyperfine spectra, as transitions with larger values of F have lower energies.

The negative value for the nuclear quadrupole parameter eQq_0 indicates a nuclear oblate symmetry. The Fermi contact interaction parameter b describes the interaction between nuclear and electron spin when an outer electron penetrates the nucleus. Because only s electrons have a non-zero probability density at the nucleus, the b parameter has a non-zero value for states arising from electronic configurations with $s\sigma$ character. In the $[15.35]1-X0^- 0-0$ hyperfine structure fits, a zero value for the Fermi interaction contact parameter was obtained. This implies that the $[15.35]1$ state has very little $s\sigma$ character, indicating that this state may arise from the promotion of the $6s$ electron to a $p\pi$ orbital or it may arise from the excitation of the f manifold. Unfortunately, without computational work, the only thing that can be said with certainty is that the $[15.35]1$ state has little to no $s\sigma$ character. Further investigation should obtain the hyperfine structure of the $[15.35]1-X0^- 1-1$ band to confirm the Fermi interaction contact parameter as well as obtain the hyperfine structure of the $(1)1$ state using the $[15.43]0^-(1)1$ ($v = 0$) transition. Since the $(1)1$ is theorized to arise from a $\text{Sm}^{2+}(4f^56s)\text{O}^{2-}$ configuration, the structure should indicate a non-zero value of b , due to the unpaired s electron.

The lack of observation of SmO^+ is puzzling. Photoionization with an ArF excimer laser was initially chosen due to the excimer photon having a sufficient energy (6.42 eV) to ionize SmO (5.74 eV). The beam energy per unit area was typically 14.3 J/cm^2 and it was estimated that an energy per unit area of 3.2 J/cm^2 was sufficient to ionize SmO. The depletion results for atomic samarium were pretty straightforward, indicating that atomic samarium was undergoing ionization, as that is the only energy path for an atom absorbing energy greater than its ionization potential. The results for the SmO depletion were less clear. SmO, upon absorbing 6.42 eV, can either ionize (5.73 eV) or dissociate (5.72 eV). There is a possibility that the depletion of SmO was due to SmO dissociating and not ionizing. It was also considered that perhaps SmO was

ionizing but recombining with an electron on a shorter time scale than the time delay between the ArF and probing dye laser pulses. However, kinetics studies⁶ have determined that this recombination event is not favorable and highly unlikely.

There seems to be two likely explanations for the lack of SmO^+ production. First, the ionization cross section at 193 nm might be too low. The cross section of photo-ionization is dependent on the energy of ionization photon. The closer the photon energy to the ionization threshold, the higher the cross section. The ArF photon has an energy 0.68 eV greater than the ionization potential of SmO. It may be that the excess energy of the ArF pulse is limiting the ionization of SmO. One other possible explanation for the lack of observation of SmO^+ bands may be an incorrect spectral range. As previously mentioned, when SmO ionizes, the Sm atom loses the 6s electron, obtaining a $\text{Sm}^{3+}(4f^5)\text{O}^{2-}$ configuration. This limits transitions to weak $f \leftrightarrow f$ transitions or stronger $f \leftrightarrow d$ transition typically located in the UV spectral region for lanthanides. Searches for SmO^+ LIF spectra were taken from 365-376 nm and 420-450 nm but no molecular signals were found. Future work should attempt at looking for SmO^+ transitions more into the UV.

In the laboratory, the space cloud experiments were replicated by exciting the supersonic expansion with the ArF pulse and then recording the dispersed fluorescence. Sharp, atomic features can be seen in the emission spectra centered at 560 nm and 750 nm. In the He-based expansions, when the ArF laser is focused, a strong broad emission profile appears at 400 nm. This is indicative of Sm^+ emissions, as in a He-based supersonic expansion, this would be the most prevalent species right after expansion, experiencing little to no collisions. This can also be confirmed with the Sm II spectral database by Lawler *et al.*³⁵, in which intense Sm II transitions are found from 380 – 430 nm. In the expansions with N_2O , a broad emission center around 620

nm is observed and, upon focusing the ArF laser, broad emissions around 460 nm and 740 nm are observed as well. The emission around 640 nm is probably indicative of neutral SmO emissions, as confirmed by this work and previous experimental works^{22, 24}. The question arises to whether the emissions at 460 nm and 740 nm belong to neutral SmO or the cation SmO⁺. Unfortunately, regions past 680 nm are inaccessible with the XeCl-pumped dye laser so the 740 emission was not able to be characterized. LIF survey scans from 430-450 nm were conducted in hopes of find SmO⁺ bands but no molecular bands were observed. It might be useful though to continue the search past 450 nm where the emission is the strongest. Future work should pursue this avenue.

5.8 SmO Einstein A_{ij} Coefficients

Table 5.9. Einstein coefficients for the [15.03]state.

Emission to (M) Ωv	A_{ij} (s ⁻¹) x 10 ⁻⁶
-1604	0.255
-1188	0.0528
-985	0.0397
-575	0.712
0	0.873
141	0.086
576	2.26
1555	0.0242
1663	0.101

Table 5.10. Einstein coefficients for the [15.25] state.

Emission to (M) Ωv	A_{ij} (s ⁻¹) x 10 ⁻⁶
X0 ⁻ $v=0$	0.54
(2)0 ⁺ $v=0$	0.88
X0 ⁻ $v=1$	1.49
(1)1 $v=1$	0.49
1150 cm ⁻¹	0.65
(2)0 ⁺ $v=1$	0.65
X0 ⁻ $v=2$	6.65
(1)1 $v=2$	0.43
(2)0 ⁺ $v=2$	1.98

Table 5.11. Einstein coefficients for the [15.43]0⁻ state.

Emission to (M) Ωv	$A_{ij} (s^{-1}) \times 10^{-6}$
X0 ⁻ $v=0$	4.11
(1)1 $v=0$	6.70
(2)1 $v=0$	4.24

Table 5.12. Einstein coefficients for the [15.25]1 $v = 1$ state.

Emission to (M) Ωv	$A_{ij} (s^{-1}) \times 10^{-6}$
X0 ⁻ $v=0$	0.042
(1)1 $v=0$	0.096
600 cm ⁻¹	0.091
X0 ⁻ $v=1$	0.859
(1)1 $v=1$	0.076
(2)0 ⁺ $v=1$	0.268
X0 ⁻ $v=2$	10.5
(1)1 $v=2$	0.326
(2)0 ⁺ $v=2$	2.56
(3)0 ⁻ $v=1$	0.049
X0 ⁻ $v=3$	0.145
(1)1 $v=3$	0.021
(3)0 ⁻ $v=2$	0.129
X0 ⁻ $v=4$	0.062

Table 5.13. Einstein coefficients for the [17.21]2 state.

Emission to (M) Ωv	$A_{ij} (s^{-1}) \times 10^{-6}$
(1)2 $v=0$	0.321
(1)1 $v=1$	0.252
(1)1 $v=2$	15.4
(4)1 $v=0$	0.279
(1)2 $v=2$	0.307
(3)1 $v=1$	4.01
(1)1 $v=3$	0.24
(1)3 $v=2$	0.0726
(3)1 $v=2$	0.555

Table 5.14. Einstein coefficients for the [15.45] state.

Emission to (M) Ωv	A_{ij} (s ⁻¹) x 10 ⁻⁶
X0 ⁻ $v=0$	0.17
X0 ⁻ $v=1$	0.19
X0 ⁻ $v=2$	2.40
2060 cm ⁻¹	3.77
(3)0 ⁻ $v=1$	0.62
X0 ⁻ $v=3$	0.40
2900 cm ⁻¹	0.13
3100 cm ⁻¹	0.23
(3)0 ⁻ $v=2$	0.39
3750 cm ⁻¹	0.25
(3)0 ⁻ $v=3$	0.21

5.9 Chapter 5 References

1. Shuman, N. S.; Hunton, D. E.; Viggiano, A. A., Ambient and Modified Atmospheric Ion Chemistry: From Top to Bottom. *Chemical Reviews* **2015**, *115* (10), 4542-4570.
2. Kung Chie, Y.; Chao-Han, L., Radio wave scintillations in the ionosphere. *Proceedings of the IEEE* **1982**, *70* (4), 324-360.
3. Wernik, A. W.; Alfonsi, L.; Materassi, M., Scintillation modeling using in situ data. *Radio Science* **2007**, *42* (1), RS1002.
4. Johnson, M. Correspondance, 2021.
5. VanGundy, R. A.; Persinger, T. D.; Heaven, M. C., Low energy states of NdO⁺ probed by photoelectron spectroscopy. *The Journal of Chemical Physics* **2019**, *150* (11), 114302.
6. Cox, R. M.; Kim, J.; Armentrout, P. B.; Bartlett, J.; Vangundy, R. A.; Heaven, M. C.; Ard, S. G.; Melko, J. J.; Shuman, N. S.; Viggiano, A. A., Evaluation of the exothermicity of the chemi-ionization reaction $\text{Sm} + \text{O} \rightarrow \text{SmO}^+ + \text{e}^-$. *The Journal of Chemical Physics* **2015**, *142* (13), 134307.
7. Caton, R. G.; Pederson, T. R.; Paris, R. T.; Groves, K. M.; Bernhardt, P. A.; Cannon, P. S. American Geophysical Union, Fall Meeting, 2013.
8. Groves, K. M.; Caton, R. G.; Pederson, T. R.; Paris, R. T.; Su, Y.; Cannon, P. S.; Jackson-Booth, N. K.; Angling, M. J.; Retterer, J. M. American Geophysical Union, Fall Meeting, 2013.
9. Holmes, J. M.; Dressler, R. A.; Pedersen, T. R.; Caton, R. G.; Miller, D., A combined spectroscopic and plasma chemical kinetic analysis of ionospheric samarium releases. *Radio Science* **2017**, *52* (5), 521-538.

10. Ard, S. G.; Shuman, N. S.; Martinez, O.; Brumbach, M. T.; Viggiano, A. A., Kinetics of chemi-ionization reactions of lanthanide metals (Nd, Sm) from 150 to 450 K. *The Journal of Chemical Physics* **2015**, *143* (20), 204303.
11. Kaledin, L. A.; Shenyavskaya, E. A.; Kovács, I., Electronic spectrum of NdO. *Acta Physica Hungarica* **1983**, *54* (1-2), 189-212.
12. Shenyavskaya, E. A.; Bernard, A.; Vergès, J., High resolution study of near-infrared emission spectra of ^{142}NdO . *Journal of Molecular Spectroscopy* **2003**, *222* (2), 240-247.
13. Linton, C.; Effantin, C.; Crozet, P.; Ross, A. J.; Shenyavskaya, E. A.; D'Incan, J., Laser induced fluorescence spectroscopy of ^{142}NdO . *Journal of Molecular Spectroscopy* **2004**, *225* (2), 132-144.
14. Effantin, C.; Bernard, A.; Crozet, P.; Ross, A. J.; D'Incan, J., Spectroscopy of ^{142}NdO : New results. *Journal of Molecular Spectroscopy* **2005**, *231* (2), 154-164.
15. Linton, C.; Ma, T.; Wang, H.; Steimle, T. C., The permanent electric dipole moments and magnetic g factors of neodymium monoxide. *The Journal of Chemical Physics* **2008**, *129* (12), 124310.
16. Babin, M. C.; Dewitt, M.; Devine, J. A.; McDonald, D. C.; Ard, S. G.; Shuman, N. S.; Viggiano, A. A.; Cheng, L.; Neumark, D. M., Electronic structure of NdO via slow photoelectron velocity-map imaging spectroscopy of NdO. *The Journal of Chemical Physics* **2021**, *155* (11), 114305.
17. Carette, P.; Hocquet, A., Ligand field calculation of the lower electronic energy levels of the lanthanide monoxides. *Journal of Molecular Spectroscopy* **1988**, *131* (2), 301-324.
18. Kaledin, L. A., The electronic structure of neodymium monoxide: Ligand field assignment of states in the range 0–3 eV. *Journal of Molecular Spectroscopy* **2019**, *365*, 111207.

19. Allouche, A. R.; Aubert-Frécon, M.; Umanskiy, S. Y., Structure of low-lying electronic states of NdO: Quantum chemical calculations. *The Journal of Chemical Physics* **2006**, *124* (18), 184317.
20. Krauss, M.; Stevens, W. J., Comparative electronic structure of a lanthanide and actinide diatomic oxide: Nd versus U. *Molecular Physics* **2003**, *101* (1-2), 125-130.
21. Hannigan, M. C., A laser induced fluorescence study of SmO. *Journal of Molecular Spectroscopy* **1983**, *99* (1), 235-238.
22. Linton, C.; Bujin, G.; Rana, R. S.; Gray, J. A., Examination of the low-lying states of samarium monoxide. *Journal of Molecular Spectroscopy* **1987**, *126* (2), 370-392.
23. Bujin, G.; Linton, C., High resolution analysis of transitions to the five lowest electronic states of samarium monoxide. *Journal of Molecular Spectroscopy* **1989**, *137* (1), 114-126.
24. Bujin, G.; Linton, C., Examination of rotational structure, doubling, and perturbations in 12 low lying electronic states of samarium monoxide. *Journal of Molecular Spectroscopy* **1991**, *147* (1), 120-141.
25. Linton, C.; James, A. M.; Simard, B., Stark effect measurement in samarium monoxide: Dipole moments of the [16.6]1 and X0⁻ states. *The Journal of Chemical Physics* **1993**, *99* (12), 9420-9427.
26. Weichman, M. L.; Vlaisavljevich, B.; Devine, J. A.; Shuman, N. S.; Ard, S. G.; Shiozaki, T.; Neumark, D. M.; Viggiano, A. A., Electronic structure of SmO and SmO⁻ via slow photoelectron velocity-map imaging spectroscopy and spin-orbit CASPT2 calculations. *The Journal of Chemical Physics* **2017**, *147* (23), 234311.
27. Mulliken, R. S., The Interpretation of Band Spectra Part III. Electron Quantum Numbers and States of Molecules and Their Atoms. *Reviews of Modern Physics* **1932**, *4* (1), 1-86.

28. Field, R. W., Diatomic Molecule Electronic Structure beyond Simple Molecular Constants. *Ber. Bunsenges. Phys. Chem.* **1982**, *86*, 771-779.
29. Dulick, M.; Murad, E.; Barrow, R. F., Thermochemical properties of the rare earth monoxides. *The Journal of Chemical Physics* **1986**, *85* (1), 385-390.
30. Paulovič, J.; Gagliardi, L.; Dyke, J. M.; Hirao, K., The gas-phase chemiionization reaction between samarium and oxygen atoms: A theoretical study. *The Journal of Chemical Physics* **2004**, *120* (21), 9998-10001.
31. Schultz, R. H.; Armentrout, P. B., Reactions of N^{+4} with rare gases from thermal to 10eV center-of-mass energy: collision-induced dissociation, charge transfer and ligand exchange. *International Journal of Mass Spectrometry and Ion Processes* **1991**, *107* (1), 29-48.
32. Loh, S. K.; Hales, D. A.; Lian, L.; Armentrout, P. B., Collision-induced dissociation of $Fe+n$ ($n=2-10$) with Xe: Ionic and neutral iron binding energies. *The Journal of Chemical Physics* **1989**, *90* (10), 5466-5485.
33. Western, C. M., PGOPHER: A program for simulating rotational, vibrational and electronic spectra. *Journal of Quantitative Spectroscopy and Radiative Transfer* **2017**, *186*, 221-242.
34. Frosch, R. A.; Foley, H. M., Magnetic Hyperfine Structure in Diatomic Molecules. *Physical Review* **1952**, *88* (6), 1337-1349.
35. Lawler, J. E.; Den Hartog, E. A.; Sneden, C.; Cowan, J. J., Improved Laboratory Transition Probabilities for Sm and Application to the Samarium Abundances of the Sun and Three-Process-rich, Metal-poor Stars. *The Astrophysical Journal Supplement Series* **2006**, *162* (1), 227-260.